Alma Mater Studiorum · University of Bologna

School of Science
Department of Physics and Astronomy
Master Degree in Physics

Study of localized defect-bound excitonic transitions in TMD-WSe_2 monolayers and evanescent coupling to tapered optical nanofibers

Supervisor:
Prof. Gabriele Bolognini

Co-supervisor:
Prof. Valia Voliotis (Institut des Nanosciences de Paris)

Co-supervisor:
Prof. Richard Hostein (Institut des Nanosciences de Paris)

Co-supervisor:
Prof. François Dubin (Institut des Nanosciences de Paris)

Submitted by:
Enrico Tartari

Acknowledgments

The five-year physics course of study ends with the presentation of this project. Upon reaching this milestone, I can look over my shoulder for a moment and thank those who have allowed all this and who, most likely, will allow what I will achieve in the future.

First of all my great-grandmother Alba who, although not interested in this thesis even a bit, is certainly very interested in the fact that now I have finished studying and I can start working. Although it has been at least 10 years that she says that for her "it is time to go", her presence is surer than that of errors in this thesis. This has certainly helped me to keep going without ever stop as time is running out. Great-grandmother's next goal: getting married. I will see how to do it. Promised.

A huge thanks goes to my grandparents Mario and Franca who have always supported my choice of experience in France, asking me every day "When are you coming back?". Thank you for everything you did for me.

Obviously thanks also to my grandfather Giovanni, to whom I can assure that I have not only done physics in Paris but that I have even tasted many good cheeses and wines. Ok not very expensive ones.

Together with the grandparents, a thank you goes to my whole family who have always decided to be close to me, mainly at this time. In fact, a thank you goes to Sa 'e Papà that have been in the United States, one to my brother Giac who instead decided to go on Erasmus in Ljubljana and one to my "sister" Tata who is waiting for my return to Italy to go to study in Lisbon.

I cannot miss a thank you to you, Sofia, who despite having left me one hundred and fifty-three and a half times during this journey, you have been my safe place. I don't want you to change the number just reported.

And the friends? Certainly, thanks also to them with whom entertainment becomes a fixed appointment. Despite them, I managed to graduate anyway, as long as I do not fail during the presentation of the thesis. In particular, a recognition goes to Claudia, a certainty in my life, that if she is not watching Netflix and she happens to read this thesis, she will be happy for this sentence.

A very heartfelt thanks goes to my entire research group in Paris. A truly special group that from the very first moment gave me space and voice to express myself at all times, masking my naivety behind a smile. A truly cohesive group in which everyone brings something unique:

- Saavas: number one, hard worker and excellent researcher. From you I learned to save places on google maps and thus engrave unforgettable memories. Ah yes, also the passionate love for physics and coffee. Thank you.

- Richard: capable of anything, solves your problem in 5 minutes. True, but you have to wait for him at least 40. But, as soon as you hear the clink of keys approaching, you know your problems are about to recede. Thank you.
- Francois: the dreamer. Despite stealing his office job, he has always been kind to me. In the darkest moments his voice is the only one you wanted to hear. He can see excellent results even in non-functioning samples. Dreaming is free. But it works. Thank you.
- Valia: the boss. A continuous smile, she brought harmony to all the people who meet her. She left me the great advise of using a notebook as well as some extra pounds because of the honey candies. They are very good. Thank you.

A thanks certainly goes to my supervisor prof. Gabriele Bolognini who had to take the trouble to correct my work.

Finally, the last thanks goes to myself who, in the end, contributed to the achievement of this milestone.

Jokes aside, each of the people I mentioned has truly mapped out a safe path for me to achieve this goal, I have always felt protected. Thank you very much.

Enjoy the reading. If you want.

The experience of a master thesis abroad during a pandemic

The development of this master thesis was truly troubled. It all started in January 2019 with the first contacts with Valia, head of the Photons, Magnons et Technologies Quantiques (PMTeQ) research team of the Institut des NanoSciences de Paris (INSP). I can therefore say that I have been gravitating around this project for two years now. It officially began at the end of February 2020, coinciding exactly with the outbreak of the pandemic ... The work could be carried out in a normal way for two weeks. After that the laboratory was closed until mid-June. We never stopped work as we took advantage of these months by working on the simulations and having weekly discussions with the whole team on useful articles in the literature and discussing the simulations. After receiving the news of the reopening of the laboratory on June 16, I took the car and after 11 hours of travel I was in Paris to resume the measurements. The experimental work lasted until the end of July, interrupted in August (again 11 hours of driving) and resumed in September (again 11 hours of driving) until the end of October. Fortunately for me, the second lockdown in France deprived me of a single day of laboratory. Despite this, I admit that the pandemic played an important role in the forced reorganization of the project. But we never gave up.

Abstract

Transition Metal Dichalcogenides (TMDs), to which WSe_2 belongs, are a family of layered materials with potential applications in optics and electronics. Using the techniques developed for the graphene, TMDs were characterized and extraordinary physical properties were discovered: when thinned down to a monolayer, TMDs become direct band gap materials, therefore strongly facilitating light emission. The direct bandgap of these semiconductors is situated on the edge of the Brillouin zone, at the $K-$ point. This is different from standard semiconductors for optoelectronics like GaAs where the bandgap is in the centre of the Brillouin zone. The optical properties are dominated by excitons, Coulomb bound electron-hole pairs, and light-matter interaction is extremely strong. In particular, the demonstration of the existence of single photon emitter in WSe_2 monolayers motivated our project. Due to this, WSe_2 monolayers are among the most intriguing candidates for future optical quantum technologies attracting considerable attention in the field of two-dimensional materials. In this work we performed a detailed optical characterization of two samples of WSe_2 we produced in clean room (respectively sample 1 and sample 2). The monolayers were produced via exfoliation while we used an all dry deterministic transfer to encapsulate the samples in two layers of hexagonal boron nitride (hBN). We performed micro-photoluminescence ($\mu - PL$) and lifetime (T_1) measurements for both sample and degree of second-order temporal coherence ($g^{(2)}(\tau)$ measurements for sample 2. We focused our attention in localized defect-bound excitons due to the high intensity PL signal and sharp linewidth. Through a cleaner preparation for sample 2 with respect to sample 1, we were able to pass from an average signal intensity PL for the different emitters analyzed of 150 counts/s in sample 1 to an average intensity of 10000 counts/s in sample 2, increasing the signal by 100 times. We measured the T_1 for some emitter chosen in sample 1 and sample 2. In sample 1, we measured the T_1 of three emitters, respectively, $27.7 \pm 0.9ns$, $12.2 \pm 0.8ns$ and $12.1 \pm 0.3ns$. We measured the T_1 for an emitter in sample 2, finding $5.2 \pm 0.9ns$. The difference between the lifetimes of sample 1 and sample 2 is compatible with the presence of very different strains in the two samples. Finally, for the emitter with $T_1 = 5.2 \pm 0.9ns$ in sample 2 we performed $g^{(2)}(\tau)$ measurements, using both a mode-locked Ti-Sa laser (727.7 nm) in pulsed mode and in CW. Through the measurement of $g^{(2)}(\tau)$ in pulsed mode we could prove qualitatively the single photon source nature of the emitter by observing a drop in counts for a delay value of 0. From the measurement of $g^{(2)}(\tau)$ in CW mode, instead, we extract the exact value of the $g^{(2)}(0)$, i.e. $0.21 \pm 0.02ns$. Therefore we could successfully demonstrate that localized defect-bound excitons in WSe_2 monolayers are single photon sources. Moreover, in this work we have demonstrated the evanescent coupling of a single localized defect-bound exciton emitter with a tapered optical nano fiber we produced. For the fabrication of the nanofiber, through COMSOL and MATLAB simulations we found that a size of 0.6 um was right to have a sufficiently intense evanescent field to allow coupling to the emitter. We managed, through several repetitions, to produce autonomously the nanofiber of the desired size. Through the use of piezoelectric stages, we developed a setup that allowed us to have total and independent control of the positioning of the fiber on the sample and of the excitation laser, with a precision below the micrometer. Finally we were able to demonstrate the feasibility of the evanescent coupling of the emission to the fiber from a chosen localized defect-bound exciton. In terms of applications, for instance, the realization of integrated photonic circuits on a single chip requires controlled manipulation and integration of solid-state quantum emitters with nanophotonic components. The coupling to the tapered optical fiber we propose could fulfil this requirement. In fact, we were also able to demonstrate how the fiber collection setup can also be used for sample excitation in a fully fiber coupled way yielding a true integrated system. Thus, our results provide evidence of the possibility to integrate quantum emitters in 2D materials with photonic structures.

Contents

*Introduction

"[...] There is a device on the market, they tell me, by which you can write the Lord's Prayer on the head of a pin. [...] I now want to show that there is plenty of room at the bottom. [...] But I am not afraid to consider the final question as to whether, ultimately—in the great future—we can arrange the atoms the way we want; the very atoms, all the way down! What would happen if we could arrange the atoms one by one the way we want them?[...] What could we do with layered structures with just the right layers?[...] Atoms on a small scale behave like nothing on a large scale, for they satisfy the laws of quantum mechanics. [...] We can use, not just circuits, but some system involving the quantized energy levels, or the interactions of quantized spins, etc. [...] Now, you might say, "Who should do this and why should they do it?" Well, I pointed out a few of the economic applications, but I know that the reason that you would do it might be just for fun. But have some fun!"

This was the transcript of a talk presented by Richard P. Feynman to the American Physical Society in Pasadena on December 1959, which explores the immense possibilities afforded by miniaturization [17]. 60 years ago, incredible. My thesis explores the universe described by Feymann, in particular the planet described by the line "What could we do with layered structures with just the right layers?". And this is precisely what we have been asking ourselves in this project. I will therefore try, with the following thesis, to give a small contribution to the question. As it can be seen from the title, the thesis will focus on WSe_2, thus on layered transition metal dichalcogenides (TMDs) a class of materials belonging to the 2D materials family and the possibility to evanescent couple to a nanofiber the radiation emerging from the flakes after excitation. Before presenting the organization of the project, I would like to focus on why 2D materials and layered TMDs are now a hot topic in the scientific community.

The interest for TMDs

The advent of nanotechnology has made it possible to study materials in extreme dimensional limits: 2D (quantum wells), 1D (nanowires) and 0D (quantum dots). In this thesis we will focus on 2D materials in the atomic monolayer limit. Graphene, is not the only representative of the layered materials family. This family is vast, and many different types of materials exist: semiconductors, metals, insulators, superconductors... Like for the case of graphene, these materials present the advantage to be easily fabricated using exfoliation, a technique by far easier to develop and cheaper than growth methods such as molecular beam epitaxy (MBE). Moreover, using similar fabrication methods, it is possible to stack layers from different materials in order to obtain van der Waals heterostructures with new physical properties. The layers are simply deposited one on top of each other and the cohesion of the structure is ensured by van der Waals forces. In this case, another advantage compared to techniques like MBE is that lattice matching with the substrate material is not required [15]. Moreover the transition metal dichalcogenides (TMDs), going from bulk to monolayer samples, undergo a transition from an indirect to a direct bandgap between 1.0 and 2.0 eV for the main representatives of the family (MoS_2, WS_2, $MoSe_2$, WSe_2) which makes them promising materials for optoelectronics applications [68]. Moreover, two-dimensional transition metal dichalcogenides have drawn certain attentions in many other fields. The knowledge advances in atomically thin two-dimensional TMDs have led to a variety of promising technologies for nanoelectronics, photonics, sensing and energy storage[9] as well as the applications of in the field of biomedicine, including drug loading, photothermal therapy, biological imaging and biosensor [75].

Organization of the work

The project has two main objectives. First, the demonstration of the existence of single photon emitters in WSe_2 monolayers. We recognized localized defect-bound excitons as responsible for this. Second, the demonstration of the evanescent coupling of a localized defect-bound exciton emission to a tapered optical nano fiber. To achieve these goals, we produced a detailed study of WSe_2, starting from the fabrication process in the clean room, up to the characterization of the emission spectrum and the proof of the existence of single photon emitters. Then, before fabricating the nanofibers and demonstrating the coupling result, we tested the feasibility of the evanescent coupling with COMSOL and MATLAB simulations. Here we present in more detail what has been done during this work.

The monolayers were produced via exfoliation while we used an all dry deterministic transfer to encapsulate the samples in two layers of hexagonal boron nitride (hBN). We focused our attention in localized defect-bound excitons due to the high intensity PL signal and sharp linewidth. We performed on these emitters micro-photoluminescence ($\mu - PL$) and lifetime (T_1) measurements for both samples. For a chosen emitter in sample 2 we performed a photoluminescence excitation spectroscopy (PLE) measurement to highlight any resonances of the PL signal and increase the signal to noise ratio. Moreover, we performed a degree of second-order temporal coherence ($g^{(2)}(\tau)$ measurements for sample 2, to test the single photon source nature of these emitters. Then we moved to the second part of the work, so to the evanescent coupling of the localized defect-bound excitonic PL signal to a tapered optical nanofiber. For the fabrication of the nanofiber, we used COMSOL and MATLAB simulations to find the right size to have a sufficiently intense evanescent field to allow coupling to the emitter. Then, we managed, through several repetitions, to produce autonomously the nanofiber of the desired size. Through the use of piezoelectric stages, we developed a setup that allowed us to have total and independent control of the positioning of the fiber on the sample and of the excitation laser, with a precision below the micrometer. Finally, we tested the evanescent coupling of the emission from a chosen localized defect-bound exciton to the fiber.

Thus, the project is developed in three parts plus an appendix.

Part I deals with establishing the theoretical foundations necessary to understand the potential of TMDS as well as to provide the theoretical foundations for the experimental part. It will be divided into three chapters.

- **Introduction to TMDS**: We start with a general overview of the main properties of the family of materials to which WSe_2 belongs, that is, transition metal dichalcogenides. We will describe how their layered structure makes them particularly interesting in the field of optoelectronics, we will analyze their band structure and how it is modified when they are brought to the monolayer limit. The role of excitons and defects will be introduced. We will discuss, in particular, the localized intervalley defects bound excitons. The reasons for this interest come, not only from the high intensity of their photoluminescencence signal, but also from the intrinsic properties of their emission, i.e the property of being a source of single photons. To understand this last step, we need the theoretical foundations presented in the next chapter.

- **The concept of coherence in classical and quantum formulation**: In this chapter, the theoretical basis for the characterization of the signal emitted by the samples are presented. Characterizing, in this project, indicates, in addition to the spectral analysis of the micro-photoluminescence signal, the measurement of the radiative lifetime of the excited states and the degree of second-order temporal coherence $g^{(2)}(\tau)$. To develop the formalism, we will start from the concept of coherence and the description of the

Mach-Zehnder ($g^{(1)}(\tau)$) and Harbury-Brown Twiss ($g^{(2)}(\tau)$) interferometry experiments. We will see how the quantum treatment will allow us to introduce non-classical concepts such as "single photon sources" and "antibunching".

- **Fibers**: The third chapter, on the other hand, will be devoted to single mode nanofibers that we will use for the evanescent collection of the photoluminescence signal in the experimental part. We will briefly see the basic operating principle of optical fibers and some properties of nanofibers like their coupling with a point-like source. This chapter will conclude Part I.

Part II will be divided into two chapters: the first dedicated to the preparation of the materials in clean room, the description of the setups and the experimental techniques used. The second chapter will be dedicated to the detailed presentation of the main results obtained during the project. In detail, the two chapters are:

- **Sample Fabrication and experimental setups**: in this chapter we will describe the techniques of exfoliation and the all-dry deterministic transfer method we used to prepare WSe_2 monolayers and the encapsulation in hBN. Then, we will move to the description of the experimental techniques and setups, therefore optical spectroscopy, micro photoluminescence, the radiative lifetime (T1) setup and the $g^{(2)}(\tau)$ setup.

- **Experimental results**: The chapter is substantially divided into two parts. The first concerns the preparation in the clean room and the optical characterization of the WSe_2 flakes, while the second part will be dedicated to the evanescent coupling process of the radiation emitted in the tapered nanofiber. Starting from the COMSOL and MATLAB simulations, we will deal with the nanofiber fabrication process and finally the coupling results.

Part III: Conclusions In the last part of the project, the final conclusions of the project will be presented and some possible outlooks of the work presented will be discussed.

Part I

Theoretical Basis

Chapter 1

Introduction to TMDS

Monolayer transition metal dichalcogenides (TMDs) exhibit remarkable physical properties resulting from their reduced dimensionality and crystal symmetry. The family of semiconducting transition metal dichalcogenides is an especially promising platform for fundamental studies of two-dimensional (2D) systems, with several potential applications due to their direct band gap in the monolayer limit and highly efficient light-matter coupling. A crystal lattice with broken inversion symmetry combined with strong spin-orbit interactions leads to a unique combination of the spin and valley degrees of freedom. In addition, the 2D character of the monolayers yield a significant enhancement of the Coulomb interaction. The resulting formation of bound electron-hole pairs, or excitons, dominates the optical and spin properties of the material. In this chapter the main structural and optical properties of TMDs will be shown.

1.1 Transition Metal Dichalcogenide Monolayers

TMDS are a class of materials described by the chemical formula MX_2, where M is a transition metal element from group IV (Ti, Zr, Hf and so on), group V (for instance V, Nb or Ta) or group VI (Mo, W and so on), and X is a chalcogen (S, Se or Te). The layers, of thickness 6.5Å, have the form X-M-X with a transition metal plane between two chalcogen planes. All these planes form hexagonal lattices [70], as shown in Fig. 1.1.

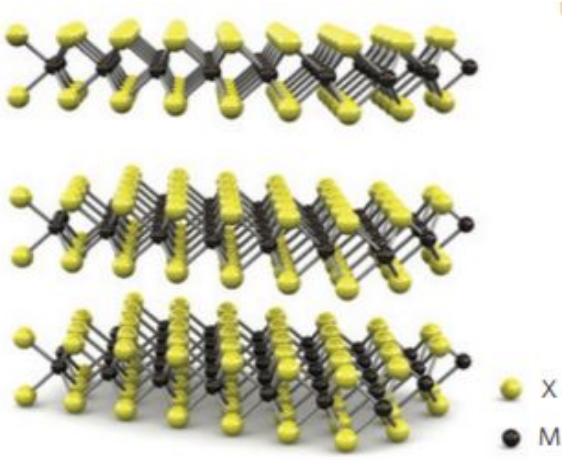

Figure 1.1: 3D representation of a transition metal dichalcogenides trilayer in the 2H phase with monolayers spaced by an interlayer spacing of 6.5 Å. [70]

They are layered materials, with strong covalent bonds in the layer plane and weak van der Waals forces between the layers [53]. They can form different phases which are illustrated

in Fig 1.2. The 2H phase with trigonal prismatic coordination is the phase the most likely to be found in nature and also in grown bulk material. For a long time these materials have been used as lubricants due to the weak van der Waals forces between the layers. Now, like for graphene, this property makes it possible to exfoliate TMD monolayers and to study their properties.

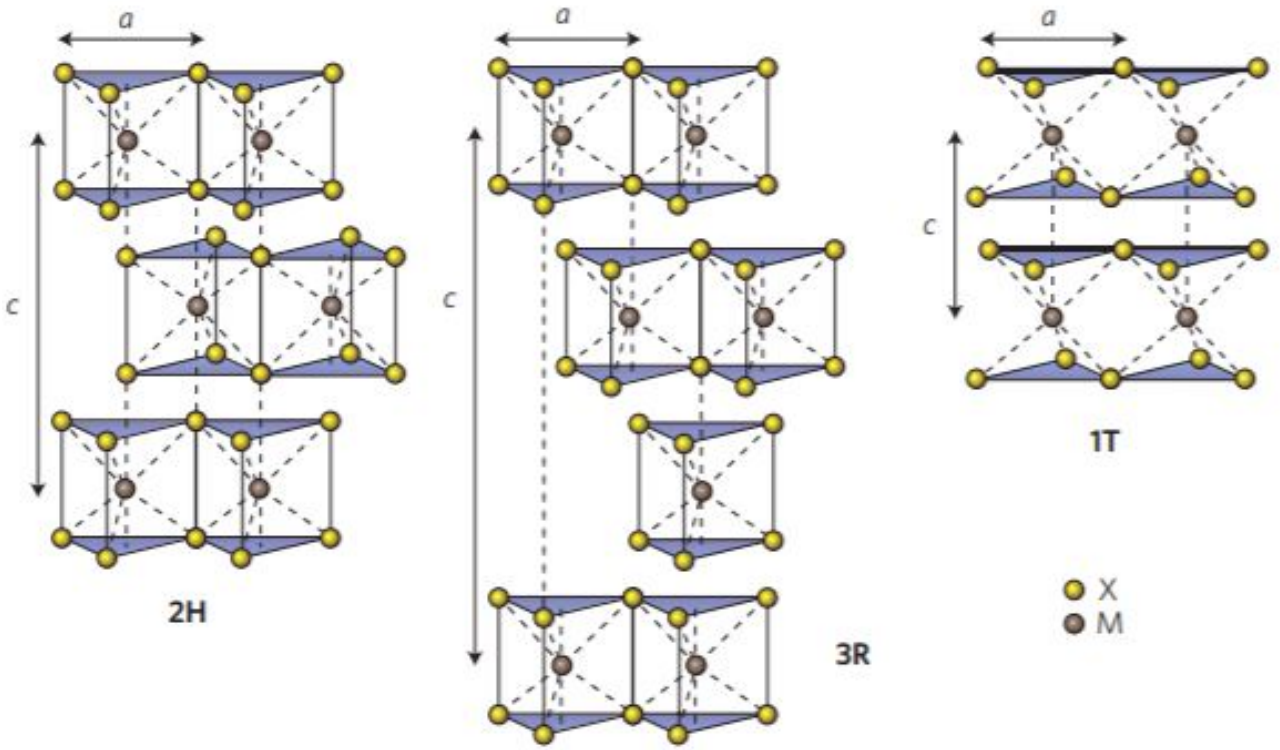

Figure 1.2: 3D representation of a transition metal dichalcogenides trilayer in the 2H phase with monolayers spaced by an interlayer spacing of 6.5 Å. [70]

1.2 Band Structure

The most important TMDs optical property we exploited during this project is the transition from indirect to direct band gap in the monolayer limit [68]. The band structure undergoes to a indirect to direct transition due to two main effects: quantum confinement and the change in orbitals hybridization. To calculate the TMDS band structure one can use density functional theory [30]. As an example, the calculation results for MoS_2 are displayed in Fig. 1.3. It is shown that the direct excitonic transition energy at the Brillouin zone K point barely changes with layer thickness, but the indirect bandgap increases as the number of layers decreases. Remarkably, the indirect transition energy becomes so high in monolayer MoS_2 that the material changes into a two-dimensional direct bandgap semiconductor.

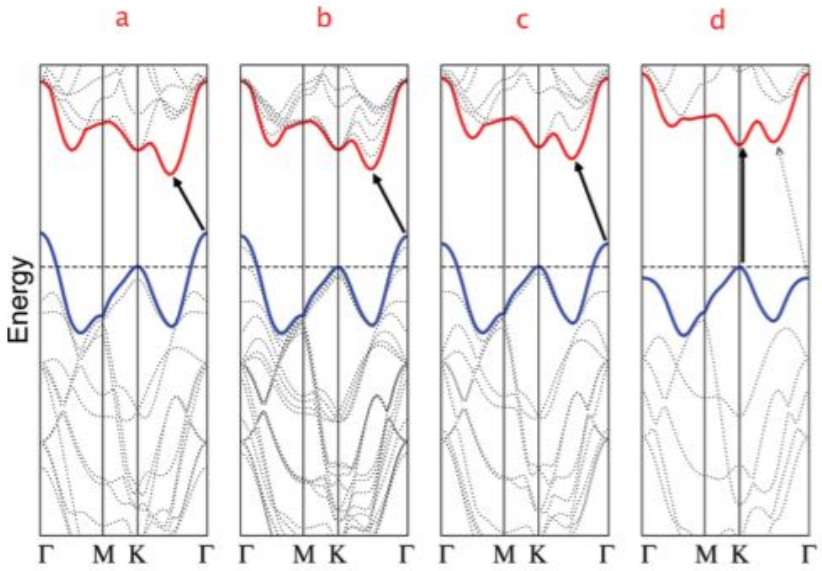

Figure 1.3: Calculated band structures of (a) bulk MoS_2, (b) quadrilayer MoS_2, (c) bilayer MoS_2, and (d) monolayer MoS_2. The solid arrows indicate the lowest energy transitions. Bulk MoS_2 is characterized by an indirect bandgap. The direct excitonic transitions occur at high energies at K point. With reduced layer thickness, the indirect bandgap becomes larger, while the direct excitonic transition barely changes. For monolayer MoS_2 in d, it becomes a direct bandgap semiconductor. This dramatic change of electronic structure in monolayer MoS_2 can explain the observed jump in monolayer photoluminescence efficiency. [64]

As shown in Fig. 1.4, the conduction band states at K-point are mainly due to d- orbitals from the transition metal atoms M which are sandwiched between the two layers of chalcogen atoms.

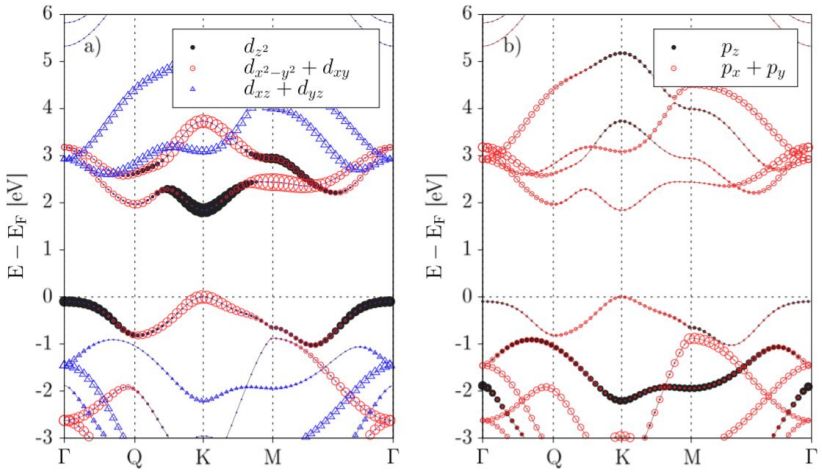

Figure 1.4: Atomic orbital weights in the energy bands of MX_2. (a) d-orbitals of the metal atom, and (b) p-orbitals of the chalcogen atoms. The size of each symbol is proportional to the weight of the atomic orbital. [32]

These orbitals are less influenced by the interlayer coupling, that is why the conduction band at K-point is not affected by the change in layer number, as illustrated in Fig 1.3. However, at local minima between K and Γ points, the conduction band moves with the layer number, increasing the value of the indirect bandgap until the material becomes direct in the monolayer limit. Again, this can be related to the conduction band states at this point which are due to a

combination of p-orbitals from the chalcogen atoms and d-orbitals of the metal atoms. In this case, the p-orbitals from the chalcogen atoms are strongly influenced by the interlayer coupling effect, explaining why the conduction band energy at this point changes with layer number. For a more realistic analysis of TMD band structure, spin orbit effects have to be taken into account. A typical DFT-calculated band structures of a MX_2 TMD monolayer with spin-orbit effect is presented in Fig. 1.5.

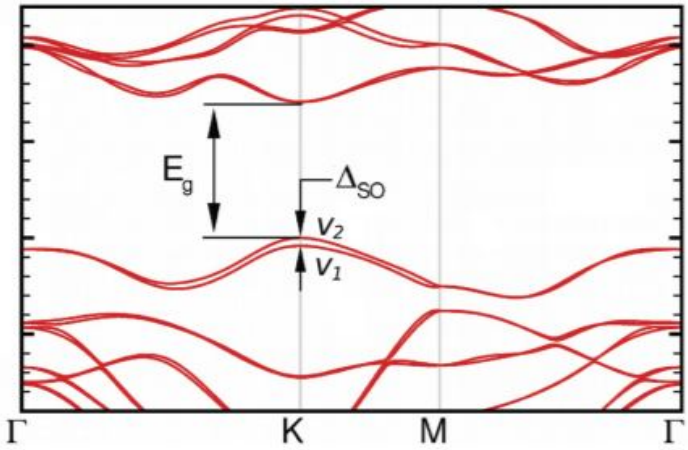

Figure 1.5: Typical band structure for an MX_2 monolayer. The valence-band maximum is split due to spin-orbit coupling. Transitions between ν_2 and the conduction-band minimum at K lead to A-type excitons in the absorption spectrum, while transitions between ν_1 and the conduction-band minimum at K lead to B-type excitons. [55]

The values of the splitting in the valence and in the conduction band are shown in Tab. 1.1. This effect is particularly important in TMDS and gives rise to large splittings. Spin-orbit splitting for the valence band is larger for W-compounds than for Mo-compounds and that is because W atoms are heavier. In the conduction band the spin-orbit splitting is smaller than in valence band, and it is due to the partial compensation of the p- and the d-states contribution. The SO splitting gives rise to the two valence subbands and, accordingly, to two types of excitons, A and B, which involve holes from the upper and lower energy spin states respectively [68].

	MoS_2	$MoSe_2$	WS_2	WSe_2	$MoTe_2$	WTe_2
Δ_{SO}^{VB} in meV	148	186	429	466	219	484
Δ_{SO}^{CB} in meV	3	22	-32	-37	32	-54

Table 1.1: Spin-orbit splitting values for valence and conduction bands for some TMDs. [32]

Is important to notice that, as we can see from Tab.1, depending on the metal atom, Mo or W, the conduction band splitting has different sign, as indicated in Fig. 1.6. Thus, thanks to the SO splitting, at the K-point, the spin degeneracy of both the conduction and valence bands is fully lifted. This stands in marked contrast to typical GaAs or CdTe quantum-well structures where the CB minimum and VB maximum occur at the F-point and both the conduction and valence band states remain spin degenerate [68]. The CB spin splitting results in an energy separation between the spin-allowed and optically active (bright) transitions and the spin-forbidden and optically inactive transitions (dark). This topic will be developed in the following sections.

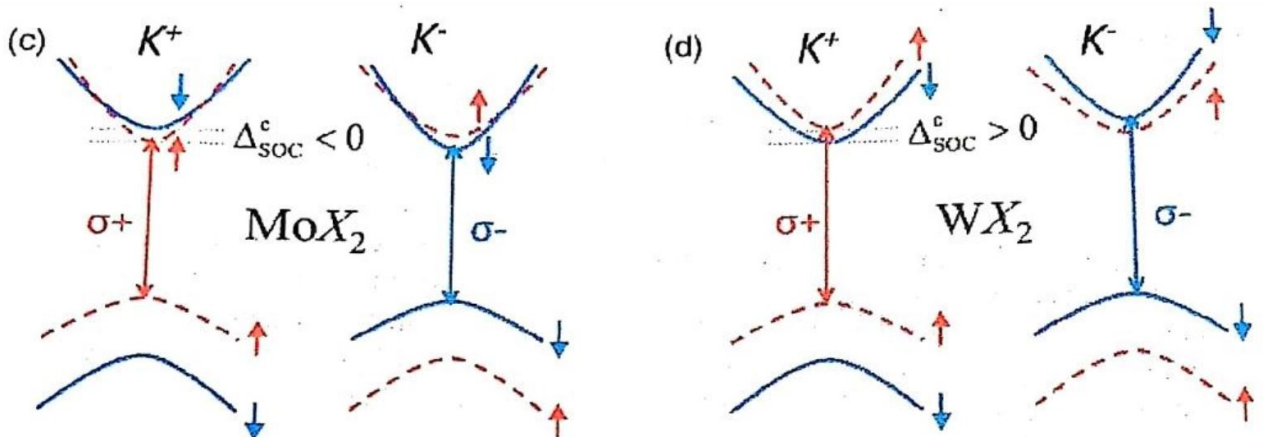

Figure 1.6: Schematic illustrations in a single-particle picture show that the order of the conduction bands is opposite in MoX_2 (c) and WX_2 (d) monolayers. [68]

Monolayers can be identified using atomic force microscopy (AFM), Raman, and Photoluminescence (PL) measurements, as shown in Fig. 1.7 (a) and (b) [66]. As previously said, the PL signal is enhanced by orders of magnitude from the bulk to monolayer due to the indirect to direct bandgap transition. Even at room temperature, monolayer MoS_2, $MoSe_2$, and WSe_2 show a strong PL peak at 1.84 eV, 1.56 eV and 1.65 eV, respectively in Fig. 1.7 (c).

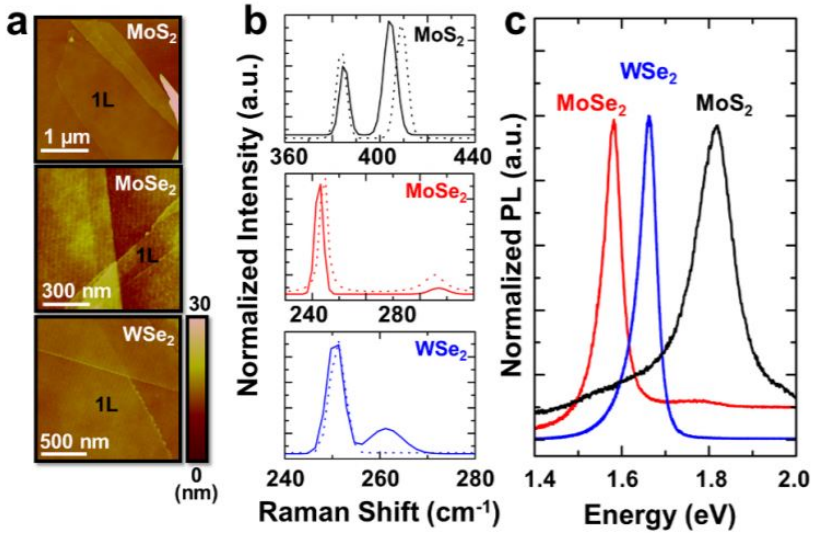

Figure 1.7: (a). AFM images taken on monolayer MoS_2, $MoSe_2$, and WSe_2. (b). Raman spectrum measured on monolayer MoS_2, $MoSe_2$, and WSe_2, where the solid and dashed curves correspond to monolayers and few-layers, respectively. (c). Room-temperature normalized PL for monolayer MoS_2, $MoSe_2$, and WSe_2. Figure extracted from [66].

To conclude this section, the observation of PL signal is consistent with the theoretical prediction of indirect to direct bandgap transition when going from multilayer to monolayer thickness. This points out a new direction for controlling electronic structure in nanoscale materials by exploiting rich d-electron physics. Such capability can lead to engineering novel optical behaviors not found in sp-bonded materials and holds promise for new nanophotonic applications [68].

1.3 Excitons in TMD monolayers

The optical properties of TMDS are dominated by Coulomb bound electron-hole pairs called excitons. This follow from the optical excitation of a semiconductor that can promote the transition of an electron frome the valence band to the conduction one, leaving behind an empty state in the valence band termed hole, Fig. 1.8. For example a photon with momentum $\vec{q}$ can generate an exciton. In general, the photon wavevector can be neglected compared to crystal momentum [68] and due to momentum conservation, the following relation holds for the exciton momentum: $\vec{K}_{exc} = \vec{k_e} + \vec{k_h}$ with $\vec{k_e}$ the momentum of the electron and $\vec{k_h}$ the momentum of the hole forming the exciton. It is possible to distinguish two main types of excitons: Frenkel and Wannier-Mott excitons. Frenkel excitons are also called tightly-bound excitons because their radius is of the order of the crystal lattice parameter. They are mainly present in insulators and molecular crystals. By contrast, Wannier-Mott excitons are also named free excitons due to their delocalized character and have a radius which extends over many atoms.

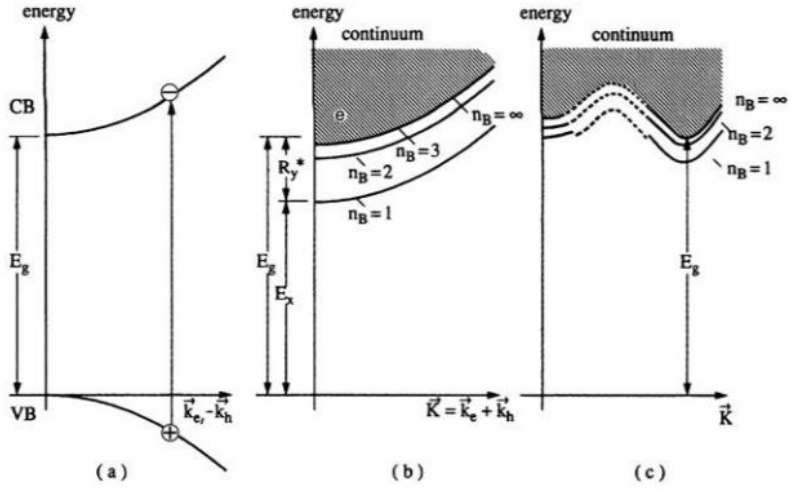

Figure 1.8: An exciton in the scheme of valence and conduction band (a) in the exciton picture for a direct (b) and for an indirect gap semiconductor (c). [30]

They are mainly present in inorganic crystals such as semiconductor. The electron and the hole have relative motions which are strongly correlated as illustrated in Fig. 1.9 (a) ,(b), for an exciton in a 2D TMD crystal. The position of the electron is clearly linked to the position of the hole. Then it is important to distinguish these relative positions and the motion of whole pair-state exciton which corresponds to the motion of the exciton center of mass having a wavevector $\vec{K}_{exc}$.

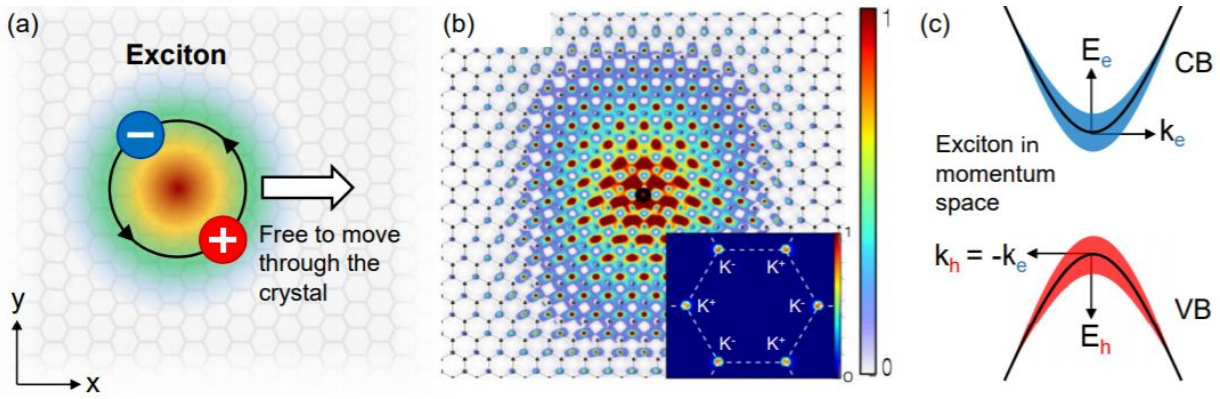

Figure 1.9: (a) Real-space representation of the electron-hole pair bound in a Wannier-Mott exciton, showing the strong spatial correlation of the two constituents. The arrow indicates the center of mass wavevector responsible for the motion of the exciton as a whole. (b) Ttypical exciton wavefunction calculated for monolayer MoS2. The modulus squared of the electron wavefunction is plotted in color scale (gray scale) for the hole position fixed at the origin. The inset shows the corresponding wavefunction in momentum space across the Brillouin zone, including both K^+ and K exciton states. (c) Representation of the exciton in reciprocal space, with the contributions of the electron and hole quasiparticles in the CB and VB, respectively, shown schematically by the width of the shaded area. [68]

Here it will be quickly shown how to estimate the exciton binding energies and excited exciton states, the 3D case calculations within effective mass approximation will be developed and then transposed to the 2D case. It is possible to consider the exciton as an hydrogen-like system with a Coulomb interaction given by:

$$V(|\vec{r_e} - \vec{r_h}|) = \frac{-e^2}{4\pi\epsilon_0\epsilon_r\,|\vec{r_e} - \vec{r_h}|} \tag{1.1}$$

with e the charge of the electron, ϵ_0 the vacuum permittivity, ϵ_r, the relative permittivity of the medium, $\vec{r_e}$ the electron position and $\vec{r_h}$, the hole position. Like for an hydrogen atom, the exciton has different hydrogenoid excited states which are represented in Fig 1.8 (b) with different principal quantum numbers n_B. This is the exciton Rydberg series. The wavefunction of an exciton can be written as [30]:

$$\Psi_{\vec{K}_{exc},n_B,l,m} = \Omega^{-\frac{1}{2}} e^{i\vec{K}_{exc}\vec{R}} \Phi_e(\vec{r_e})\Phi_h(\vec{r_h})\Phi^{env}_{n_B,l,m}(\vec{r_e} - \vec{r_h}) \tag{1.2}$$

where $\Omega^{-\frac{1}{2}}$ is the normalization factor, $\Phi_e(\vec{r_{e,h}})$ are the wave packets for electrons and holes, $\Phi^{env}_{n_B,l,m}(\vec{r_e} - \vec{r_h})$ is the envelope function of the relative electron-hole motion and $\vec{R}$ is the position of the centre of mass, given by:

$$\vec{R} = \frac{m_e\vec{r_e} + m_h\vec{r_h}}{m_e + m_h} \tag{1.3}$$

We note that the relative electron-hole motion and the centre of mass motion are separated and so the exciton wavefunction can be simply noted $V(\vec{R}, \vec{r_e} - \vec{r_h})) = G(\vec{R})F(\vec{r_e} - \vec{r_h}))$. In order to determine the total energy of exciton states, the Schrödinger equation must be solved for these two components of the exciton wavefunction. Solving the Schrödinger equation for the envelope function of the relative electron-hole motion and for simple spherical bands, enables determining bound states energies of the exciton (1s, 2s, 3s...), where 1, 2, 3 are the principal quantum numbers n_B. Developing the calculations, it is possible to find [30]:

$$E_{exc}(n_B, \vec{K}_{exc}) = E_g - R^*_y \frac{1}{n_B^2} + \frac{\hbar^2 \left|\vec{K}_{exc}\right|^2}{2M_{exc}} \tag{1.4}$$

where $E_{exc}(n_B, \vec{K}_{exc})$ is the total energy of the exciton states, E_g is the free carrier band gap, R_y^* is the exciton Rydberg energy (contains the effective mass term). The exciton binding energy is just defined as $E_B = E_g - E_{exc}$ and decreases as n_B increases. Now we just need to move from the 3D to the 2D case for the TMDs monolayers. In 2D the motion of the electron and the hole is restricted to a 2D plane and so $\vec{K}_{exc} = \vec{K}_x + \vec{K}_y$. It is possible to show that in this case [30]:

$$E_{exc}^{2D}(n_B, \vec{K}_{exc}) = E_g + E_Q - R_y^* \frac{1}{(n_B - \frac{1}{2})^2} + \frac{\hbar^2 \left|\vec{K}_{exc}\right|^2}{2M_{exc}} \tag{1.5}$$

Quantitatively, when going from 3D to 2D, n_B has to be replaced by $(n_B - \frac{1}{2})$. This considerably changes the binding energies. If we take for instance $n_B = 1$, in 3D we obtain a binding energy proportional to R_y^* whereas in 2D it is proportional to $4R_y^*$. So the binding energies are larger in 2D compared to 3D. So, taking into account the excitonic effects, we expect excitonic transitions to appear below the free particle bandgap as in Fig. 1.10. Indeed most emission and absorption spectra for high quality samples are dominated by $n = 1$ excitonic transitions.

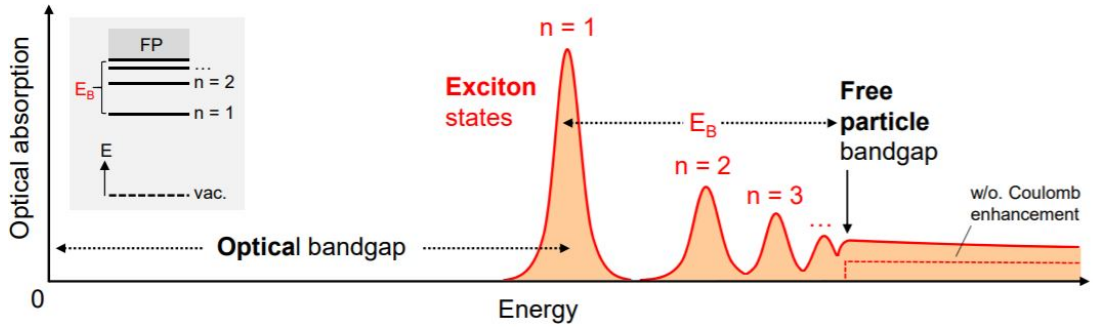

Figure 1.10: Illustration of the optical absorption of an ideal 2D semiconductor including the series of bright exciton transitions below the renormalized quasiparticle band gap. In addition, the Coulomb interaction leads to the enhancement of the continuum absorption in the energy range exceeding the exciton binding energy (E_B). The inset shows the atom-like energy level scheme of the exciton states, designated by their principal quantum number n, with the binding energy of the exciton ground state ($n = 1$) denoted by E_B below the free particle bandgap (FP). [68]

1.4 Light-matter coupling via excitons

When thinned down to the limit of a single monolayer, the band gap becomes direct and the corresponding band extrema are located at the finite momentum K^+ and K^- points of the hexagonal Brillouin zone, Fig. 1.12, and give rise to interband transitions in the visible to near-infrared spectral range. In the literature, the energy states close to the K^+/K^- points located at the edges of the first Brillouin zone are typically referred to as K^+ and K^- valleys, whereas the term valley is generally used to designate band extrema in momentum space. The presence of a direct gap is particularly interesting for potential device applications because of the associated possibility for efficient light emission. In addition to being direct, the optical transitions at the gap are also valley selective, as σ^+ and σ^- circularly polarized light can induce optical transitions only at the K^+ and K^- valleys, respectively [11]. This is in strong contrast to systems such as GaAs and many other III-V and II-VI semiconductors, where the bandgap is located at the center of the Brillouin zone (Γ-point). As shown in the previous sections, an additional interesting feature of TMDs materials is the presence of strong spin-orbit interactions,

which introduce spin splitting of several hundred meV in the valence band and of a few to tens of meV in the conduction bands, where the spin states in the inequivalent valleys K^+ and K^- are linked by time reversal symmetry. In a semiconductor, following absorption of a photon with suitable energy, an electron is promoted to the conduction band, leaving behind a hole in the valence band. In TMD MLs the electrons and holes are tightly bound together as excitons by the attractive Coulomb interaction, with typical binding energies on the order of $0.5eV$. As a result, the fundamental optical properties at both cryogenic and room temperatures are determined by strong exciton resonances. At the corresponding transition energies, the light-matter interaction is strongly enhanced in comparison to the transitions in the continuum of unbound electrons and holes. For these materials with almost ideal 2D confinement and reduced dielectric screening from the environment, the Coulomb attraction between the hole and the electrons is one to two orders of magnitude stronger than in more traditional quasi-2D systems such as GaAs or GaN quantum wells used in today's optoelectronic devices. Moreover, the Coulomb interaction in TMD MLs also determines the valley polarization dynamics of excitons and contributes to the splitting between optically bright and dark exciton states, in addition to spin-orbit coupling, see Fig. 1.11.

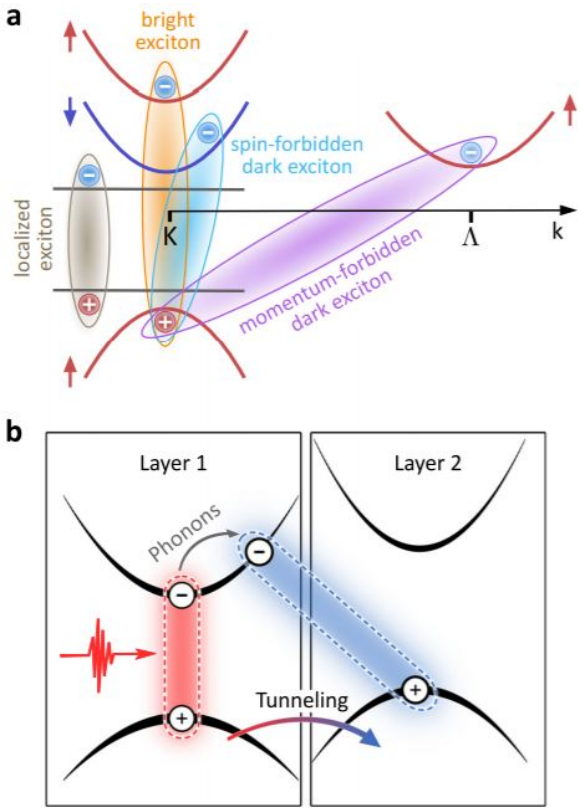

Figure 1.11: Different exciton types in atomically thin nanomaterials and related heterostructures. (a) Excitons are Coulomb-bound electronhole pairs (ovals in the picture). Momentum-forbidden dark excitons consist of electrons and holes located at different valleys in the momentum space. Spin-forbidden dark excitons consist of electrons and holes with opposite spin. These states cannot be accessed by light due to the lack of required momentum transfer and spin-flip, respectively. Electrons and holes in localized excitons are trapped into an impurity-induced potential. (b) Interlayer excitons appear, where electrons and holes are located in different layers. [49]

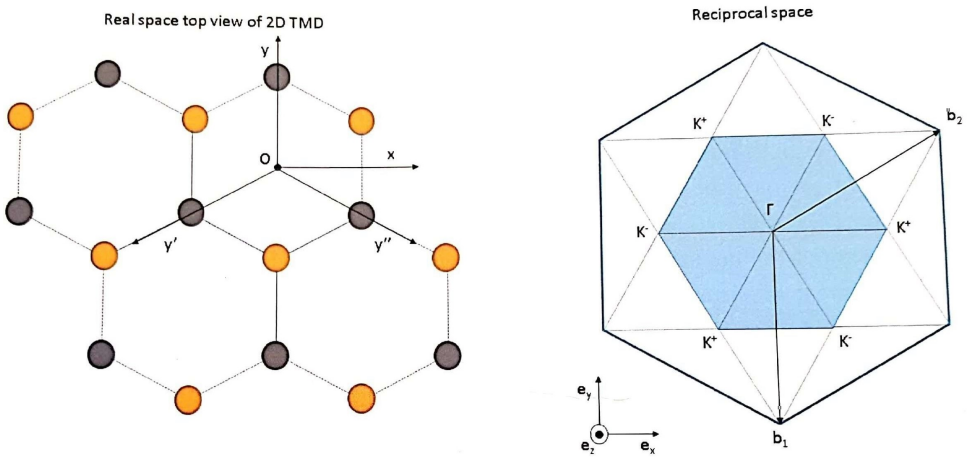

Figure 1.12: Real and reciprocal space of a 2D TMD. The shaded area corresponds to the first Brilluoin zone. In real space the point group of the crystal is D_{3h} with a rotation axis of order 3 (Oz), 3 axis of order 2 ($Oy, Oy^{'}, Oy^{"}$), one mirror operation σ_h defined from (xOy) and 3 mirror operations $\sigma_v, \sigma_v^{'}, \sigma - v^{"}$ defined from the planes (yOz), (y'Oz), (y"Oz). In reciprocal space, at the corners of the Brilluoin zone (K^+ and K^-), the point group is C_{3h}; due to inequivalent K valleys the symmetry is lowered (order 2 axis and the corresponding mirror symmetries $\sigma_v, \sigma_v^{'}$ and $\sigma_v^{"}$ are suppressed).[52]

It has been shown that, depending on the metal atom (Mo or W), the conduction band spin splitting has a different sign, as indicated in Fig. 1.6. Hence, at the K-point, the spin degeneracy of both the conduction and valence bands is fully lifted. As already mentioned, this stands in marked contrast to typical GaAs quantum well structures where the CB minimum and VB maximum occur at the Γ-point and both the conduction and valence band states remain spin degenerate. The CB spin splitting results in an energy separation between the spin-allowed and optically active (bright) transitions and the spin-forbidden and optically inactive transitions (dark), Fig 1.11 (a). For these reasons, The lowest energy transition in MoX_2 is expected to be the bright exciton. In contrast for the WX_2 materials, dark excitons are predicted to be lower energies, Fig. 1.6. The chiral optical selection rules for interband transitions in the $K^{\pm}$ valleys can be deduced from symmetry arguments [68]. It can be shown that, the optical selection rules for the interband transitions at $K^{\pm}$ valleys are chiral: the σ^+ (σ^-) circularly polarized light can only couple to the transition at K^+ (K^-). Thus, selective optical excitation of valleys in momentum space is possible. This selective excitation of valley circularly polarized has been proved [73], especially through photoluminescence (PL) experiments which revealed a conservation of the polarization. For instance, if K^+ valleys are excited with a σ^+ polarized laser, a σ^+-polarized PL is measured. In conclusion, the optical generation and detection of the spinvalley polarization are possible, rendering the TMD monolayers an ideal platform to study the electron valley degree of freedom in the context of valleytronics.

It is also important to emphasize that for an electron to change valley, it has either to flip its spin (see Fig. 1.6) or undergo an energetically unfavorable transition, especially for the valence states. As a result, optically generated electrons and holes are both valley and spin polarized, which is termed spin-valley locking. Therefore, following the σ^+ excitation, the exciton emission in TMD MLs can be co-polarized with the laser if the valley polarization lifetime is longer or of the order of the recombination time. This behavior stands in contrast to that of III-V or II-VI quantum wells where excitation with the circularly polarized light usually results only in spin-polarization of the charge carriers [68].

1.5 Defect-bound excitons

Defects in semiconductors can trap free charge carriers and localize excitons. The interaction between these defects and charge carriers becomes stronger at reduced dimensionalities, and is expected to greatly influence physical properties of the hosting material. Indeed, a sub-bandgap emission peak as well as increase in overall photoluminescence intensity can be measured through PL experiments [66]. These effects offer a possible route toward tailoring optical properties of 2D semiconductors by defect engineering. Due to the intense optical signal and their non-classical single-photon emission character, the excitons bound to the defects will be the emitters on which this project will be focused. In semiconductors, lattice point defects such as vacancies and interstitials can act as very efficient traps for electrons, holes and excitons, and strongly influence transport and optical properties of the host material. Excitons bound to defects, if recombine radiatively, lead to light emission at energies lower than free excition transition energy. Such interactions become stronger in reduced dimensionalities due to tighter localization of the electron wavefunction. Although the understanding of point defects in conventional 3D semiconductors is well established and the defects database is relatively complete, physics and behaviour of point defects in 2D semiconductors, such as the newly emerging monolayer semiconducting transition metal dichalcogenides (TMDs), have remained an unexplored field. As well as 3D crystals, layered TMDs possess defects which can play an important role in changing the opto-electronic properties of the material. Due to the 2D nature of TMDs monolayers, defects can be categorized similarly as in graphene [42]: vacancies, topological defects (grain boundaries and extended line of defects) and defects that change the curvature of the structure.

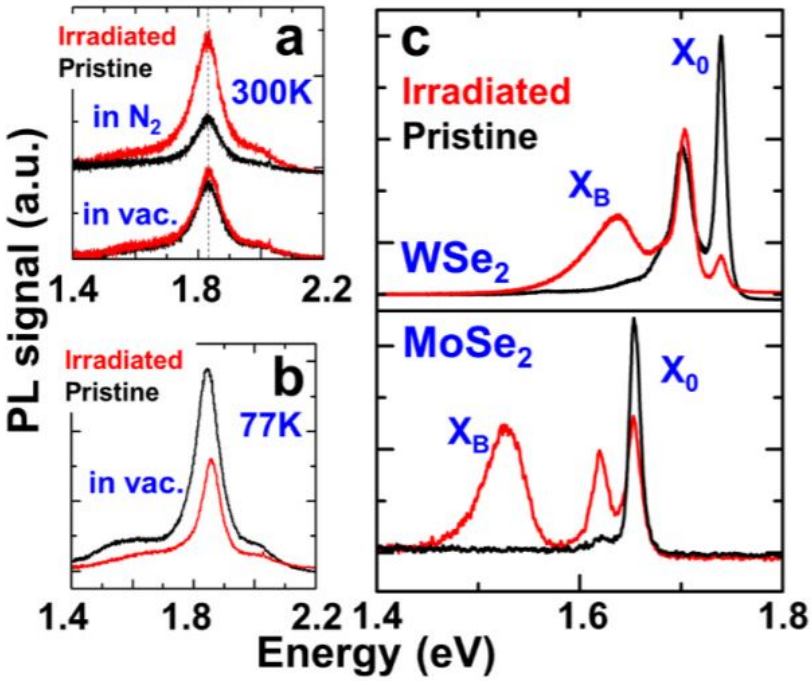

Figure 1.13: (a) PL spectrum of a monolayer MoS_2 at 300 K in the presence of N_2 or in vacuum before and after irradiation. (b) The same taken at 77 K in vacuum. (c) PL spectrum taken at 77 K in N_2 on WSe_2 and $MoSe_2$ monolayers before and after the irradiation. Figure extracted from [66].

In addition, doping or alloying and different stackings can add defects in TMDs. For instance, in the work presented in [66] they show that the irradiation with MeV α particles or thermal annealing at sub-decomposition temperatures introduce anion vacancies in monolayer

MoS_2, $MoSe_2$, and WSe_2, where the vacancy density can be controlled by the irradiation dose or annealing time. These defects introduce a new emission peak below the free-exciton PL peak, and its intensity is enhanced as the defect density is increased. Moreover, the overall PL intensity also increases at higher defect densities, and as such, the defective material becomes more luminescent compared to pristine monolayers. Their results are summarised in Fig. 1.13. The full treatment of the defects in crystal is not in our aim since we just need the experimental proven phenomenon of the appearance of transitions lines within the band gap energies despite the pure nature of the defect that create the state. However the most probable cause of the presence of the bright and narrow peaks in our samples is the presence of localized inter-valley defect excitons that, indeed, behave as single-photon sources. Thus, in the next paragraph, we will retrace the work of Linhart et al. [39] to provide a very brief presentation of this kind of excitonic transition lines. To see a detailed explanation please see [39].

1.5.1 Localized inter-valley defect excitons as single-photon emitters in WSe_2

The research group of Linhart et al. claimed to have identified inter-valley defect excitonic states as the likely candidate for antibunched single-photon emission (SPE) [39]. This model is shown to account for a large variety of experimental observations including brightness, radiative transition rates, the variation of the excitonic energy with applied magnetic and electric fields. They proposed a multi-scale simulation for WSe_2 with locally varying strain and in the presence of point defects.

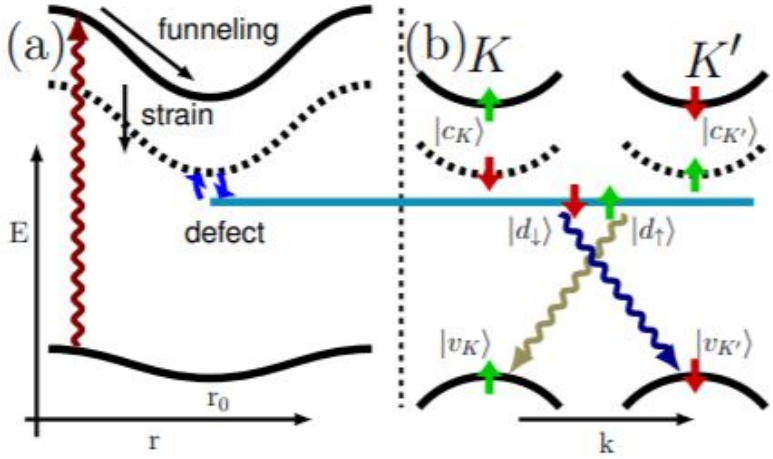

Figure 1.14: Single photon emitter in WSe2, schematically (a) Real space representation: a free exciton is created (dark red arrow), strain efficiently funnels excitons with the electron in the bright (solid black line) and dark (dashed line) conduction band state down in energy towards the strain maximum near r_0 due to the strain-dependent bandgap: mixing of the strain-localized dark exciton with a defect state leads to the formation of a strongly localized defect exciton. (b) Reciprocal space: while strain-localized exciton states (dashed) remain dark, a point defect (horizontal cyan line) breaks the valley selectivity and leads to efficient photoemission (dark blue/yellow arrows). Figure extracted from [39].

From the simulation the autors envisioned the following scenario for the origin of SPEs: the strongly non-uniform strain variations result in the lowering of excitonic energies in the strained region forming a weakly localized exciton, see Fig. 1.14 (a). Moreover, in the presence of a point defect in this region, hybridization with a strongly localized defect level in the band

gap leads to the formation of a novel electron-hole pair configuration termed inter-valley defect exciton for which the broken valley symmetry allows efficient radiative decay, see 1.14 (b), the key prerequisite for a SPE. In summary, Linhart et al., in [39], have developed a microscopic model for bright single photon emitters in WSe_2 and have identified inter-valley defect excitons as likely candidates for strong photoemission at energies lower than the band gap. As proof of what has just been said, from the experimental point of view, we can affirm with high confidence that the brightest photoluminescence peaks are always found in the vicinity of cracks or in any case inhomogeneity of the sample, therefore areas in which the strain is certainly present.

1.6 TMDs heterostructures

To conclude the chapter we will present briefly the possibility to produce sophisticated heterostructures through TMDs. It has already been mentioned that at the monolayer limit the TMDs become a direct band gap semiconductor. This direct band gap behavior opens fascinating possibilities when studying few-layered systems since they possess different electronic properties from the bulk and from the monolayer form [42]. Recently, it has been found in bilayers of WS_2, WSe_2, MoS_2 and $MoSe_2$, the indirect and direct band gaps can become very close to one another with differences of around $0.14eV$, anyway, the indirect band gap always dominates. However, if different semiconducting TMDs are used to form van der Waals heterostructures such as heterobilayers, band gap tuning and direct band gaps might be possible.

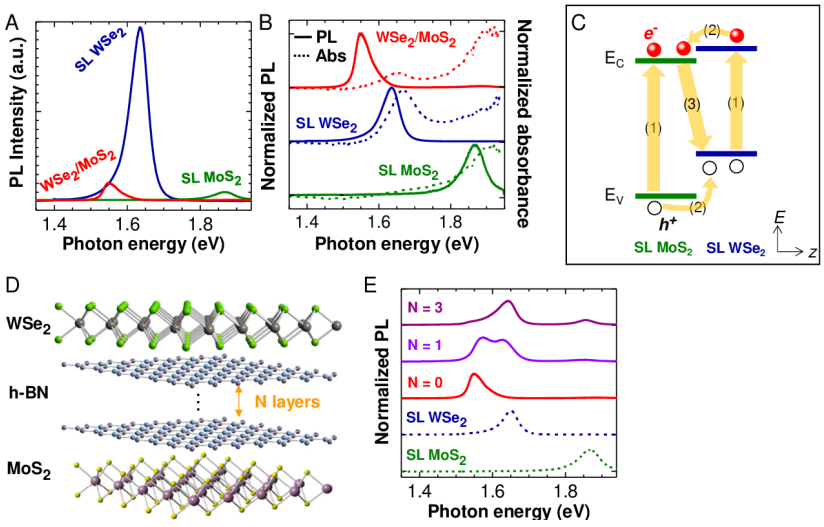

Figure 1.15: Photoluminescence and absorption from WSe_2/MoS_2 hetero-bilayers. (A) PL spectra of single-layer WSe_2, MoS_2, and the corresponding hetero-bilayer. (B) Normalized PL (solid lines) and absorbance (dashed lines) spectra of single-layer WSe_2, MoS_2, and the corresponding hetero-bilayer, where the spectra are normalized to the height of the strongest PL/absorbance peak. (C) Band diagram of WSe_2/MoS_2 hetero-bilayer under photo excitation, depicting (1) absorption and exciton generation in WSe_2 and MoS_2 single layers, (2) relaxation of excitons at the WSe_2/MoS_2 interface driven by the band offset, and (3) radiative recombination of spatially indirect excitons. (D) An atomistic illustration of the heterostructure of single-layer WSe_2/single-layer MoS_2 with few-layer h-BN spacer in the vdW gap. (E) Normalized PL spectra from single-layer WSe_2/single-layer MoS_2 heterostructure with n layers of h-BN (n = 0, 1, and 3) Figure extracted from [15].

Semiconductor heterostructures are the fundamental platform for many important device applications such as lasers, light-emitting diodes, solar cells, and high-electron-mobility transistors. Indeed, analogous to traditional heterostructures, layered transition metal dichalcogenide

heterostructures can be designed and built by assembling individual single layers into functional multilayer structures, but in principle with atomically sharp interfaces, no interdiffusion of atoms, digitally controlled layered components, and no lattice parameter constraints [15]. The main optical properties of a WSe_2/MoS_2 heterostructure, chosen as an example, is presented in Fig. 1.15 [15].

Chapter 2

The concept of coherence in classical and quantum formulation

Coherence is a crucial property for a light source. In the framework of my thesis, we stressed out the concept of coherence, in particular the second-degree of temporal coherence since its value describe the quantum or classical nature of the source and, for instance, whether it is possible or not to use the light source in the applications which require a single photon source. Thus, before introducing the experimental part of the project where we measured the second order coherence it is useful to understand what coherence really is and why it is important. Coherence is defined as the ability of waves to interfere. Intuitively, coherent waves have a well-defined constant phase relationship. However, a detailed mathematical analysis need to be stressed out for a deep understanding of the concept of coherence. Mathematically, correlation functions have been introduced to measure the coherence between the electric field components. These correlations can be measured to arbitrary orders, hence leading to the concept of different orders of coherence. The first order of coherence can be measured by a Micheloson or a Mach-Zender interferometer, while the second order of coherence with an Hanbury Brown-Twiss interferometer. The formers tell us how the electric field measured at two points in time is correlated, and the latter quantifies the correlation of the electric field intensity. The goal of the chapter is to point out a physical and mathematical description of coherence and of the two correlation functions known as the degree of first-order temporal coherence and the degree of second-order temporal coherence. After the description of the basic definition of spatial and temporal coherence, we will introduce the different types of light sources. Then, starting from the classical description of coherence we will slowly move to a brief quantum description. The Mach-Zender and the Hanbury Brown-Twiss interferometer will be presented as well. The last part of the chapter will be occupied by the quantum formulation and the value it predicts for the second-degree of coherence for a single photon source. Even though the measurement of the first-degree of coherence for our defects-bound excitons will not be carried out in this project, I thought it was necessary to describe it since its description provide us the mathematical tools to develop the description of the second-degree of coherence which we had measured.

2.1 Coherence

In general there are two types of coherence for waves: spatial coherence and temporal coherence. Both are represented in Fig. 2.1. The temporal coherence is a measure of the phases correlation of a light wave at different points along the direction of propagation. In that sense one can refer to the temporal coherence as the longitudinal coherence. Temporal coherence, thus, give us an idea about the confidence with which we can predict the amplitude and the phase of the wave at the time τ knowing their values at a time $t < \tau$. Of course we need to take into account

the coherence time τ_c of the light beam since making prediction for a $\tau > \tau_c$ makes no sense [45]. For the case of an ideal plane wave, as in Fig. 2.1 (a), the temporal coherence is infinite. Spatial coherence is in contrast a measure of the correlation of the phases at different points normal to the direction of propagation. In that respect one could call it transverse coherence. The more spatially coherent the light is, the more uniform the wave front is. A perfect point source would be perfectly spatially coherent. An example of spatial coherent wave is presented in Fig. 2.1 (b).

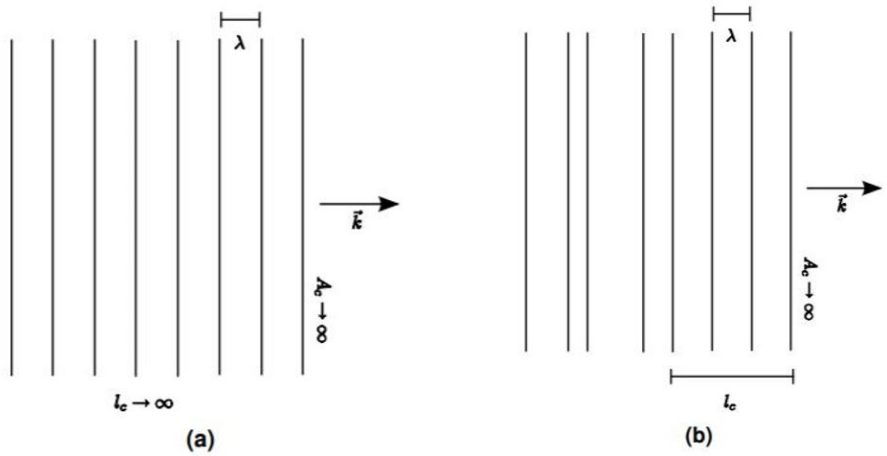

Figure 2.1: Visualisation of different types of coherent light. (a) Light with both infinite coherence length l_c and infinite coherence area A_c. (b) Spatially coherent light with infinite coherence area A_c, but only partially temporal coherence as seen from the finite coherence length l_c. Figure extracted from [45].

Temporal coherence is closely related to the bandwidth of a source, we will explain this in the following part of the chapter. In contrast, the spatial coherence is used to describe the effects due to the (non-point) size of any real source. To conclude, the coherence area A_c is defined as the length of the coherent wave front multiplied with the wavelengths where the profile of the field is unchanged. The coherence area A_c plays an important role in interference experiments since to observe interference when the light passes through two slits, A_c must be large enough to have wave front more or less constant over the slits. If this condition is not fulfilled the interference pattern is lost.

2.1.1 Different type of lights

The concept of "type of light" is linked to a statistical connotation of the fluctuations of the sources which will play an important role in the evaluation of the degree of first-order temporal coherence and the degree of second-order temporal coherence. There are two main types of light sources: coherent light sources and chaotic light sources. A light source is coherent if it emits mostly monochromatic light with a constant relative phase, like a laser source for instance. Then, chaotic sources consist of a very large number of atoms which radiates almost independently of each other, leading to the term chaotic. The frequency and phase of the emitted light is determined by the unstable energy levels of the atoms, the statistical spread in atomic velocities and random collisions between atoms [40]. Thus the statistical properties of chaotic light are profoundly different from that of coherent light. For further simplification, one can adopt the common convention that chaotic light is ergodic. For an ergodic process, any average calculated along a sample function (i.e., a time average of the electric field emitted by a single atom) must equal the same average calculated across the ensemble (i.e., a simultaneous ensemble average over the ν equivalent atoms). A less restrictive demand is that the statistics

governing chaotic light is wide-sense stationary, meaning that the following two conditions are met [22]:

1. $E[u(t)]$ is independent of t.
2. $E[u(t_1)u(t_2)]$ is independent of $\tau = t_2 - t_1$.

where $E[...]$ denotes the expectation value of the random process u(t). So by widesense stationary it is meant that the random fluctuations in the light are governed by processes that do not change with time.

2.2 Classical formulation

The classical statistical theory of light properties is useful for a physical understanding of the nature of the various emitted light properties and the introduction of their quantum version. The aim of this section is to define the *degree of first-order temporal coherence* and *degree of second-order temporal coherence*. We will follow the path traced in [40]. The temporal fluctuation properties of a light beam are measured through optical interference experiments. In particular, the Mach-Zender interferometer measures the first-order interference while the Brown-Twiss interferometer measures the second-order interference. We will analyze them in detail in the next sections. The basic optical component for this kind of experiments is the beam splitter. Starting from the description of its properties we will analyze its usage in the various interference experiments that, finally, enable us to introduce the concept of *degree of first-order temporal coherence* and *degree of second-order temporal coherence*.

2.2.1 The lossless beam-splitter

In Fig. 2.2 a schematic representation of an optical beam-splitter is shown. E_1 and E_2 are the electric fields of the input beams while E_3 and E_4 of the output, both considered monochromatic. All the beams are assumed to have the same linear polarization.

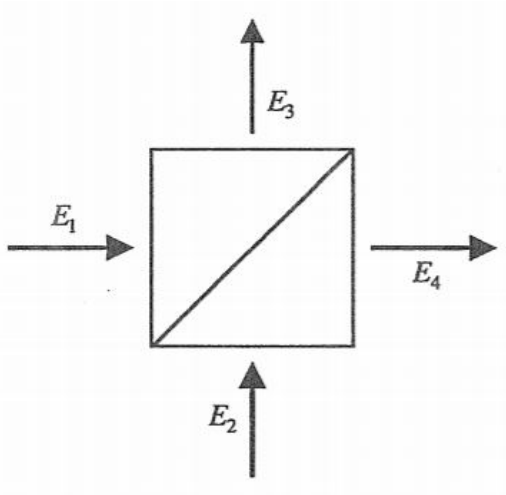

Figure 2.2: Lossless beam-splitter showing the notation for the electric field amplitudes of the input and output beams. [40].

Assuming negligible loss process, the following relation holds

$$E_3 = R_{31}E_1 + T_{32}E_2 \quad \text{and} \quad E_4 = T_{41}E_1 + R_{42}E_2 \tag{2.1}$$

where R and T are complex reflection and transmission coefficient in amplitude for the beam-splitter. Writing down the same relation in matrix form, we have

$$\begin{bmatrix} E_3 \\ E_4 \end{bmatrix} = \begin{bmatrix} R_{31} & T_{32} \\ T_{41} & R_{42} \end{bmatrix} \begin{bmatrix} E_1 \\ E_2 \end{bmatrix} \tag{2.2}$$

where the 2×2 is known as *beam-splitter matrix*. Since we consider negligible any loss process we can equate the total energy flow in the input part to the one in the out, for the energy conservation principle.

$$|E_3|^2 + |E_4|^2 = |E_1|^2 + |E_2|^2 \tag{2.3}$$

that is satisfied for all input fields if

$$|R_{31}|^2 + |T_{41}|^2 = |R_{42}|^2 + |T_{32}|^2 = 1 \quad \text{and} \quad R_{31}T_{32}^* + T_{41}R_{42}^* = 0. \tag{2.4}$$

Now we can divide the coefficients into amplitude and phase part, so using the reflection one as an example we have

$$R_{31} = |R_{31}|\, exp(i\phi_{31}). \tag{2.5}$$

Substituting the above definition into the second part of the equation 2.4 we obtain a constraint both for the phase angles

$$\phi_{31} + \phi_{42} - \phi_{32} - \phi_{41} = \pm\pi \tag{2.6}$$

and the amplitudes

$$|R_{31}| \,/\, |T_{41}| = |R_{42}| \,/\, |T_{32}| \,. \tag{2.7}$$

This relation in conjunction with equation 2.4 proves that the two reflection coefficients have the same magnitude and this holds for the transmission ones too, thus

$$|R_{31}| = |R_{42}| \equiv |R| \quad \text{and} \quad |T_{32}| = |T_{41}| \equiv |T| \,. \tag{2.8}$$

Equations 2.6 and 2.8 constitute the general constraints on the reflection and transmission coefficients of the beam splitter. These constraints impose the beam splitter matrix to be unitary, so we can easily find the inverse by equating it with its complex-conjugate transpose and obtain:

$$\begin{bmatrix} E_1 \\ E_2 \end{bmatrix} = \begin{bmatrix} R_{31}^* & T_{41}^* \\ T_{32}^* & R_{42}^* \end{bmatrix} \begin{bmatrix} E_3 \\ E_4 \end{bmatrix} \tag{2.9}$$

It is important to point out that all the properties we obtained are just derived from the energy conservation principle. To conclude the paragraph, we introduce the symmetrical beam splitter case that will be used for all the subsequent derivations. Symmetric means that the coefficients are chosen to be symmetric, so $\phi_{31} = \phi_{42} = \phi_R$ and $\phi_{32} = \phi_{41} = \phi_T$, where

$$R_{31} = R_{42} \equiv R = |R|\, exp(i\phi_R) \quad \text{and} \quad T_{32} = T_{41} \equiv T = |T|\, exp(\phi_T) \tag{2.10}$$

Under this assumption, the relation 2.4 reduces to

$$|R|^2 + |T|^2 = 1 \quad \text{and} \quad RT^* + TR^* = 0, \quad \text{or} \quad \phi_R - \phi_T = \pm\pi/2. \tag{2.11}$$

If we also assume to have a 50:50 beam splitter where the reflection and transmission coefficients are of equal magnitude, then

$$|R| = |T| = 1/\sqrt{2} \quad \text{with} \quad \phi_R - \phi_T = \pi/2. \tag{2.12}$$

2.2.2 The Mach-Zehnder interferometer and degree of first-order temporal coherence

The treatment of the Mach—Zehnder interferometer provides a simple illustration of some general principles common to all interference experiments and helps introducing the concept of *first degree of temporal coherence*. Figure 2.3 shows a representation of the experiment. Chaotic light from a point source is rendered parallel by means of a lens and then hits the first beam splitter via arm 1. No light is incident via arm 2. Let $E(t)$ be the complex electric field of the incident light beam in arm 1 at the entrance of the first beam splitter. We assume to have perfectly symmetrical beam splitters. Since cahotic light contains a spread of frequencies we also assume that the coefficients of reflection and transmission remain constant throughout this spectrum. The internal path of the interferometer have in general different lenghts and so different travel time and we denote them as z_1 and z_2. Thus when the two beams arrive in the second beam splitter they will be delayed by z_1/c and z_2/c respectively.

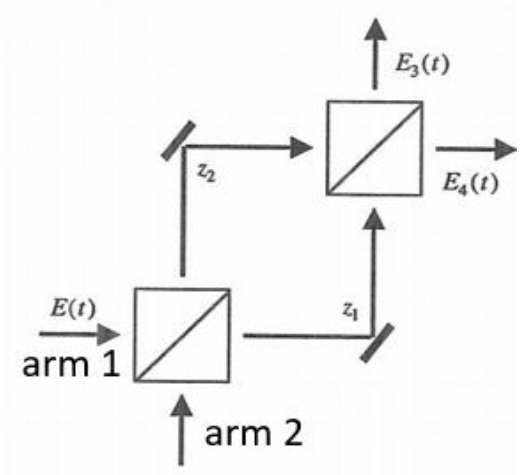

Figure 2.3: Mach-Zender interferometer showing the notation for the input and output electric field amplitudes and for the internal path lenghts. [40]

So in the arm labelled 4 we have

$$E_4(t) = R \times T \times E(t_1) + T \times R \times E(t_2) \tag{2.13}$$

where

$$t_1 = t - (z_1/c) \quad \text{and} \quad t_2 = t - (z_2/c). \tag{2.14}$$

The intensity of the output light, averaged over a cycle of oscillation, is

$$\begin{aligned} \bar{I}_4(t) &= \frac{1}{2}\epsilon_0 c|E_4(t)|^2 = \\ &= \frac{1}{2}\epsilon_0 c|R|^2|T|^2 \left\{|E(t_1)|^2 + |E(t_2)|^2 + 2Re[E^*(t_1)E(t_2)]\right\} \end{aligned} \tag{2.15}$$

Since it is useful to compare theoretical predictions with experiments, we need to average $\left\langle \bar{I}_4(t) \right\rangle$ over an observation period $\mathbf{T}$ much greater than the cahotic light coherence time τ_c, thus

$$\bar{I}_4(t) = \frac{1}{2}\epsilon_0 c|R|^2|T|^2 \left\{\left\langle|E(t_1)|^2\right\rangle + \left\langle|E(t_2)|^2\right\rangle + 2Re\left\langle E^*(t_1)E(t_2)\right\rangle\right\} \tag{2.16}$$

The term that generates the interference pattern is the third one which involves the first order correlation function, written explicitly for the fields at time t_1 and t_2 as

$$\langle E^*(t_1)E(t_2)\rangle = \frac{1}{\mathbf{T}}\int_{\mathbf{T}} dt_1 E^*(t_1)E(t_2) \tag{2.17}$$

We note that it is an integral in one variable since t_1 and t_2 differ by a fixed amount, as we derive from equation 2.14. It is very important to observe that the nature of the field correlation function and so of the interference fringes depends on the type of light incident on the interferometer. If the statistical properties of the light source are stationary then the average in equation 2.17 does not depend on the particular starting time of the period T, provided that T is much longer than the characteristic time scale of the fluctuations. Since the equivalence of time averaging and statistical averaging is valid for light beams whose fluctuations are produced by ergodic random processes, the time averaging in equation 2.17 then samples all of the electric-field values allowed by the statistical properties of the source with their appropriate relative probabilities, and the result is independent of the magnitude of T. Thus, although the experimental effects of the first-order correlation function are manifested by a time averaging, as on the right of equation 2.17, the function is calculated by a statistical average over all values of the fields at times t_1 and t_2. The result does not depend on the time t_1, and the correlation is a function only of the time delay τ between the two field values. Indeed, for the stationary case, we can write

$$\langle E^*(t)E(t+\tau)\rangle = \frac{1}{\mathbf{T}}\int_{\mathbf{T}} dt E^*(t)E(t+\tau) \tag{2.18}$$

We now observe that from the independence from the specific values of t_1 and t_2 but just from the time delay τ between them, we can derive the subsequent property

$$\langle E^*(t)E(t-\tau)\rangle = \langle E^*(t+\tau)E(t)\rangle = \langle E^*(t)E(t+\tau)\rangle^* \tag{2.19}$$

therefore the real part of the correlation function is the same at positive or negative values of the time delay. Finally we can define the *degree of first-order temporal coherence* of stationary light as a normalized version of the first-order correlation function,

$$g^{(1)}(\tau) = \frac{\langle E^*(t)E(t+\tau)\rangle}{\langle E^*(t)E(t)\rangle} \tag{2.20}$$

and then inserting it in equation 2.16 we obtain

$$\left\langle \bar{I}_4(t)\right\rangle = 2|R|^2|T|^2\left\langle \bar{I}(t)\right\rangle\left\{1 + Re\left[g^{(1)}(\tau)\right]\right\} \tag{2.21}$$

where

$$\left\langle \bar{I}(t)\right\rangle = \frac{1}{2}\epsilon_0 c\left\langle |E(t)|^2\right\rangle \tag{2.22}$$

is the averaged input intensity and

$$\tau = (z_1 - z_2)/c. \tag{2.23}$$

From equations 2.19 and 2.20 we derive

$$g^{(1)}(-\tau) = g^{(1)}(\tau)^*. \tag{2.24}$$

2.2.3 The degree of first-order temporal coherence for some concrete models of radiation

We will now compute the degree of first-order temporal coherence for some concrete models of radiation. We will analyse three different radiation models which induces fluctuations in either the relative phase or the angular frequency of the light. These three cases are

1. Lifetime (natural) broadening

2. Collision (pressure) broadening

3. Doppler broadening

and each can be put into two categories. The first two are homogeneous broadening mechanisms while the third is an inhomogeneous broadening mechanism [19]. In general the electric field is on the form

$$E(\mathbf{r},t) = |E(\mathbf{r},t)|e^{i(\mathbf{k}\cdot\mathbf{r}-\omega_k(t)t+\phi(t))}$$

By homogeneous it is meant that all the individual atoms in the light source behave in the same way and produce light of the same angular frequency so only their relative phase is different (i.e., $\omega_k(t) \to \omega_0$ and $\phi(t)$). The latter case is inhomogeneous in the sense that the individual atoms behave differently and produce light with slightly differing angular frequency, while their relative phase remains unchanged (i.e., $\phi(t) \to \phi$ and $\omega_k(t)$).

Light experiencing homogeneous broadening mechanisms will have a Lorentzian frequency distribution [40], yielding the degree of first-order coherence:

$$g^{(1)}(\tau) = exp\{-i\omega_0\tau - (|\tau|/\tau_c)\} \tag{2.25}$$

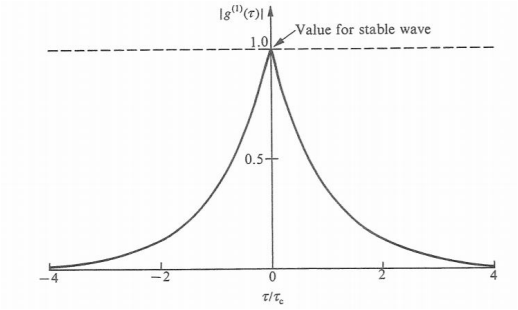

Figure 2.4: The modulus of the degree of first-order coherence of chaotic light with a Lorentzian frequency spectrum [40].

Where ω_0 is the central frequency of the light and τ_c is the coherence time of the light. Light with an inhomogeneous broadening mechanism displays a Gaussian frequency distribution, yielding the degree of first-order coherence

$$g^{(1)}(\tau) = exp\{-i\omega_0\tau - \frac{\pi}{2}(|\tau|/\tau_c)^2\} \tag{2.26}$$

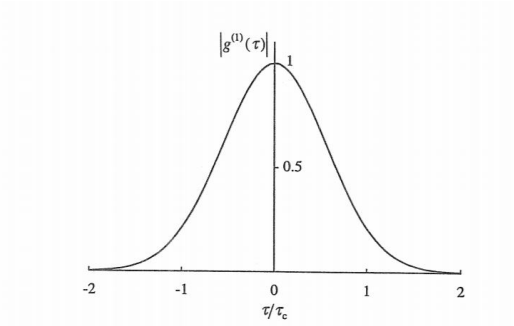

Figure 2.5: The modulus of the degree of first-order coherence of chaotic light with a Gaussian frequency spectrum. [40]

Fig. 2.4 shows the $\left|g^{(1)}(\tau)\right|$ for coherent light and chaotic light with a Lorentzian frequency distribution while and Fig. 2.5 shows the $\left|g^{(1)}(\tau)\right|$ for a chaotic light with a Gaussian frequency

distribution . For both distributions we see that near $\tau = 0$ chaotic light is first-order coherent. For the moment we evaluated the degree of first-order coherence expressed in term of correlation between the fields at different times but at the same position. It is possible to generalize it [40] in terms of space-time (z, t), assuming a plane parallel light beam, as

$$g^{(1)}(z_1, t_1; z_2, t_2) = \frac{\langle E^*(z_1, t_1) E(z_2, t_2) \rangle}{[\langle |E^*(z_1, t_1)|^2 \rangle \langle |E^*(z_2, t_2)|^2 \rangle]^{\frac{1}{2}}} \tag{2.27}$$

where for

$$|g^{(1)}(z_1, t_1; z_2, t_2)| \begin{cases} = 1 & \text{the light is first-order coherent.} \\ = 0 & \text{the light is incoherent.} \\ \neq 0, 1 & \text{partially coherent.} \end{cases} \tag{2.28}$$

Since the fluctuations in a parallel light beam in free space propagate at velocity c without any change in their form, the expressions for the $g^{(1)}(\tau)$ of stationary light derived above are simply converted by a redefinition of the delay time as

$$\tau = t_2 - t_1 - \frac{z_2 - z_1}{c} \tag{2.29}$$

Replacing this definition of τ in 2.20 the relation still holds and it is easy to see that

$$g^{(1)}(0) = 1 \tag{2.30}$$

The field correlations in any chaotic light must vanish for times t much longer than τ_c, in fact, since

$$\langle E(t) \rangle = 0 \tag{2.31}$$

it follows that the $g^{(1)}(\tau)$ must have a limiting value

$$g^{(\tau)} \to 0 \quad \text{for} \quad \tau \gg \tau_c \tag{2.32}$$

The light at such well separated space—time points is incoherent.

2.2.4 Physical interpretation of the degree of first-order temporal coherence

Visibility

To understand the physical meaning of $g^{(1)}(\tau)$ we need to introduce the concept of "visibility" of the interference pattern. This pattern forms when two (or more) light waves overlap. Visibility measures the contrast between the bright and dark fringes and it is defined as

$$V = \frac{\langle I \rangle_{\max} - \langle I \rangle_{\min}}{\langle I \rangle_{\max} + \langle I \rangle_{\min}} \tag{2.33}$$

where $\langle I_{max} \rangle$ and $\langle I_{min} \rangle$ represent the maximum and minimum intensity of the fringes. In fact, the visibility can be interpreted as a measure of the coherence between the two fields or between the same field at two different times. It can be proven that the intensity of two overlapped electric fields can be written in terms of the degree of first-order coherence [40], essentially meaning that

$$V \sim \left| g^{(1)}(\tau) \right| \tag{2.34}$$

thus, the visibility is proportional to the magnitude of the first degree of coherence. So from equation 2.28 the maximum visibility of the fringes is obtained when the two light beams are

completely coherent, so when $g^{(1)}(\tau) = 1$. For maximal contrast we mean that the dark fringes are totally dark due to perfect destructive interference. If the two light beams are incoherent, the contrast of the fringes is zero and there are no discernible darker and lighter patches. That is, if the light beams are incoherent there will be no visible interference pattern.

Relation between $g^{(1)}(\tau)$ and the frequency spectrum

Another important information about $g^{(1)}(\tau)$ comes from its relation with the frequency spectrum of the emitted light through Wiener-Khinchin theorem that will be developed briefly in this section. Firstly, computing the Fourier transform of an electric field $E(t)$ over the integration range T, we obtain

$$E_T(\omega) = \frac{1}{\sqrt{2\pi}} \int_T \mathrm{d}t E(t) e^{i\omega t} \tag{2.35}$$

The power spectral density of an electromagnetic wave is defined as

$$f(\omega) = \frac{|E_T(\omega)|^2}{T} = \frac{1}{2\pi T} \iint_T E^*(t) E(t') \, e^{-i\omega(t-t')} \mathrm{d}t \mathrm{d}t' \tag{2.36}$$

From the definition of $g^{(1)}(\tau)$ it can be proven that the normalized spectrum is [45]:

$$S(\omega) = \frac{1}{\pi} \mathrm{Re} \int_0^\infty g^{(1)}(\tau) e^{i\omega\tau} \mathrm{d}\tau \tag{2.37}$$

This relation is known as the Wiener-Khinchin theorem. Thus, the shape of the spectral lines can be predicted through the relationship between the normalised power spectral density and the degree of first-order coherence. If the broadening of a spectral line is due to Doppler shifts, the line will have an approximately Gaussian shape [45]:

$$S_G(\omega) = \frac{1}{2\pi} \int_{-\infty}^{\infty} e^{-\left[\left(\pi/2\tau_c^2\right)\tau^2 - i(\omega-\omega_0)\tau\right]} \mathrm{d}\tau = \frac{\sqrt{2}\tau_c}{\pi} e^{-(2/\pi)(\omega-\omega_0)^2\tau_c^2} \tag{2.38}$$

where ω_0 is the average frequency of the radiated light. If the radiation is mainly due to collisions between atoms or molecules, the spectral lines will have a Lorentzian shape [45]:

$$S_L(\omega) = \frac{2\tau_c/\pi}{1 + 4\left(\omega - \omega_0\right)^2 \tau_c^2} \tag{2.39}$$

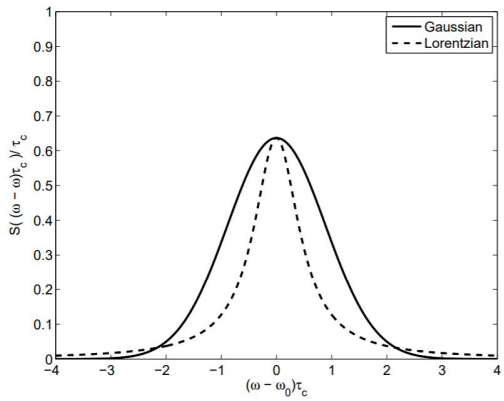

Figure 2.6: The normalised power spectral density $S(\omega)$ with both Gaussian and Lorentzian lineshape. [45]

Both the Gaussian and the Lorentzian line shapes are shown in Fig. 2.6. Doing an inverse Fourier transformation one can go from the power spectral density to the degree of first-order coherence. This can be very helpful since, often, it could be easier to measure the coherence of a signal rather than its power density spectrum. In conclusion, it is possible to find a simple relation between the width of the frequency spectrum and the coherence time by calculating the Full Width Half Maximum (FWHM). For light with a Gaussian frequency distribution, we obtain [45]:

$$\mathrm{FWHM}_G : \Delta\omega = \omega'_+ - \omega'_- = \frac{\sqrt{2\pi \ln 2}}{\tau_c} \tag{2.40}$$

A similar calculation yields the FHWM for light with a Lorentzian frequency distribution

$$\mathrm{FWHM}_L : \Delta\omega = \omega'_+ - \omega'_- = \frac{2}{\tau_c} \tag{2.41}$$

So in both cases the width of the frequency band is inversely proportional to the coherence time of the light, meaning that a decrease in $\Delta\omega$ increases the coherence time τ_c.

2.2.5 The degree of second-order temporal coherence

The degree of second-order coherence plays a crucial role in the distinction between light beams that can or cannot be described by classical theory. To derive the intensity-fluctuation properties of chaotic light in a similar way as what was done for the field-fluctuation in the previous section, we consider two-time measurements in which many pairs of readings of the intensity are taken at a fixed point in space, with a fixed time delay τ. For simplicity light with just one fixed polarization. The average of the product of each pair of readings is the intensity correlation function of the light, analogous to the electric-field correlation found in 2.17. The normalised form of the correlation function is called the degree of second-order temporal coherence and can be written as [40]:

$$g^{(2)}(\tau) = \frac{\left\langle \bar{I}(t)\bar{I}(t+\tau)\right\rangle}{\bar{I}^2} = \frac{\langle E^*(t)E^*(t+\tau)E(t+\tau)E(t)\rangle}{\langle E^*(t)E(t)\rangle^2} \tag{2.42}$$

where

$$\begin{aligned} \bar{I} \equiv \langle \bar{I}(t)\rangle &= \frac{1}{2}\epsilon_0 c \langle E^*(t)E(t)\rangle = \frac{1}{2}\epsilon_0 c \sum_{i=1}^{\nu} \langle E_i^*(t)E_i(t)\rangle \\ &= \frac{1}{2}\epsilon_0 c \left\langle \left| E_1 e^{i\phi_1(t)} + E_2 e^{i\phi_2(t)} + \ldots + E_\nu e^{i\phi_\nu(t)} \right|^2 \right\rangle \\ &= \sum_{i=1}^{\nu} \frac{1}{2}\epsilon_0 c\nu E_i^2 \quad (i = 1, 2, \ldots, \nu) \end{aligned} \tag{2.43}$$

is the long-time average intensity in a plane parallel light beam radiated by ν atoms.

Since the light beam consists on indipendent contributions of ν equivalent radiating atoms, the total electric field can be written as

$$\begin{aligned} E(t) &= E_1(t) + E_2(t) + \ldots + E_\nu(t) \\ &= E_0 e^{-i\omega_0 t}\left[e^{i\phi_1(t)} + e^{i\phi_2(t)} + \ldots + e^{i\phi_\nu(t)}\right] \end{aligned} \tag{2.44}$$

The cross-terms between different sources gives a zero average contribution to $\bar{I}$, due to the random distribution of the phases $\phi_i(t)$.

Now, we are interested on the limiting values of $g^{(2)}(\tau)$. We start by considering the variance of the intensity.

$$(\Delta\bar{I}(t))^2 = \left\langle \bar{I}(t)^2 \right\rangle - \langle \bar{I}(t) \rangle^2 \tag{2.45}$$

The variance must be greater than or equal to zero by definition, so that

$$\left\langle \bar{I}(t)^2 \right\rangle \geq \langle \bar{I}(t) \rangle^2 \tag{2.46}$$

Thus

$$\bar{I}^2 \equiv \langle \bar{I}(t) \rangle^2 \leq \left\langle \bar{I}(t)^2 \right\rangle . \tag{2.47}$$

It implies that for $\tau = 0$

$$g^{(2)}(0) = \frac{\left\langle \bar{I}(t)^2 \right\rangle}{\bar{I}^2} \geq 1 \tag{2.48}$$

It is not possible to establish an upper limit but the complete range of allowed value is

$$1 \leq g^{(2)}(0) \leq \infty. \tag{2.49}$$

While for time delays different from zero the positive nature of the intensity lust gives the restriction

$$0 \leq g^{(2)}(\tau) \leq \infty, \quad \tau \neq 0 \tag{2.50}$$

Using the Cauchy-Schwarz inequality, where

$$\bar{I}(t)^2 + \bar{I}(t+\tau)^2 \geq 2\bar{I}(t)\bar{I}(t+\tau) \tag{2.51}$$

we obtain an other important property of $g^{(2)}(\tau)$. Indeed, it can be shown that [40]:

$$g^{(2)}(\tau) \leq g^{(2)}(0) \tag{2.52}$$

meaning that the degree of second-order coherence can therefore never exceed its value for zero time delay.

2.2.6 Second-degree of temporal coherence for an ideal plane wave and for chaotic light

Plane Wave

For an ideal plane wave propagating in the z-direction with a constant amplitude E_0 and phase ϕ the degree of second-order coherence is on a particularly simple form. So for

$$E(z,t) = E_0 e^{i(kz-\omega_0 t)} \tag{2.53}$$

we have [40]

$$g^{(2)}(\tau) = \frac{\langle E^*(t)E^*(t+\tau)E(t+\tau)E(t)\rangle}{\langle E^*(t)E(t)\rangle^2} = 1 \tag{2.54}$$

We knew that such a stable wave is first-order coherent at all space-time points. It is said to be second-order coherent if simultaneously

$$\left|g^{(1)}(\tau)\right| = 1 \quad \text{and} \quad g^{(2)}(\tau) = 1. \tag{2.55}$$

It can be shown that the classical stable wave is *nth-order* coherent with $g^{(n)}(\tau) = 1$, hence it is often called just coherent light.

Chaotic light

If the chaotic lights source consists of ν radiating atoms, each of which is not correlated with any of the others, it can be shown that [40], in good approximation

$$\langle E^*(t)E^*(t+\tau)E(t+\tau)E(t)\rangle = \nu^2\left[\langle E_i^*(t)E_i(t)\rangle^2 + |\langle E_i^*(t)E_i(t+\tau)\rangle|^2\right] \tag{2.56}$$

Observing that the rightmost term corresponds to the definition of the first-order correlation function, implying that the degree of second-order coherence can be related to the degree of first-order coherence, see equation 2.20, as

$$g^{(2)}(\tau) = 1 + \left|g^{(1)}(\tau)\right|^2, \quad \nu \gg 1 \tag{2.57}$$

Now, using the limiting values for $g^{(1)}(\tau)$, see equation 2.30 and 2.32, we obtain the upper value of $g^{(1)}(\tau)$, that is

$$g^{(2)}(0) = 2 \tag{2.58}$$

and

$$g^{(2)}(\tau) \to 1 \text{ for } \tau \gg \tau_c \tag{2.59}$$

These limits are only valid for chaotic light. The statistical distributions of collision broadened (Lorentzian) and Doppler broadened (Gaussian) light are inserted into equation 2.57, to obtain respectively [40]

$$g^{(2)}(\tau) = 1 + e^{-2|\tau|/\tau_c} \tag{2.60}$$

and

$$g^{(2)}(\tau) = 1 + e^{-\pi(\tau/\tau_c)^2} \tag{2.61}$$

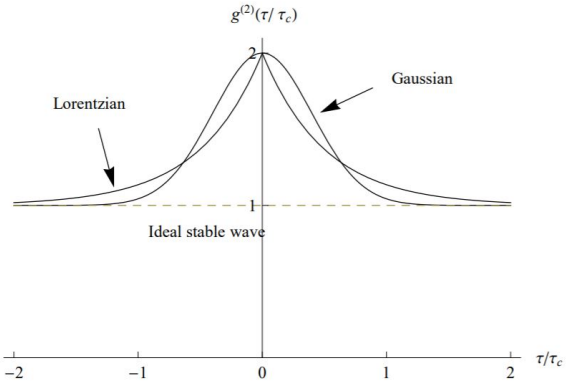

Figure 2.7: A representation of the degrees of second-order coherence of chaotic light having Lorentzian and Gaussian frequency distribution with coherence time τ_c. The dashed line shows the constant unit $g^{(2)}(\tau)$ of coherent light (ideal plane wave). [40]

Fig. 2.7 shows the behaviour of $g^{(2)}(\tau)$ for the different distributions. According to equation 2.55, chaotic light is not second-order coherent. While Fig. 2.4 and 2.5 show that chaotic light is first-order coherent for very short values of τ , such short times produces a degree of second-order coherence equal to 2, and criterion equation 2.55 cannot be fulfilled. Therefore chaotic light is second-order incoherent for any pairs of space-time points.

2.3 Quantum formulation

In the previous part the electromagnetic field was treated as a classical field. The classical theory is a successful one in the sense that it accounts for a variety of optical phenomena, especially those dealing with wave propagation, interference and diffraction. However, there are some effects that can only be accounted for by quantum mechanics,like photon anti-bunching and indistinguishability. These discussion is saved for the end of chapter. Thus the classical degrees of first- and second-order coherence must be translated to a quantum mechanical coherence theory. But first the free electromagnetic field needs to be quantised using field operators. This is an essential tool in developing the framework to study the quantum correlations of light. We will just present how the degrees of first- and second-order coherence functions will be rewritten in terms of field operators. For the full treatment of the quantum formulation, please see [40]. It will be shown that the degree of second-order coherence in fact turns out to be a measure of the classical nature of light. The last section, then, briefly discusses the quantum Hanbury Brown-Twiss effect and how the intensity interferometer can be interpreted in quantum mechanics.

2.3.1 Quantum first and second-degree of temporal coherence

The quantised electric field operator then takes the form [45]

$$\hat{\mathbf{E}}(\mathbf{r},t)=\sum_{\mathbf{k}}\sum_{\lambda}\left(\frac{\hbar\omega_k}{2\epsilon_0 L^3}\right)^{1/2}\hat{\epsilon}_{\mathbf{k}\lambda}\left[\hat{a}_{\mathbf{k}\lambda}e^{i(\mathbf{k}\cdot\mathbf{r}-\omega_k t)}+\hat{a}^{\dagger}_{\mathbf{k}\lambda}e^{-i(\mathbf{k}\cdot\mathbf{r}-\omega_k t)}\right] \tag{2.62}$$

That, as we see, it is written in terms of creation and annihilation operators and thus it can be convenient to write down the quantised electric field as composed by two terms:

$$\hat{\mathbf{E}}(\mathbf{r},t)=\hat{\mathbf{E}}^{(+)}(\mathbf{r},t)+\hat{\mathbf{E}}^{(-)}(\mathbf{r},t) \tag{2.63}$$

Thus separating the positive and negative frequency parts of the electric field operator, where

$$\begin{aligned}\hat{\mathbf{E}}^{(+)}(\mathbf{r},t)&=\sum_{\mathbf{k}}\sum_{\lambda}\left(\frac{\hbar\omega_k}{2\epsilon_0 L^3}\right)^{1/2}\hat{\epsilon}_{\mathbf{k}\lambda}\hat{a}_{\mathbf{k}\lambda}e^{i(\mathbf{k}\cdot\mathbf{r}-\omega_k t)}\\ \hat{\mathbf{E}}^{(-)}(\mathbf{r},t)&=\sum_{\mathbf{k}}\sum_{\lambda}\left(\frac{\hbar\omega_k}{2\epsilon_0 L^3}\right)^{1/2}\hat{\epsilon}_{\mathbf{k}\lambda}\hat{a}^{\dagger}_{\mathbf{k}\lambda}e^{-i(\mathbf{k}\cdot\mathbf{r}-\omega_k t)}\end{aligned} \tag{2.64}$$

So $\hat{\mathbf{E}}^{(+)}(\mathbf{r},t)$ contains only the annihilation operators and its adjoint, $\hat{\mathbf{E}}^{(-)}(\mathbf{r},t)$, contains only the creation operators. It is important to point out that the annihilation operator, $\hat{a}_{k\lambda}$, decreases the number of particles in the mode k with for the direction λ, thus in the state $|n_{k\lambda}\rangle$ by one, while the creation operator, $\hat{a}^{\dagger}_{k\lambda}$, increases their number by one. These operators, respect the commutation rules:

$$\begin{aligned}&[\hat{a}_{\mathbf{k}\lambda},\hat{a}_{\mathbf{k}'\lambda'}]=\left[\hat{a}^{\dagger}_{\mathbf{k}\lambda},\hat{a}^{\dagger}_{\mathbf{k}'\lambda'}\right]=0\\ &\left[\hat{a}_{\mathbf{k}\lambda},\hat{a}^{\dagger}_{\mathbf{k}'\lambda'}\right]=\delta_{\mathbf{k}\mathbf{k}'}\end{aligned} \tag{2.65}$$

After the quantisation of the electromagnetic field using field operators one can write the first-degree of temporal coherence for a stationary field as [40]:

$$g^{(1)}(\tau)=\frac{\left\langle\hat{E}^{(-)}(t)\hat{E}^{(+)}(t+\tau)\right\rangle}{\left\langle\hat{E}^{(-)}(t)\hat{E}^{(+)}(t)\right\rangle} \tag{2.66}$$

While the second-degree of temporal coherence as [40]:

$$g^{(2)}(\tau) = \frac{\left\langle \hat{E}^{(-)}(t)\hat{E}^{(-)}(t+\tau)\hat{E}^{(+)}(t+\tau)\hat{E}^{(+)}(t) \right\rangle}{\left\langle \hat{E}^{(-)}(t)\hat{E}^{(+)}(t) \right\rangle^2} \tag{2.67}$$

2.3.2 The value of $g^{(2)}(0)$ for a single photon source

In this section we briefly comment the connection between the second-degree correlation function and single photon sources. We will prove that if $g^{(2)}(\tau = 0) < \frac{1}{2}$ then the source is a single photon source. In particular, it is possible to prove that any quantum state, for which the second-order correlation function falls below 1/2, has a nonzero projection on the single-photon Fock state [23], this proof is out of the aim of the project.

Proof that $g^{(2)}(0) < \frac{1}{2}$ for a single photon source

For any given Fock state (Focks states are number states) $|n\rangle, n \geq 1$, it is possible to calculate [23]:

$$g^{(2)}(0) = \frac{n-1}{n} = 1 - \frac{1}{n}. \tag{2.68}$$

Thus, for any Fock state with $n > 1$, $g^{(2)}(0)$ will be greater or equal to one half. For the vacuum state $|0\rangle$, and in the limit of coherent states we can define $g^{(2)}(0) := 1$. Thus, all Fock states besides $|1\rangle$ follow the rule $g^{(2)}(0) \geq 1/2$, while for $|1\rangle$, we obtain $g^{(2)}(0) = 0$.

Non-zero projection on the single-photon Fock state

The proof of the fact that any quantum state, for which the second-order correlation function falls below 1/2, has a nonzero projection on the single-photon Fock state is quite easy for the limited case of a pure state. Indeed, since any pure quantum state can be written in the Fock basis as a linear combination [23], then, if a superposition of two arbitrary states with disjoint Fock statistics can not yield a lower $g^{(2)}$ than either of its constituents, the proof of the above conjecture would be completed for pure states. The proof for any quantum states can be processed providing a general link between the value of the second-order correlation function and the quantum state projection on the single-photon Fock state [23].

2.3.3 The Hanbury Brown-Twiss effect in classical and quantum treatment and the concept of indistiguishibility and antibunching

In physics, the Hanbury Brown and Twiss (HBT) effect is the correlation and anti-correlation effects in the intensities received by two detectors from a beam of particles (or photons). Indeed, in 1954 Hanbury Brown and Twiss showed that one could measure the angular sizes of astronomical radio sources and stars starting from the analysis of the correlations of the signal intensities, rather than the amplitudes, in independent detectors. A schematic representation of the Hanbury Brown and Twiss interferometer setup is depicted in Fig. 2.8. Their subsequent correlation experiments demonstrated how this measurement is linked with quantum bunching of photons in incoherent light beams [3]. We will analyze it in detail in the quantum formulation of the Hanbury Brown and Twiss (HBT) effect. Indeed, the HBT effect can be predicted even by treating the incident electromagnetic radiation as a classical wave [4].

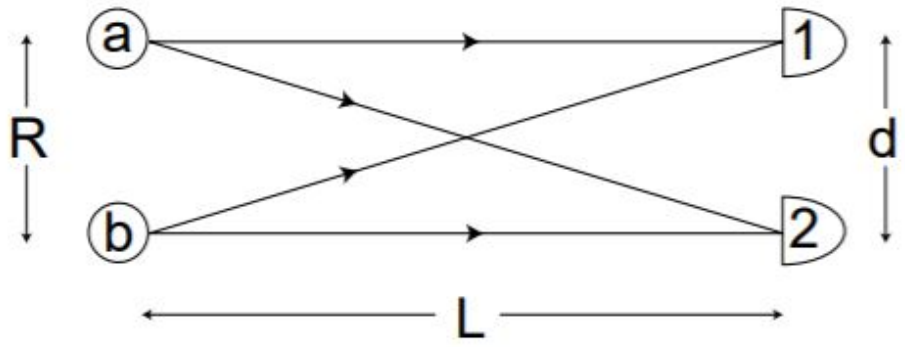

Figure 2.8: Measurement of the separation of two sources, a and b, by correlation of intensities in detectors 1 and 2, figure extracted from [3].

Classical HBT effect

We suppose to have a monochromatic wave with frequency ω hitting on two independent detectors, with an amplitude $E(t)$ that varies on timescales slower than the wave period $2\pi/\omega$. Since the detectors are separated and independent, we assume that the signal arrives to the second detector delayed by a time τ, or equivalently, a phase $\phi = \omega\tau$;, with respect to the first detector; that is [3]

$$\begin{aligned} E_1(t) &= E(t)\sin(\omega t) \\ E_2(t) &= E(t-\tau)\sin(\omega t - \phi) \end{aligned} \tag{2.69}$$

The intensity recorded by the detectors is the square of the amplitude averaged over a timescale that is short compared to the fluctuations in the field $E(t)$ but long compared to the wave period $2\pi/\omega$:

$$\begin{aligned} i_1(t) &= \overline{E_1(t)^2} = \overline{E(t)^2\sin^2(\omega t)} = \tfrac{1}{2}E(t)^2 \\ i_2(t) &= \overline{E_2(t)^2} = \overline{E(t-\tau)^2\sin^2(\omega t - \phi)} = \tfrac{1}{2}E(t-\tau)^2 \end{aligned} \tag{2.70}$$

where the over line indicates this time averaging. The correlation function $\langle i_1 i_2\rangle(\tau)$ of these time-averaged intensities can then be calculated as:

$$\begin{aligned} \langle i_1 i_2\rangle(\tau) &= \lim_{T\to\infty}\frac{1}{T}\int_0^T i_1(t)i_2(t)\mathrm{d}t \\ &= \lim_{T\to\infty}\frac{1}{T}\int_0^T \frac{1}{4}E(t)^2E(t-\tau)^2\mathrm{d}t \end{aligned} \tag{2.71}$$

One can show rather the correlation in intensity fluctuations at the two detectors, instead of the intensities correlation, since it is not too difficult to see that if the intensities are correlated, then the fluctuations $\Delta i = i - \langle i\rangle$, where $\langle i\rangle$ is the average intensity, will be correlated too, as

$$\begin{aligned} \langle \Delta i_1 \Delta i_2\rangle &= \langle (i_1 - \langle i_1\rangle)(i_2 - \langle i_2\rangle)\rangle = \langle i_1 i_2\rangle - \langle i_1\langle i_2\rangle\rangle - \langle i_2\langle i_1\rangle\rangle + \langle i_1\rangle\langle i_2\rangle . \\ &= \langle i_1 i_2\rangle - \langle i_1\rangle\langle i_2\rangle \end{aligned} \tag{2.72}$$

In the simple case where the field $E(t)$ consists mainly of a steady field E_0 with a small sinusoidally varying component $\delta E\sin(\Omega t)$, the time-averaged intensities are easy to compute [72]

$$\begin{aligned} i_1(t) &= \tfrac{1}{2}E_0^2 + E_0\delta E\sin(\Omega t) + \mathcal{O}(\delta E^2) \\ i_2(t) &= \tfrac{1}{2}E_0^2 + E_0\delta E\sin(\Omega t - \Phi) + \mathcal{O}(\delta E^2) \end{aligned} \tag{2.73}$$

with $\Phi = \Omega\tau$, and $\mathcal{O}(\delta E^2)$ represents terms proportional to $(\delta E)^2$, which are small and may be ignored. Thus the correlation function of these two intensities is [72]:

$$\begin{aligned}\langle \Delta i_1 \Delta i_2 \rangle (\tau) &= \lim_{T\to\infty} \frac{(E_0\delta E)^2}{T} \int_0^T \sin(\Omega t)\sin(\Omega t - \Phi)\mathrm{d}t \\ &= \frac{1}{2}(E_0\delta E)^2 \cos(\Omega\tau)\end{aligned} \tag{2.74}$$

showing a sinusoidal non-zero dependence on the delay τ between the two detectors. So, the Hanbury Brown-Twiss effect gives an enhanced relative intensity correlation between chaotic light beams incident on two (photo) detectors, and this effect is not seen for coherent sources.

Quantum HBT effect

Thus for radio astronomy, the classical electromagnetism interpretation was considered sufficient for the description of this interference effect. However, applying the concept to optical wavelength dimensions it is not trivial. Indeed, the quantum description of the effect is less intuitive: if one supposes that a thermal or chaotic light source randomly emits photons, then it is not obvious how the photons could understand that they should arrive at a detector in a correlated way. We will briefly review the quantum version of the HBT effect and see how coincidence counting of photons led to the discovery of photon bunching and its relation to the degree of second-order coherence.

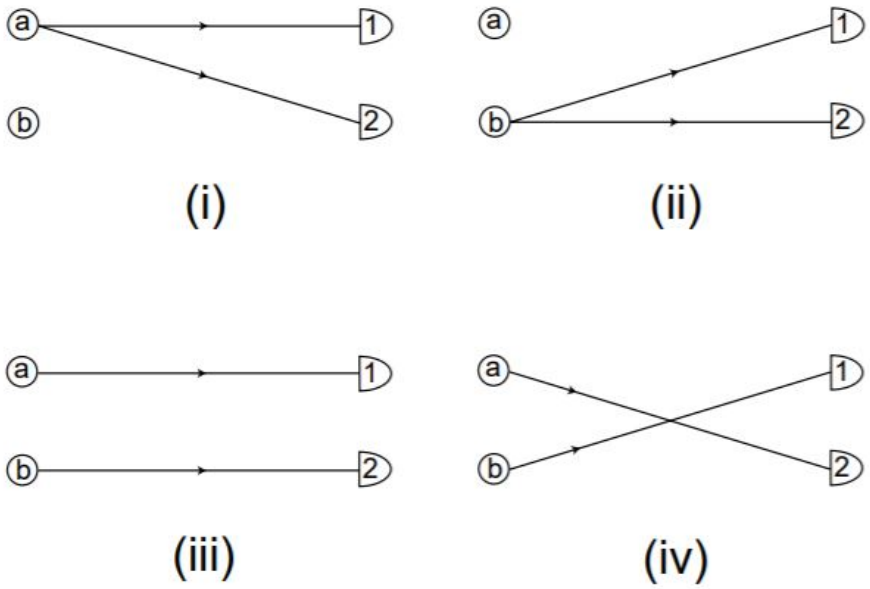

Figure 2.9: The four independent photon emission and detection processes, figure extracted from [3].

Let's move now to the quantum interpretation. Consider two source atoms a and b initially in excited states without any phase correlation. They emit photons which are absorbed by the atoms 1 and 2, considered as detectors. There are four combinations that will lead to excitations of 1 and 2, and assuming that each detector can only be excited by one photon at a time [45]: (i) atom a can emit two photons that are detected at 1 and 2, respectively, and (ii) b can emit two photons that are detected at 1 and 2. These processes are distinguishable and do not lead to any interference. (iii) Atom a can emit a photon detected at 1, with b emitting a photon detected in 2. (iv) Atom a can emit a photon detected at 2, with b emitting a photon

detected in 1. A schematic illustration of the four possible events is shown in Fig. 2.9. It is not possible to distinguish events (iii) and (iv) since photons are,indeed, "indistinguishable" particles. Thus the system state vector is a superposition of (iii) and (iv), and it can be written as:

$$|1,2\rangle = \frac{1}{\sqrt{2}}[|a \to 1, b \to 2\rangle + |b \to 1, a \to 2\rangle] \tag{2.75}$$

and this represents the origin of the correlation observed in the quantum Hanbury Brown-Twiss effect. Thus, the probability that 1 is excited in presence of the sources a and b is the sum of the probabilities that 1 is excited by a without b present and by b without a present, so [45]:

$$P_1 = P(a \to 1) + P(b \to 1) \tag{2.76}$$

in a similar way, we can compute the probability that 2 is excited, P_2. As explained in [16], the probability of excitation of both 1 and 2, $P_{1,2}$, is not just equal to the product P_1P_2, instead $P_{1,2}$ is an oscillatory function of the distance between 1 and 2, provided the two excitations are close enough in time. This result is in complete agreement with the classical description provided in the previous section. Now, we can make a switch of variables since the probability distribution of an excitation over time is equivalent to a counting distribution of n photons detected. Thus, we define a "coincidence" as a combined detection of a photon at 1 and 2 simultaneously, where "simultaneous" means within some short time τ according to the resolution time of the setup. If the counter N registers a coincidence when two photons arrive at $1, 2$, the average coincidence rate is

$$\bar{N} = 2\bar{N}_1\bar{N}_2\tau\left[1 + 1/2\left|g^{(1)}(0)\right|^2\right] \tag{2.77}$$

where $\bar{N}_{1(2)}$ is the average counting rate of photons arriving at 1(2). This result holds just for a resolving time much shorter than the coherence time, so if the light is not first-order coherent, then the coincidence rate is simply the expected rate for two uncorrelated streams of photons $2\bar{N}_1\bar{N}_2\tau_1$. But if the light is at least partially first-order coherent $\left(\left|g^{(1)}(0)\right| > 0\right)$, there is an excess in the coincidence rate which varies directly with the degree of first-order coherence [45], and we say the photons tend to arrive in "clumps". Recall that classical chaotic light is partially first-order coherent for small τ.
To conclude, so the problem with applying the intensity interferometer on light, it is that at optical wavelengths the energies would require the light to be quantised in a relatively small number of photons. It would then not be correct to use Maxwell's equations on light waves and only introduce quantisation through the discrete energy levels in the photodetectors [45]. Thus, in quantum interpretation, instead, light is interpreted in terms of photons and the enhanced intensity correlation imply that the photon's arrival at the two separated detectors is correlated. This is the quantum Hanbury Brown and Twiss effect.

Antibunching

The antibunching dip of the correlation function is based on the fact that a single emitter can only emit one photon at a time. The process can easily be described using a simplified two-level energy diagram, where a molecule in an excited state requires a finite amount of time before it relaxes back to the ground state by emitting a photon. The temporal separation between adjacent photons is therefore determined mostly by the excited-state lifetime. This effect is known as antibunching [54]. The observation of antibunching reveals whether there is only a single photon emitter present in a sample. The antibunching experiment is pratically the measurement of the $g^{(2)}(\tau)$, for a zero delay and the proof that its value is lower than 1/2. This is the experiment we will perform on the localized defect-bound excitons in Chapter 5.

In the previous section we introduced the HBT interferometer which enables us to measure the $g^{(2)}(\tau)$. Moreover, light can be classified with respect to its degree of second-order coherence, $g^{(2)}(\tau)$. In fact, it can be categorised as random , bunched or antibunched. Tthis means is that if in an experimental setup a stream of photons is sent at a detector, there will be different probabilities of detecting a photon at a time τ when a photon was detected earlier, at $t = 0$ [45]. This section takes a closer look at what this entails.

Random light

For a random light it can be shown that the following relation holds [45]:

$$g^{(2)}(\tau) = \left|g^{(1)}(\tau)\right|^2 = 1 \quad \text{for all} \quad \tau \tag{2.78}$$

Thus if a photon is detected at time $t = 0$ there is an equal probability that another photon is detected at any time τ. This can be interpreted as if the spacing between the emitted photons is totally random and that explains the classification.

Bunched light

Light is said to be bunched when

$$g^{(2)}(0) > 1 \text{ and } g^{(2)}(\tau) < g^{(2)}(0) \tag{2.79}$$

meaning that a detection of a second photon is much more likely to occur for shorter time delays τ than for longer ones. Since the intensity interferometer measures $g^{(2)}(\tau)$, it could provide the first experimental evidence for photon bunching. Thus photon bunching is also known as the Hanbury Brown-Twiss effect. Finally is now explained the arrival of photons in "clumps", which now is clearly linked with the quantum degree of second-order coherence.

Antibunched light

As opposed to coherent and bunched light, for antibunched light the following relation holds

$$g^{(2)}(0) < 1 \text{ and } g^{(2)}(\tau) > g^{(2)}(0) \tag{2.80}$$

which can be interpreted as if the detection of a second photon is much more likely to occur for larger values of τ, i.e., the longer one waits. The experimental proof of antibunched light is not trivial. Although for a source consisting of a single atom antibunching is fairly intuitive, since the relaxed atom needs some time to be re-excited and emit again. The different types of light are depicted in Fig. 2.10.

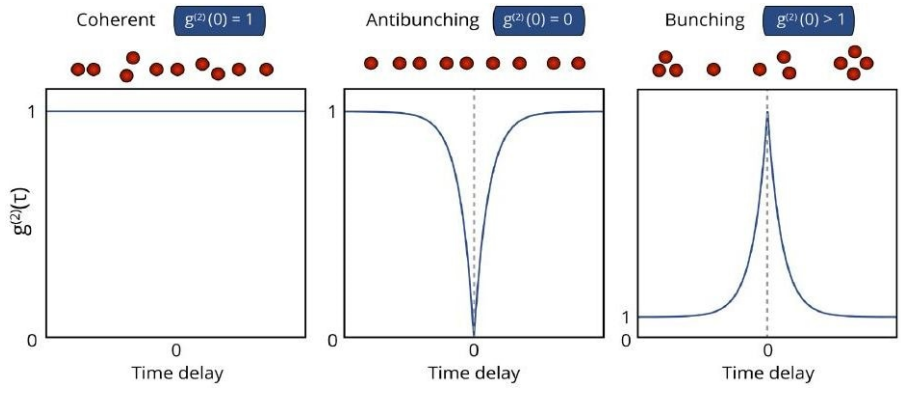

Figure 2.10: Illustration of $g^{(2)}(\tau)$ for bunched light, random light and antibunched light, figure extracted from [51].

Chapter 3

Fibers

In this chapter we explain the basic properties of fiber optics, as well as the coupling between the guided modes and a radiative mode. Indeed, the latter is one of the aims of our project. Thus in this chapter we will present a brief review of the theoretical notions needed for a good comprehension of the process of coupling we will see in Chapter 5. Optical fibers are dielectric waveguides composed by the core that is surrounded by a glass or a plastic layer called cladding which is characterized by a lower refractive index compared to the core refractive index. This difference is the responsible of the confinement and transmission of the light in the fiber, since it provides the conditions for total internal reflection.

3.1 Principle of operation

The propagation of light in an optical fiber can be described in two main ways [58]. If the diameter of the core where the light propagates is much larger compared to the wavelength of the light, a geometrical (or ray optics) approach can be appropriate to describe some of the properties of the fiber. However, in many cases, it is necessary to use electromagnetic theory to describe the set of electromagnetic waves propagating in the fiber, called the modes of the fiber [1].

3.1.1 Ray optics representation

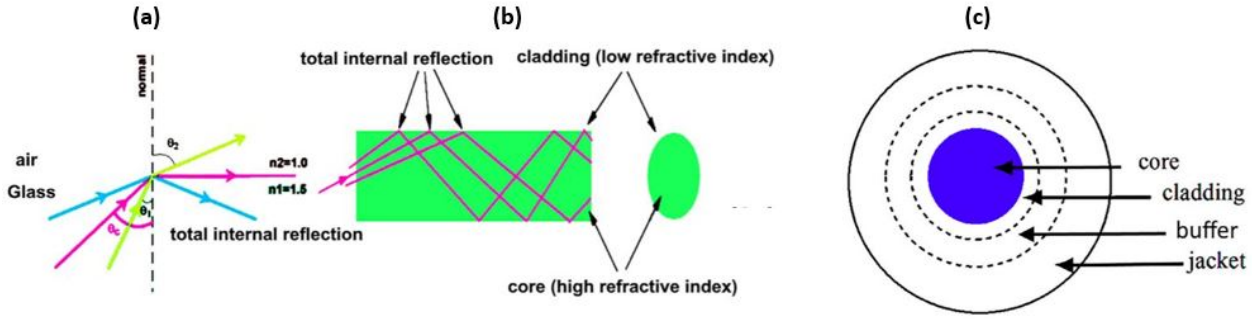

Figure 3.1: Total internal reflection, (a) in glass and air media, (b) in fiber structure which has two glass media with different refractive indices; (c) Structure of optical fiber including four sections as core, cladding, buffer, and jacket. Figures extracted from [1].

Following the analysis presented in [58], the simplest fiber shown to efficiently transmit light from one end to the other consists in a cylindrical core of high refractive index (n_1) where the light propagates, surrounded by a cladding of low refractive index (n_2) that confine the light in the core the through total internal reflection phenomenon (TIR). These fibers are called step-index fibers and an example is shown in Fig. 3.1. Most of the optical fibers are made of fused silica (SiO_2) ,. The difference in refractive index between the core and the cladding is crucial to provide TIR and is often very small: $(n_1 - n_2)/n_1 \ll 1$. The TIR condition is computed through the Snell's law of refraction that predicts a total reflection of light at an interface between two materials of refractive index n_1 and n_2 (with $n_1 > n_2$) , for incident angles $\alpha > \alpha_{\min} = \sin^{-1}(n_2/n_1)$ (see Fig. 3.1). For this angular range the TIR is occuring and light can propagate in the core of the fiber all along the fiber through multiple reflections. Therefore, there is a cone of light at the entrance of the fiber for which the incident angles on the interface core/cladding are higher than $\alpha_{\max}$, and for which the light is transmitted. Outside of this cone, the light can not be confined in the core and escapes through refraction in the cladding. This cone of light defines the numerical aperture of the optical fiber. By applying Snell's law to the end of the fiber, the numerical aperture NA can be written [58]:

$$\mathrm{NA} = n \sin\left(\frac{\pi}{2} - \alpha_{\min}\right) = \sqrt{(n_1^2 - n_2^2)} \tag{3.1}$$

where n is the refractive index of the outer medium. One could assume that any ray entering the fiber within the cone defined by NA can be transmitted, however, when interference effects are taken into account, it becomes clear that only a discrete set of rays are allowed to propagate in the fiber. Only the set of rays that fulfill the conditions for constructive interference can survive the propagation. This is illustrated in Fig. 3.2 where each ray corresponds to one mode. The drawback of this kind of fiber is the intermodal dispersion. Indeed, there will be a delay between the exit time of two modes, as the rays follow different optical paths.

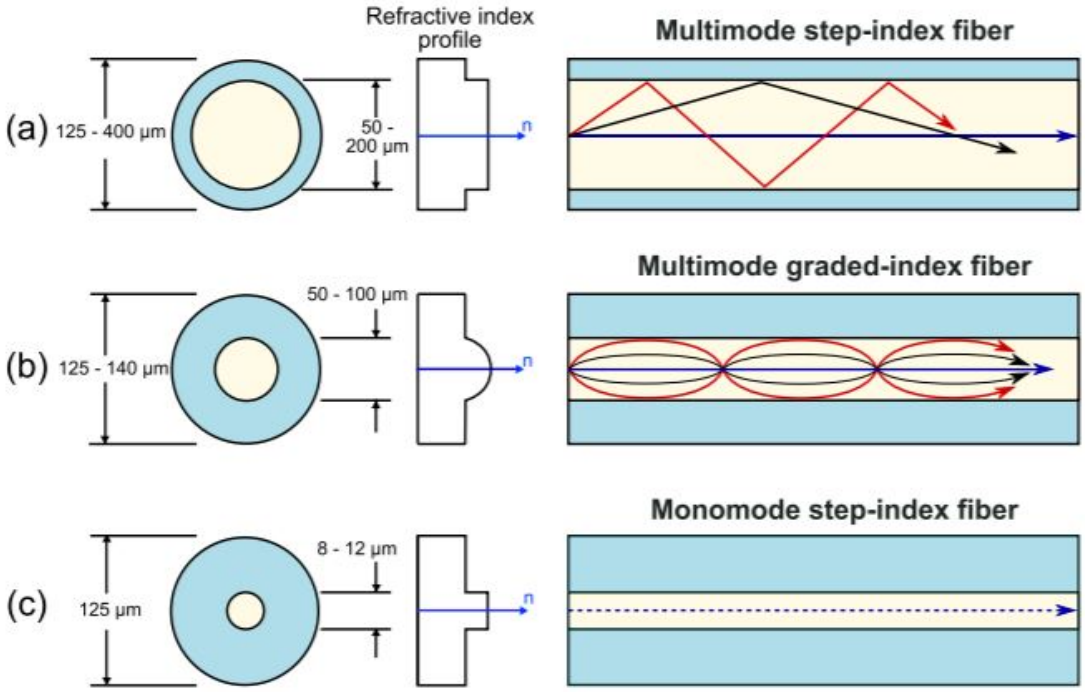

Figure 3.2: Typical dimensions, refractive index profiles, and rays paths in (a) multimode step-index fiber, (b) multimode graded-index fiber and (c) monomode step-index fiber. Figure extracted from [59].

In graded-index fiber, the refractive index gradually decreases from the central axis to the cladding and the NA varies as a function of the radial distance. It is maximum at the center and decreases when the rays enter closer to the cladding. This results in less modes sustained by the fiber and less transmitted light compared to a step-index fiber. In the experimental part of this project we will mainly use step index single (mono) mode fiber.

3.1.2 Mode theory of cylindrical waveguides

If the diameter of the core is very small, or even less than the wavelength of the radiation propagated inside, the geometric approach of the problem through a ray optics approach is not used. In this case, it is necessary to solve Maxwell's equations to find the solutions to the propagation equation that satisfies the boundary conditions. Following the analysis shown in [58], we will present briefly the results of the mode theory for circular waveguides, for a detailed derivation of the results, please see [65]. We are interested in the propagation of the light along the main axis of the fiber, we say z, so an important parameter is the propagation constant β, which is the axial component of the wavevector $\vec{k}(|\vec{k}| = k = 2\pi/\lambda)$.

There are different types of modes that can be sustained by the fiber. First, the **guided modes** are the ones that were discussed above. They are confined in the core of the fiber and differ from each other by the electric field pattern along the fiber's cross-section. The **cladding modes** originate from the light outside of the acceptance angle that is thus refracted and trapped in the cladding. The **leaky modes**, instead, are partially confined to the core region but are attenuated as they propagate. The difference between guided and leaky modes is set by the cutoff condition. A mode remains guided if

$$n_2 k < \beta < n_1 k \tag{3.2}$$

the lower boundary being the cutoff condition. If $\beta < n_2 k$, the mode is leaky. In the geometrical approach, this is equivalent to the TIR limit. As β is the projection of $n_1\vec{k}$ onto the z axis, its maximum value is $n_1 k$. The maximum angle allowed by TIR satisfies $\sin(\alpha) = n_2/n_1$. The projection of $n_1\vec{k}$ onto the z axis then gives $\beta = n_2 k$ as the minimum value of the propagation constant.

The V parameter, also called normalized frequency, can be introduced as:

$$V = \frac{2\pi a}{\lambda}\mathrm{NA} = \frac{2\pi a}{\lambda}\sqrt{(n_1^2 - n_2^2)} \tag{3.3}$$

where a is the radius of the core. Except for the fundamental mode, all modes are cut off when $\beta = n_2 k$, which happens at different values of V depending on the modes. For $V < 2.405$, only the fundamental mode is left, then the fiber is monomode. The number of modes M in a multimode fiber can be estimated by:

$$M \approx \frac{V^2}{2} \tag{3.4}$$

This is the equivalent of the quantization of modes due to interferences in classical picture. The number of modes (of angles in the ray optics interpretation) is limited, then if the core becomes smaller, the number of modes decreases until only the fundamental mode at $\alpha = \pi/2$ is left.

3.2 Optical nanofibers

We already explained in the introduction chapter that in this project we worked with single mode nano fiber to optimize the coupling with the localized defect-bound excitons in the hBN

encapsulated WSe_2 TMDs. It could be then important to analyze briefly the properties of nanofibers that vary from the properties of the common optical fiber; we will do this retracing the work of Garcia et al. presented in [20]. In contrast with the fibers presented in the previous part, optical nanofibers with a diameter smaller than the wavelength of the guided light exhibit a strong lateral confinement of the guided mode in conjunction with a pronounced evanescent field surrounding the fiber [20]. These properties make optical nanofibers a unique tool for efficient and controlled coupling of light with matter on or near their surface, exactly what we want to reproduce in this project. We will present the experimental preparation procedure for the tapering of an optical fiber (TOF) in Chapter 5 as well as the results of the evanescent coupling with the emitter. Thus the properties of the guided light in the nanofibers will be presented, following the treatment developed in [20].

3.2.1 Properties of the guided light in nanofibers

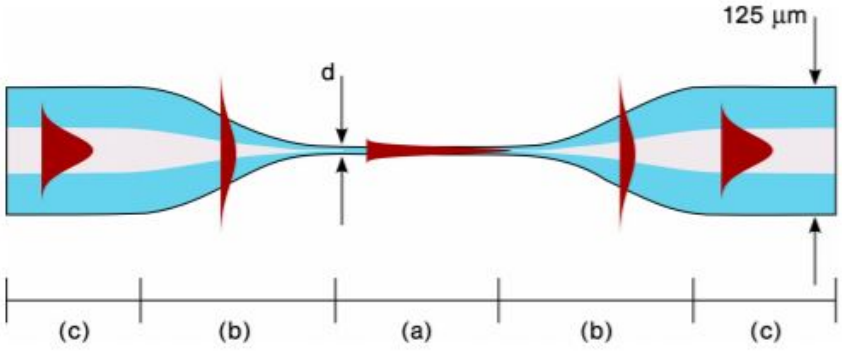

Figure 3.3: Schematic of a tapered optical fiber (TOF) showing the light propagation and conversion of the fundamental mode (c) in the tapered region (b) to the nanofiber waist (a) and back again to the initial mode (c). The intensity profile of the guided mode is schematically represented by the red filled curves. Figure extracted from [20]

Figure 3.3 depicts schematically a TOF. There aree three sections, each of them exhibits different propagation properties: the nanofiber waist (a) surrounded by the two taper transitions (b) and the original unstretched fiber (c). The intensity distribution of the corresponding guided mode is schematically represented by the red filled curves. In the unstretched part of the single mode TOF (part (c)), the light is guided inside the core via total internal reflection at the core-cladding boundary, as explained in the previous section. Due to the low refractive index difference between core and cladding (n_{core} /n_{cladding} ≈ 1.0035) , this section is often designated as weakly guiding and Maxwell's equations are approximately solved by linearly polarized (LP) modes. Then, in the taper transition, both cladding and core shrink. The decrease of the core diameter leads to a compression of the guided mode until the mode diameter reaches a minimum [20]. Further reduction of the core diameter leads to an expansion of the mode into the cladding. Since, in this configuration the cladding acts as the new guiding medium, in order to minimize transmission losses, this mode conversion should be adiabatic, i.e., there should be no coupling of the fundamental mode to higher transverse or radiative modes. This could be achieved by maintaining very small taper angles, in the order of magnitude of a few milliradians [20]. In the experimental section of this project we will show how we tried to control the shape of the tapered fiber produced.

If the fiber diameter is further decreased to the waist value the mode will be more and more laterally confined, as shown in Fig. 3.3. The high refractive index difference at the cladding-air

interface (n_{cladding} /n_{air} ≈ 1.5) provides a much tighter radial confinement. The most important property of this fiber is that throughout the nanofiber waist, the diameter of the fiber remains constant in the sub-wavelength regime, and the guided mode exhibits tight radial confinement and a strong evanescent field, thus, this will be the section of the fiber we will use to get the evanescent coupling with the emitters. At the second taper transition, the mode transformation is reversed. Note, that through this process the weakly guided LP_{01} mode of the unstretched fiber is adiabatically transformed into the strongly guided HE_{11} mode of the nanofiber and back. The intensity distribution of a circularly or unpolarized HE_{11} mode is plotted in Fig. 3.4 as a function of the distance from the fiber center.As depicted in Fig. 3.4 Garcia et al. in [20] observed that the intensity is maximal at the fiber center and decreases towards the surface. Due to the high refractive index mismatch at the surface, the radial component of the electric field exhibits a correspondingly strong discontinuity, while the tangential components of the electric field remain continuous. The transformation of modes defines the hybrid modes that will be used by the MATLAB simulations that will be developed in Chapter 5. We can observe the slow spatial decay length of the evanescent field. The strong intensity achieved at the fiber surface provides excellent conditions for the evanescent coupling we prepare. Light propagation in a nanofiber is usually described using the concept of an effective refractive index $n_{\text{eff}} = c/v_{\text{phase}} = \beta/k_0$, where c is the vacuum speed of light v_{phase} is the phase velocity of the mode, β is the mode propagation constant, and $k_0 = 2\pi/\lambda$ is the vacuum wavenumber.

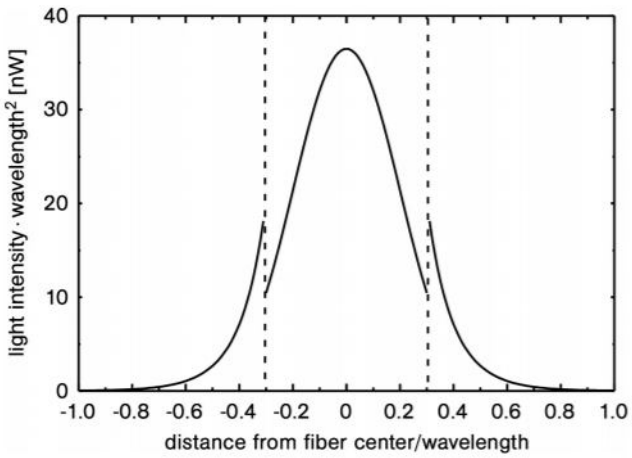

Figure 3.4: Radial intensity distribution in units of $1/\lambda^2$ of the fundamental mode HE_{11} guided through a nanofiber as a function of the distance from the fiber center in units of the wavelength. The calculation are developed for circularly or unpolarized light, a guided power of 10nW, $d/\lambda = 0.6$ and a refractive index $n = 1.46$. Figure extracted from [20]

Fig. 3.5 shows the effective refractive indices of the lowest nanofiber modes as a function of the fiber diameter normalized for the propagating beam wavelenght. Thus, we see clearly the link between the value of the effective refractive index and the guided mode. We will use this tool to understand the mode propagating in the COMSOL simulated fibers. Single-mode and multi-mode regime can be clearly distinguished in the figure. The cutoff value at which only the fundamental HE_{11} mode propagates is wavelength-dependent and corresponds to $d/\lambda \approx 0.73$ for a refractive index of $n_{\text{silica}} = 1.45$. As the fiber diameter decreases, a larger and larger fraction of the mode propagates outside of the glass, and the effective refractive index of the mode decreases to unity. On the other hand, a fiber diameter increase leads to a mode guided mostly entirely in the bulk and the effective refractive index approaches n_{silica} .

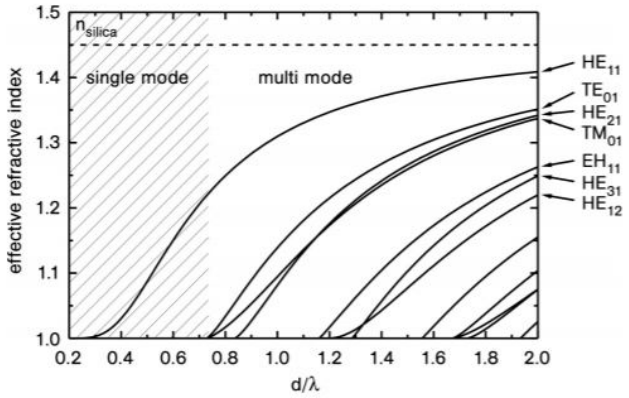

Figure 3.5: Effective refractive index for the fundamental mode (leftmost) and a few higher order modes as a function of the fiber diameter in units of wavelength. The calculation was performed assuming a refractive index of $n_{\text{silica}} = 1.45$. Figure extracted from [20]

3.2.2 Coupling of a point-like source and guided modes

Here, we describe the results by Fieldings et al. [18] of a numerical and experimental investigation of how a point source of radiation couples light to the HE_{11} fundamental mode of a tapered single-mode fiber, that will constitute our experimental objective for the evanescent coupling in Chapter 5. Although light is coupled to fiber cladding modes, energy in these modes eventually leaks out of the fiber and does not reach a detection system. Indeed, the detector receives only light that has traveled back in the core of the fiber, so the optical signal measured at the detector has only two possible origins: 1) direct evanescent coupling to the HE_{11} mode of the fiber or 2) evanescent coupling to fiber cladding modes followed by mode-coupling to the HE_{11} mode.

Taper to taper coupling measurements

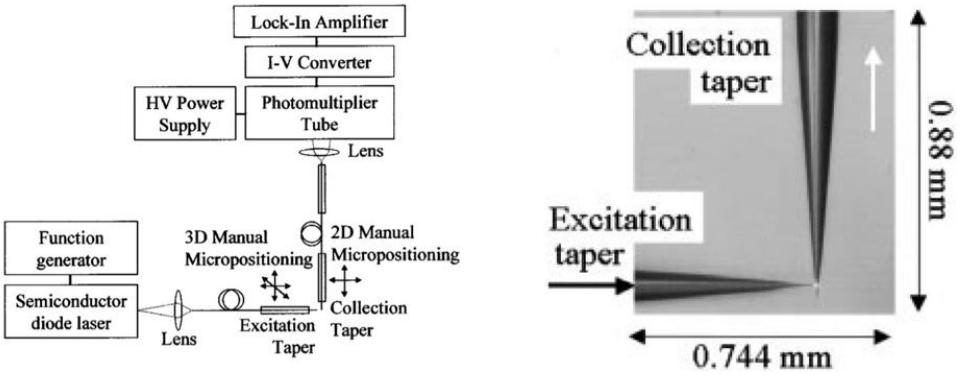

Figure 3.6: Left: Experimental configuration used to measure taper-to-taper coupling. Right: Camera picture of evanescent coupling measurement for a short nonadiabatic tapered collection fiber. Figure extracted from [18]

The measurement of the evanescent coupling of a spatially localized optical source to a tapered optical fiber was achieved by Fielding et al. using the experimental arrangement shown in Fig. 3.6. The setup uses a short, nonadiabatic, tapered optical fiber to approximate a point source of light. The source fiber carries light from a 40mW 785 nm semiconductor laser diode to the surface of a second tapered optical fiber, this wavelenght is very close to the emitted

wavelenght in our WSe_2 samples (from 735-800 nm). This second tapered fiber serves as a "collection taper," its other end illuminates a photomultiplier tube (PMT). Light coupled from the source taper to the collection taper is measured using the PMT. For all the setup specifics, please see [18]. Taper-to-taper coupling was measured with both fibers surrounded by air. The source and collection tapered fibers were each mounted in fiber chuck holders connected to micro-positioners, see Fig 3.7.

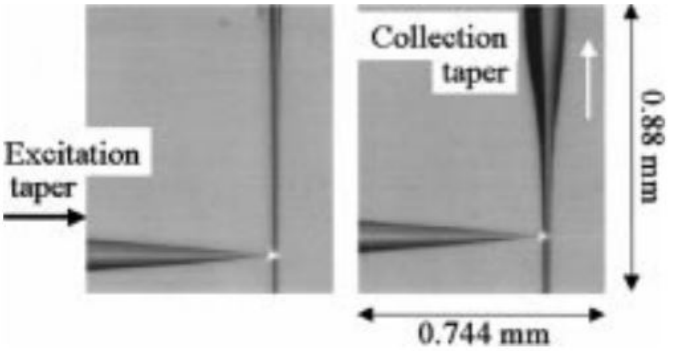

Figure 3.7: Camera picture of evanescent coupling measurement for a long nonadiabatic tapered collection fiber. Two views are shown for the source taper located at different points along the long collection taper. Figure extracted from [18]

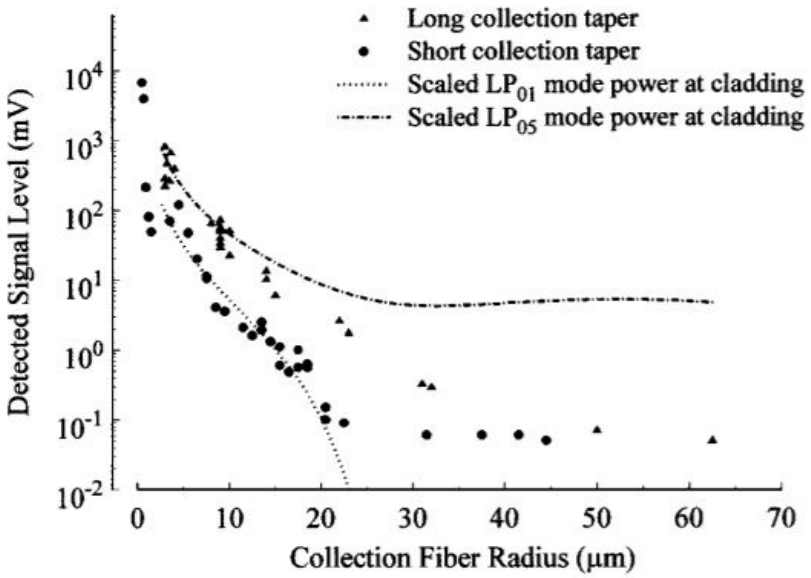

Figure 3.8: Evanescent coupling level measured using two different collection taper shapes. Solid triangles are measured with the source taper in contact with the long collection taper. Solid circles are measured with the source taper in contact with the short collection taper. Figure extracted from [18]

To acquire coupling data, the source taper was moved by manual control of the micropositioner to different locations along the collection taper surface. Evanescent coupling was measured using two different collection fiber shapes. Both a long nonadiabatic tapered optical fiber and a short nonadiabatic tapered optical fiber were used as collection tapers. Fig. 3.8 presents signal levels measured using the two collection tapers. These data show that the long tapers have greater evanescent coupling efficiency than the short nonadiabatic tapers. Coupling efficiency is defined as the fraction of power leaving the source tapered fiber tip, coupled into

the core of the collection taper, and returned to the measurement system. The peak measured signal level in Fig. 3.8 corresponds to a maximum coupling efficiency of 30% in the short taper (with the source taper located at the collection fiber tip) and maximum coupling efficiency of 3% in the long nonadiabatic taper (with the source taper located at a 10μm collection taper diameter). For all taper diameters greater than 10μm, the long taper demonstrated a $5-10$ times greater coupling efficiency than the short taper. The group of Garcia claimed in [20] that the greater measured coupling efficiency of the long collection taper in Fig. 3.8 can be explained in terms of mode conversion inside the taper structure. For this reason, two different LP mode field strengths are plotted in Fig. 3.8. When a source is located at the cladding surface of the collection taper, light couples predominantly to higher order modes in that collection fiber. As the light in these higher order modes travels back along the taper in the direction of increasing diameter, light is coupled to the lowest order core mode by mode coupling.

3.2.3 Conclusions

Fielding et al. [18] have shown that the largest signal arises from the narrowest section of the collection taper and also that a longer tapered fiber demonstrates higher evanescent coupling efficiency than a shorter tapered fiber. We considered this work supported by the COMSOL and MATLAB simulations for the preparation of the tapered nanofibers in Chapter 5. We will see in that chapter how we succeeded preparing a tapered nanofiber with a tip diameter of $0.6\mu m$.

Part II

Experimental Part: setups and results

Chapter 4

Sample fabrication and experimental setups

After treating the theory useful for understanding the experimental project, this chapter opens Part II. The experimental work carried out during the project is described in this part. In particular, this chapter will deal in detail with the preparation process of WSe_2 monolayers. The results of the preparation process carried out in the cleanroom will be presented in the next chapter. Then, the experimental techniques used for the optical characterization of the samples will be presented.

4.1 Sample preparation techniques

As pointed out in Chapter 1, transition metal dichalcogenides (TMDs) are layered materials. Each atomic monolayer has strong covalent bounds in the plane while its cohesion with the other monolayers is ensured by weak Van der Waals forces. The most important advantage of producing monolayers is that when TMDs reach the limit of a single monolayer, their band gap becomes direct an thus optically active allowing several perspective applications [9]. This section focuses on the experimental techniques implemented for a pure sample fabrication. There are several ways to isolate the monolayers and the basic one requires just the sample in its bulk form, an adhesive tape and a substrate. This simple process is called mechanical exfoliation and it is explained in the following paragraph. This is the technique used for the first test of the basic optical properties of WSe_2 monolayers. Although its experimental simplicity, the crucial disadvantage of the exfoliation process is that the position of the layer transferred on the substrate can not be controlled. Thus, deterministic transfer techniques have been developed and we will present the one we used in the following paragraph. These methods enable the layers transfer on a precise position on the substrate and made also possible to stack layers of different materials to form Van der Waals heterostructures through layer by layer deposition.

4.1.1 Mechanical exfoliation

In a typical mechanical exfoliation process, Fig. 4.1, appropriate thin TMD crystals are first peeled off from their bulk crystals by using adhesive Scotch tape. These freshly cleaved thin crystals on Scotch tape are brought into contact with a target substrate and rubbed by using tools such as plastic tweezers to further cleave them. After the Scotch tape is removed, monolayer and multilayer TMD nanosheets are left on the substrate [37].

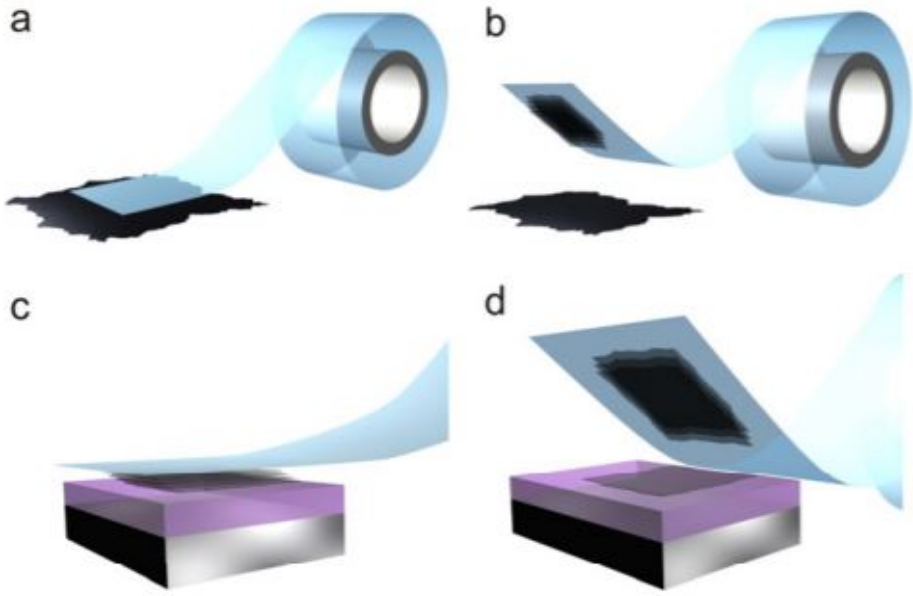

Figure 4.1: Micromechanical exfoliation of 2D crystals. (a) Adhesive tape is pressed against a 2D crystal so that the top few layers are attached to the tape (b). (c) The tape with crystals of layered material is pressed against a surface of choice. (d) Upon peeling off, the bottom layer is left on the substrate. [37]

When the process is over, the final result will be as presented in Fig. 4.2.

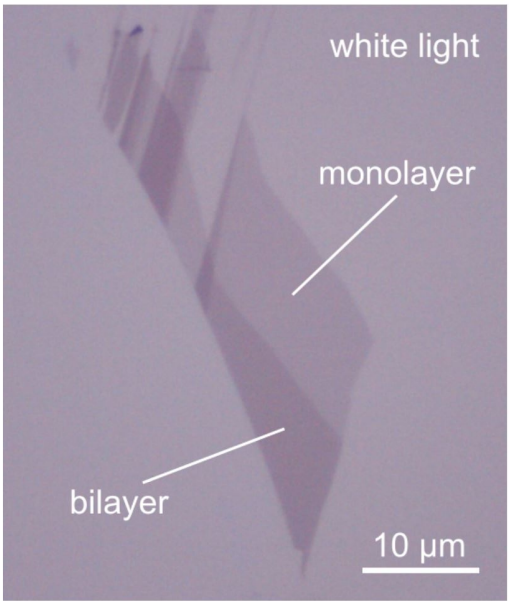

Figure 4.2: Optical microscope image of a WSe_2 sample deposed on a Boron-Nitrade substrate after exfoliation. The lightest zone correspond to the monolayer. Figure exctracted from [37].

4.1.2 Deterministic transfer of two-dimensional materials by all-dry viscoelastic stamping

The deterministic transfer of two-dimensional it is fundamental for the fabrication of heterostructures based on artificial stacking of two-dimensional materials. Indeed, we have already seen in the previous section that the basic mechanical exfoliation process can not reach such a goal as the layers are transferred at random locations onto the substrate. The control on

the positioning of two-dimensional crystals would enable their integration in complex devices, which allows the exploration of novel applications and the discovery of new phenomena in layered materials [7]. One possible solution is the all-dry transfer method that relies on viscoelastic stamps. The whole fabrication process is quick, clean and it can be performed with high efficiency. Moreover, this technique is found very advantageous, since it enables to freely suspend these materials as there are no capillary forces involved in the process.

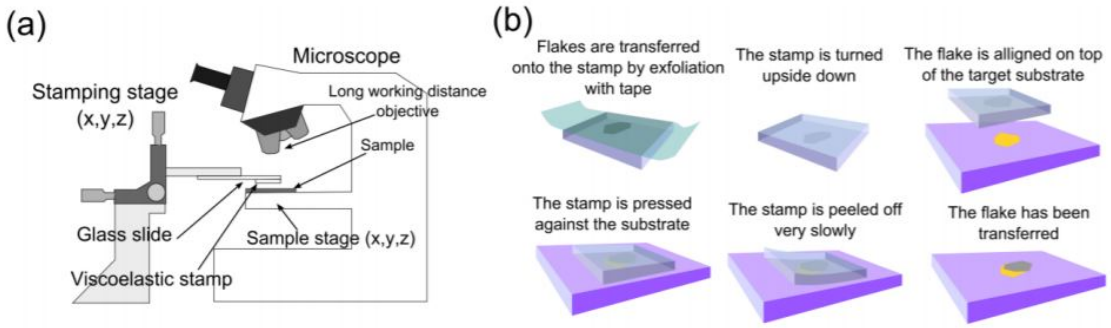

Figure 4.3: Deterministic transfer setup and process. (a) Schematic diagram of the experimental setup for the all-dry transfer process. (b) Diagram of the process for the preparation of the viscoelastic stamp and the deterministic transfer of an atomically thin flake onto desired location. Figure extracted from [7].

The step by step process is shown in Fig. 4.3 (b). The first step is the classical scotch tape exfoliation presented in the previous section. Then, instead of transferring the layers from the scotch directly on a substrate, one has to transfer the exfoliated layers on the viscoelastic polymer stamp, which was polydimethylsiloxane (PDMS) in our case. Now, turning the stamp upside down, it is possible to stick the transparent stamp on a desired location on the substrate and then by removing it slowly the layers are transferred from the stamp to the substrate. The schematic setup is depicted in Fig 4.3 (a) which is composed of two main stages: one for the glass slide and one for the substrate. The glass slide with the PDMS stamp is fixed on a stage which can be moved in the XYZ directions using micromanipulators. The PDMS stamp is scanned with an optical microscope to find the appropriate layers that we want to deposit on the substrate. Once the desired layer has been chosen, we place the substrate below the PDMS stamp on another stage which can also be moved in the XYZ directions. Having these two mobile stages makes it possible to align properly the PDMS stamp with the substrate by alternately focusing on the substrate and on the PDMS. We can thus choose with micrometer precision the location of the layer transfer. Once we are well aligned, we lower the PDMS stamp until we come into contact with the substrate.

4.2 Hexagonal boron nitride encapsulation

It has been shown in the previous section that it is possible to stack layers from different layered materials to obtain a Van der Waals heterostructure. In the following paragraph we will show that a hBN/TMD monolayer/hBN Van der Waals heterostructure provides an improved optical quality compared to the monolayers transferred directly to a SiO_2 substrate, and we will observe that this improvement is strictly link with the suppression of disorder effects [57].

4.2.1 Motivations for encapsulation

Inhomogeneous broadening of TMDs monolayers on SiO_2 and emission unstability

TMDs monolayers have became a hot topic since 2010, in particular TMDs monolayers deposited directly on SiO_2 [43]. Though this preparation technique provided a good insight of the main properties of the materials, a more detailed spectroscopic analysis enlightened broad linewidths due to inhomogeneous broadening [33]. This broadening effect is clear, for istance, in MoS_2 excitonic transitions, where, even at low temperature ($5K$), the linewidth of the peaks reaches up to $50meV$, as we can see from Fig. 4.4.

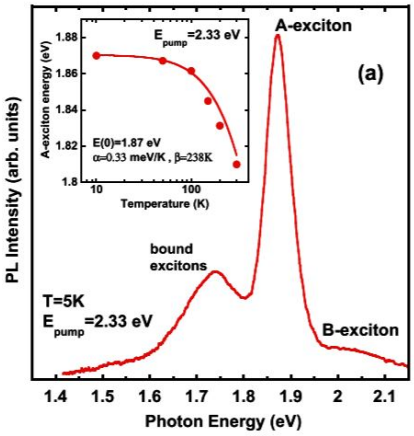

Figure 4.4: PL spectrum at 5K taken with a 532 nm excitation. The PL is dominated by the A-exciton emission and its temperature dependence (upper left inset). Figure exctracted from [29].

The transition linewidth depends on two main contributions, the homogeneous and the inhomogeneous broadening. As described in [48], the homogeneous broadening rate γ is given by:

$$\gamma = \frac{\Gamma}{2} + \gamma^* \tag{4.1}$$

where Γ is the population relaxation rate due to radiative and non radiative recombinations, while γ^* represents the dephasing rate coming from exciton-exciton or exciton-phonons scattering. Moreover, the exciton energy transition can be shifted due to the local potential fluctuations and disorder. The set of all the possible values of the excitonic transition energy values due to these effects will provide broad PL transition lines, as schematized in Fig. 4.5.

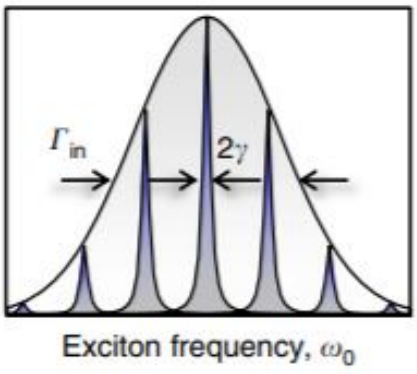

Figure 4.5: An inhomogeneous distribution of exciton oscillator frequencies due to a varying local potential landscape masks the intrinsic homogeneous linewidth in most optical spectroscopy experiments. Figure exctracted from [48].

Thus, the observation of broad transitions in PL experiments suggested that the inhomogeneous broadening effect was dominant. Indeed, Four-Wave mixing experiments and 2D Fourier Transform Spectroscopy confirmed that the large inhomogeneous broadening is a signature of local spatial inhomogeneity [48], which is mainly due to substrate on which the TMD monolayer is deposited, through charge puddles and strains.
Moreover when SiO_2 is used as a substrate, it has been shown that, for a given sample, the energy position for the A-exciton in PL experiments can vary significantly after several cryogenic cycle [33] and in addition an hysteresis shifting effect is measured for transition energies at low temperature when the sample is exposed to different excitation power [6].

4.2.2 The choice of hexagonal boron nitride and encapsulation technique

Hexagonal boron nitride has attracted a great attention in the scientific community because it was shown that using hBN as a new substrate for graphene deposition increased the electronic mobilities three times more than SiO_2 [12]. In fact, hBN provides a high k-dielectric isolating graphene. Moreover, hBN is crystalline and atomically flat compared to amorphous SiO_2 which is rough. These are just two of the main advantages that made the hBN as the most used substrate for TMDs monolayers. Since, even the electrical environment and the molecular absorbption have been proven as perturbation of the optical quality of the TMDs monolayers, hBN has ben used also as a capping layer, to form a $hBN/$ TMD monolayer $/hBN$ Van der Waals heterostructure, in order to protect the TMD from many possible perturbations. A schematic illustration of an hBN-encapsulated samples and their optimized optical PL quality are shown in Fig. 4.6. Thus, in this thesis project we worked always with encapsulated samples.

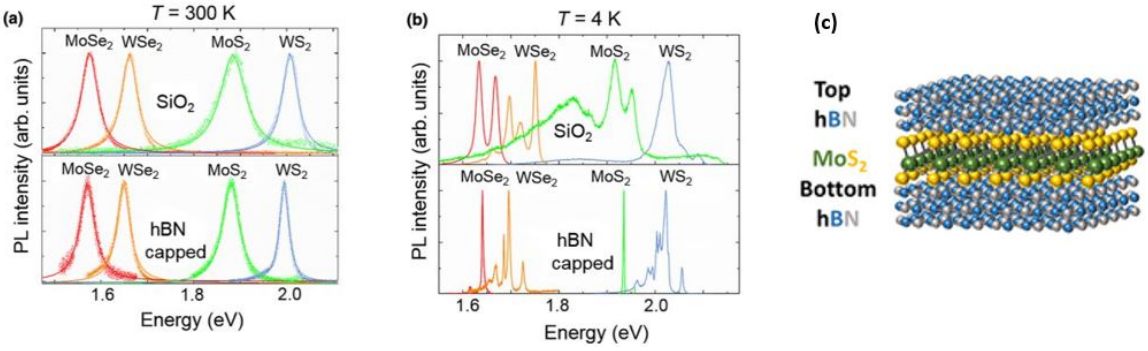

Figure 4.6: (a) Typical PL spectra for different TMDC MLs at T=300 K when deposited directly onto SiO2 (top) and when capped with hBN (bottom). (b) Same as (a) at 4 K. (c) Schematic representation of a TMD hBN encapsulation, here MoS_2 as an example. Figures exctracted from [5].

4.3 Experimental techniques

This section is dedicated to presentation of the main optical setup we used for optical characterization of the sample and for the analysis of the emitted light. We will present the fundamental principles of optical spectroscopy and then analyze the techniques used for micro photoluminescence (μ-PL or micro-PL) experiments and the techniques used for the measurement of the radiative lifetime (T_1) and the second order degree of temporal coherence ($g^{(2)}(\tau)$).

4.3.1 Optical spectroscopy setup

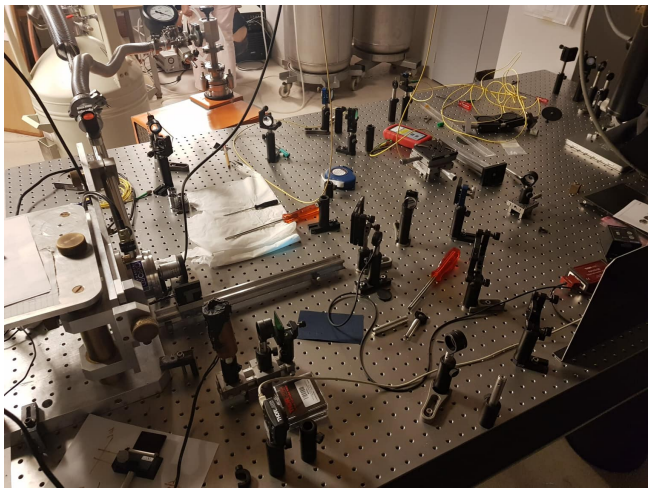

Figure 4.7: A picture of the optical spectroscopy and μ-PL setup I have used.

The fundamental optical study for any kind of experiments starts from the spectral characterization of the signal. The spectrum analysis of the source allows for the first interpretation of the nature of the emitters, for instance the distinction of the transitions (excitonic, bi-excitonic, defect-bound excitonic...), the emission spectrum between different samples as well as the presence of trapped charges through the shifting of the transition lines from the expected wavelength.

An optical spectroscopy setup is basically composed of a light source, the sample to be characterized, a detector and a spectrometer. In our case, the sample is kept under high vacuum and low temperature to reduce thermal fluctuations as the population of optically active carriers is optimized at cryogenic temperature, see Fig. 4.7. For the vacuum we used a turbo molecular pump while for low temperature we used a liquid Helium cryostat, reaching low temperature as 3-4 K. Inside the cryostat the sample is glued to the holder using silver paste ensuring good thermal contact. In our setup one of the main components was the microscope objective. It was mounted on a piezo-electric support giving the possibility to direct the laser beam over a desired position on the sample with a precision up to 0.5 μm in XYZ directions. Moreover it collected the signal from the sample and let it propagate in our optical path eliminating the beam of light coming out of the focal plane using pinholes. It is important to analyze then the specifics of the lens since they will affect the spatial resolution of the setup. Using the Rayleigh criterion it is possible to estimate the beam spot diameter D in the focal plane of the objective as

$$D = 1.22 \times \frac{\lambda}{N.A.} \tag{4.2}$$

where λ is the excitation wavelength (we mainly used a HeNe laser 632.8 nm and Ti-Sa 726nm) and $N.A.$ is the numerical aperture of the objective, given by $N.A. = nsin\theta$, in our case $N.A. = 0.4$. By using the equation 4.2 we can estimate a $D = 1.9 \times 10^{-6}m$ for the HeNe laser and $D = 2.2 \times 10^{-6}m$ for TiS, roughly $2\mu m$. High spatial resolution is important for an optimal optical characterization of TMDs monolayers. In fact, TMDs are generally subject to spatial inhomogenities due to the preparation process and the stage mounting and it is fundamental to have the possibility to scan the TMD monolayer to find the area with the highest optical quality. It is important to remark that we used a low N.A. microscope objective because we want to have enough space to introduce more components inside the cryostat, like the nanofiber and thus we will lose in counts but we will gain in working space. For the analysis

of the light coming out from the sample we used a spectrometer. The spectrometer is coupled to a Charge-Coupled-Device (CCD) cooled down with liquid nitrogen to increase the signal to noise ratio. CCD has a photoactive region constituted by an array of photodiodes which are p-doped metal-oxides semiconductors (MOS) capacitors. When a photon hits one of the pixels of the array it will excite electrons that will be accumulated at the semiconductor-oxide interface of the capacitors. The electric charge generated is proportional to the number of photons (light intensity) impinging on the capacitor. Then, the accumulated charge will be swept by an electric field and transferred to a read-out zone where it will be converted into a digital signal.

The array of our CCD is made of 2000X256 pixels (just the first number is important in spectroscopy mode, the vertical number of pixels can be neglected since the spectroscopy occurs on a linear section of the CCD) which measure 15 $\mu m \times 15 \mu m$ each. Since our CCD has quantum efficiency from 80% to 95% in the 600-900nm wavelengths range then is it sensitive to the emission of the main members of the TMDs family [2]. The first sample monolayer we prepared was around $100 \mu m \times 50 \mu m$, very small compared to the substrate dimensions, $1 cm \times 1 cm$. Thus, an imaging setup was necessary to simultaneously understand how to move the beam and optimize the signal collection. The imaging setup will be shown as a part of the micro photoluminescence setup, thus in the next section.

4.3.2 Micro photoluminescence (micro-PL)

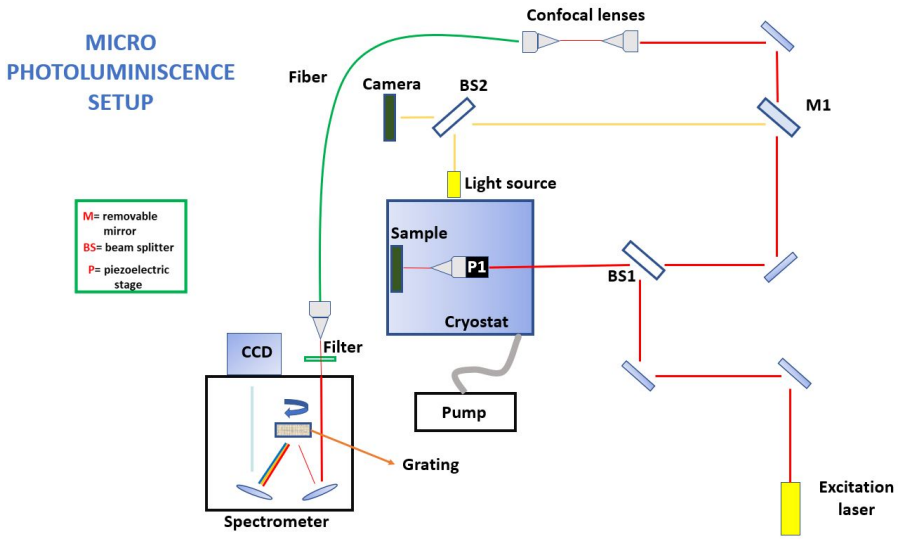

Figure 4.8: The laser beam is directed on the sample through the first two mirrors and the beam splitter (BS1) from which it reaches the objective and then the sample. The signal emitted by the sample follows the reverse path but passes the BS1 and is directed towards the confocal lens system passing the M1 mirror which is used only in imaging mode. Confocal lenses are used to reduce the beam spot and obtain good coupling with the fiber which focuses the signal to the entrance slit of the spectrometer and then analyzed by the CCD.

Photoluminescence is the process of light emission from a semiconductor material when it is excited by photons. Thus to occur, radiative recombination processes are needed, which is verified for TMDs in the monolayer limit. Micro-PL is a sensitive, non-destructive technique useful for the study of semiconductors optoelectronic properties. Photoluminescence emission depends on fast-relaxation processes and it is sensitive to the shortest radiative lifetime and lowest energies transitions. A schematic illustration of a typical micro-PL setup is shown in

Fig. 4.8. Firstly, the sample is exposed to an excitation light beam (laser) whom photons will create electron-hole pairs in the sample. Naturally the light beam wavelength need to be chosen properly to be greater than the bandgap of the material. We observed that using red-laser with wavelength just below the excitonic spectral line, so almost in "resonance", we obtained cleaner and more intense transitions than with the green one, we will see it in detail in the next chapter of the thesis in which we will analyze the excitation wavelength dependence of the transition lines through photoluminescence excitation spectroscopy experiment (PLE). In fact, an advantage of PL is that it enables the observation of optical transitions with small oscillator strength [71], thus as exciton bound to defect or impurities and charged exciton (trions) transitions. Indeed, we will see in the next chapter that the presence of defects introduces the existence of energy levels in the gap and so transitions with energies lower than the band gap. PL is also an useful tool to test the cleanliness of the sample and compare it with the new ones. In the cleaner sample (sample 2) the peaks will be sharper and more intense, as we will see in the next chapter through the comparison between the first sample (sample 1) and the second one (sample 2) prepared. An important optical element for a photoluminescence experiment is the optical filter, that we used to prevent the laser light from passing into the spectrometer. Indeed the laser light can perturb the measurements, particularly if it is "in-resonance" with the energy of the optical transition since we can not easily distinguish the pure signal from the sample from the one of the laser. As we said before, an imaging setup was necessary to simultaneously understand how to move the beam and optimize the signal collection. Thus, as shown in Fig. 4.8, we used a white lamp source that emits light which is collimated and sent to the beam splitter (BS2) which makes white light to be reflected onto a flip mirror (M1) which will be flipped during acquisition. From M1 the light is then reflected through BS1 to the cryostat on the sample. The light is back reflected by the sample and follows the reverse path and when it reaches BS2 it is transmitted to the imaging camera. It is important to note that we worked with a not perfectly collimated beam on purpose since we want an image of the sample larger than just the spot diameter of the laser beam.

4.3.3 Radiative lifetime measurements: model and set-up

The radiative lifetime of an excited state is the lifetime of the state under the assumption that only radiative processes depopulate that level. In general there can be several non radiative processes, like phonon coupling, that can affect the theoretical expected value. We will briefly explain a model proposed by Ayari et al. [2] to predict the radiative lifetime of localized excitons in TMDs and then present the experimental set-up we used measure it.

Model: Radiative lifetime of localized excitons in transition-metal dichalcogenides

The model developed by Ayari et al. [2] describes the localization of the excitons, due to lattice structural defects, residual impurities introduced during exfoliation, via a random disorder potential. They show that it can be described by a Gaussian random field for electrons and holes $V_{e,(h)}\left(\rho_{e,(h)}\right)$, created from a superposition of N random plane waves with random direction θ_i, random phase ϕ_i, and a wavelength L, which will be shown to correspond to the disorder potential correlation length. Thus the final form of the potential is:

$$V_{e,(h)}\left(\rho_{e,(h)}\right) = \frac{V_{0;e,(h)}}{\sqrt{2N}} \sum_{i=1}^{N} \mathrm{Re}\left\{ e^{i\left(\boldsymbol{K}_i \cdot \boldsymbol{\rho}_{e,(\boldsymbol{h})} + \phi_i\right)} \right\} \tag{4.3}$$

with $\boldsymbol{K}_i = \left(\frac{2\pi}{L}\cos\theta_i, \frac{2\pi}{L}\sin\theta_i\right)$, $\boldsymbol{\rho}_e$ and $\boldsymbol{\rho}_h$ are the in-plane position vectors for the electron and the hole, respectively, $V_{0;e,(h)}$ is the fluctuation amplitude for the electrons and holes,

respectively. Under the assumptions of low temperature, low doping density, and under low-density excitation the model does not capture optical transitions that are associated with trions and their fine structure, biexcitons, excitons (shortwave) plasmon coupling, as well as phonon emission while it is focused on bright exciton states. It aims at the analysis of the impact of the disorder potential originating from defects on exciton states and radiative lifetime. The model is developed in three steps. First the calculation of the eigenstates and eigenvalues of a localized exciton by solving the effective Schrödinger equation where the disorder potential model is inserted. Second, the treatment of the influence of the disorder parameters on the optical properties. Third, by using the Fermi golden rule, the calculation of the radiative lifetime of the localized excitons. The model proves that the localized excitons have a longer emission time than free excitons and that the decay time depends strongly on the disorder model parameters and the dielectric environment. Indeed, we will measure nanoseconds long lifetimes for the localized excitons, way longer thant the picoseconds lifetimes measured in literature for the free excitons [68]. The full treatment is out of our aim, for a detailed analysis see [2].

Setup

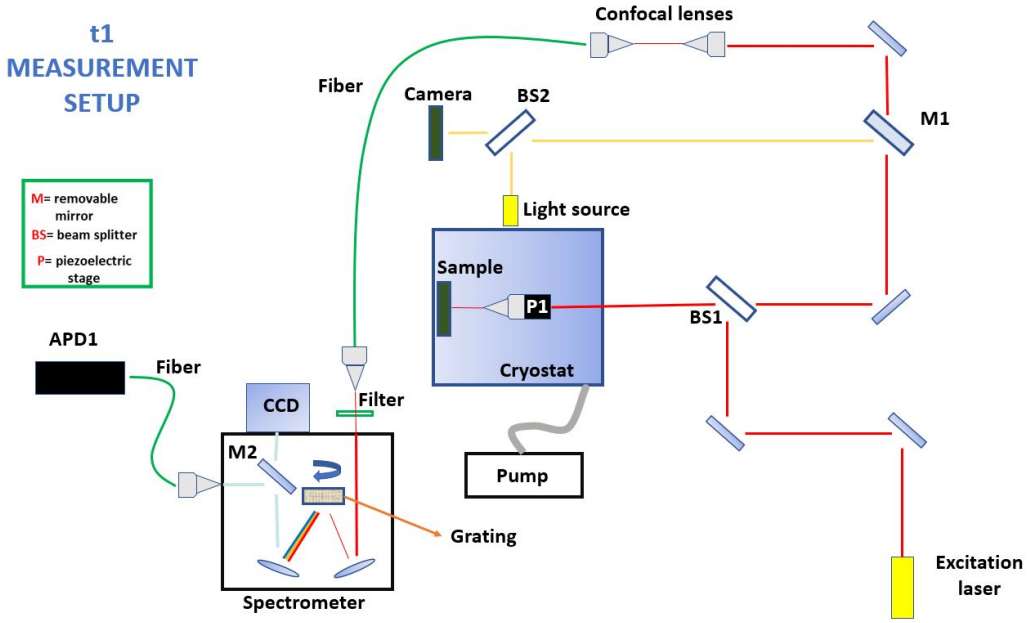

Figure 4.9: The setup for the T_1 measurement is the same as that used for the micro-PL with the only difference that the M2 mirror is raised to bring the signal to the APD via the fiber and preventing the signal from reaching the CCD. The generation of the histogram is carried out by a time-correlator connected to the APD.

The experimental setup for the radiative lifetime of the emitters is shown in Fig 4.9. Firstly, one needs to choose the peak to analyse. We decided to choose the best peak found after an optical PL scanning of the flake. For "best" we mean the most intense, to have the highest signal to noise ratio, the sharpest and well spectral isolated peak in order to avoid peak selection confusion due to the resolution limits of the spectrometer. The experimental setup is basically the same of the one described in the previous section with the addition of an Avalanche Photodiode (APD) and the use of a pulsed laser. In our case, we used a mode-locked picoseconds pulsed (80MHz) Titanium-sapphire laser, with tunable wavelength. From the practical point of view a radiative lifetime measurement (T_1 measurement) is the experimental generation of an histogram. We want to reproduce the counts distribution of the time delay between the

laser pulse and the emitted photon detected by the APD. The distribution is exponential decaying and plotting it in natural logarithmic scale and extracting the inverse of the slope of the linear fit we obtain the radiative lifetime. Thus, we introduced in the experimental apparatus a fiber-coupled LabView programmed Avalanche PhotoDiode (APD). An avalanche photodiode is a semiconductor-based photodetector (photodiode) which is operated with an additional semiconductor layer and a relatively high reverse voltage (typically tens or even hundreds of volts), sometimes just below breakdown. In this regime, carriers (electrons and holes) excited by absorbed photons are strongly accelerated in the strong internal electric field, so that they can generate secondary carriers. The avalanche process effectively amplifies the photocurrent [14] and thus the signal. The APD was fiber coupled to the exit slit of the spectrometer in order to have the possibility to select the peak we want to study by rotating the internal grating of the spectrometer.

4.3.4 Labview coding

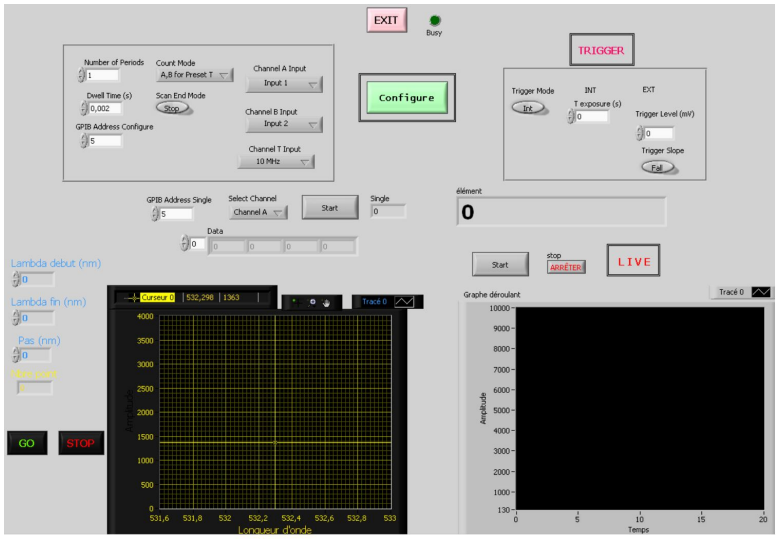

Figure 4.10: The front panel of the labview code we prepared to record the same spectra detected with CCD with the APD. The left half controls the single mode counting while the right one controls the live mode counting.

The LabVIEW coding, was a fundamental part of the instrumental apparatus setup for T_1 measurements, as well as the $g^{(2)}(\tau)$. Indeed, it enabled instruments to communicate between themselves allowing the user to produce more complex measurements than the ones which require just a linear-logic experimental process. In our case, it enabled the communication between the CCD (spectrometer) and the APD providing the experimental conditions to perform the radiative lifetime measurements. The code was made to have the possibility to reproduce the spectra collected with the CCD with the APD, and thus enabling the selection of the desired peak and the creation of the counts histogram for that specific peak. Since the CCD is composed by an array of photodiodes it can collect a large spectral range (60nm), each collection while the APD just measure the intensity of the collected signal. Thus, in order to produce a spectrum with the APD, we needed to be able to control the wavelengths hitting it. As explained before, we could select and control the wavelength by twisting the grating inside the spectrometer, the control of which was managed by our LabVIEW code. Indeed the communication between the spectrometer, CCD and APD was fundamental. We needed to start the counting on the APD signal just when the spectrometer arrived in the right wavelength position. We could collect both when the spectrometer was moving (to obtain a spectrum)

both with a fixed wavelength (when the peak was selected and optimized for the lifetime measurement). The front panel of the code is shown in Fig. 4.10. The bottom-left part of the panel controlled the spectrum acquisition part. With the light blue controls we could communicate the initial and final wavelengths to the spectrometer. The bottom-right part, instead, managed the live counting mode, i.e. the live reading of the counts collected by the APD. This tool was crucial to optimize the signal. Indeed the APD was fiber-coupled to the PL signal emerging from the sample, that before reaching the APD, it had to follow an optical path composed by beam splitters, mirrors lens and spectrometer. Thus the optimal alignment of the optical setup was required to optimize the counts and through the live counting mode of this setup it was way easier since we just need to check whether the counts increased or decreased. The top-left part was used just to control the input signal of the APD while the right-top part controlled the integration time of the measurements. In summary, this coding was necessary to enable us to perform the radiative lifetime measurements. The results will be presented in the next chapter.

4.3.5 The $g^{(2)}(\tau)$ setup

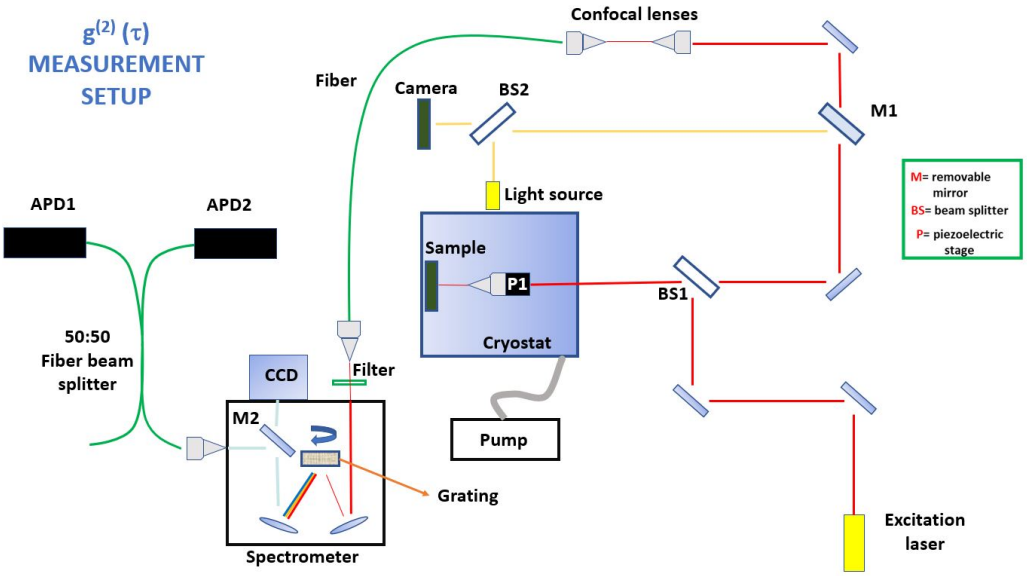

Figure 4.11: The setup for the $g^{(2)}(\tau)$ measurement is the same as that used for the T_1 with the only difference that now the exit slit of the spectrometer is coupled to a 50:50 fiber beam splitter to bring the signal to the APDs, that are, of course, two this time.

From our perspective the second-degree temporal coherence is the measure of the single photon source nature of the material, the lowest the value at zero delay time the most close to a single photon source it is the emitter. The setup for a $g^{(2)}(\tau)$ measurement is basically the same of a T_1 measurement but with an additional APD connected to the exit slit of the spectrometer through a 50:50 fiber beam splitter as depicted in Fig. 4.11. From the practical point of view a $g^{(2)}(\tau)$ measurement is another histogram. This time each count is the time delay value between the counts of each APD, one referred as the "start" and the other as the "stop". So, for a single photon source, we expect to have histograms with v-shape centred (lowest value) in 0 for a continuous wave laser excitation and a histogram with peaks centred on the integer multiples of the laser pulses delay (12ns in our case) and no peaks for 0 delay. We exploited our T_1 setup for the $g^{(2)}(\tau)$ measurements. Indeed, since we already optimized the coupling efficiency with the first APD we just substituted the fiber coupled to the spectrometer APD

with a fiber 50:50 beam splitter and bring the two output arms to the two APDs. We could do the same experiment by using an optical 50:50 beam splitter to split the beam but the apparatus would have been more heavy and sensitive to mechanical misalignment. To obtain a clear curve for the $g^{(2)}(\tau)$ one would need an intense peak (10 000 counts/s) to have a high signal to noise ratio or let the experiment run for more than ten hours. However, checking the stability of the apparatus during such a long time is not trivial. Thus, during my thesis we had to postpone this measurement to the second samples produced since the first one was not clean enough to provide such intense lines. An example of a $g^{(2)}(\tau)$ measurement in continuous and pulsed regime for a single photon source is presented in Fig. 4.12. This will be the plot we will use as a comparison for our results.

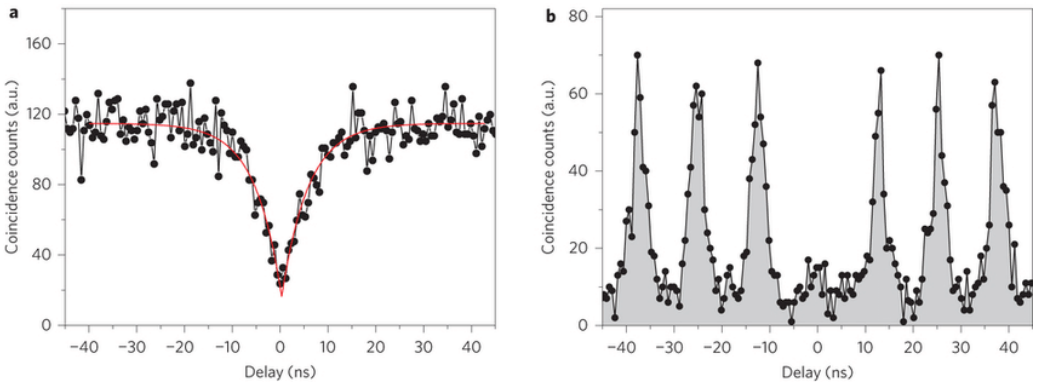

Figure 4.12: An example of a second-degree coherence function for a single photon source for the case of a pulsed excitation (right) and CW excitation (left). Figure extracted from [24].

Chapter 5

Experimental results

In this chapter the main experimental efforts and results will be presented. Finally, after the detailed analysis of the theoretical background of the project and the description of the experimental setups , we can move to the results presentation. The chapter will be developed retracing, basically, the chronological and logical steps we followed during my thesis project to reach the final goal, thus to be able to evanescently couple the emitter radiation into a tapered nanofiber. Of course, we could not go directly to the fiber coupling without having characterized optically our samples.

5.1 Sample preparation and comparison

In this section we will present the experimental process we followed for the production of the samples. The theoretical explanation of these processes has already been addressed previously, the goal of this section is to show the procedure we followed step by step. The preparation part was probably the most delicate of my thesis, since, as we will see, the quality of the samples produced determines their optical response. We will therefore show how we have prepared the monolayers (and bilayers) of WSe_2 encapsulated in hexagonal boron nitride (hBN).

Figure 5.1: In the left picture, a WSe_2 sample in bulk form. In the right one, the first step of the exfoliation process. We can see how some layers of the sample are transferred from one part of the scotch tape to the other. The process need to be repeated until the sample appears slightly violet in contrast to sunlight.

Initially we have the TMD bulk, as seen in Figure 5.1. The monolayer production process starts from the exfoliation of the bulk material. As explained in the previous chapter, the

exfoliation process allows us to overcome the Van der Waals forces that hold the TMD layers together. To do this, we use the Scotch tape made of PDMS and repeat the process for fifteen times. Visually, we knew when to stop by observing the color of the material deposited on the Scotch when exposed to outside light. When the sample began to take on a purplish color, we understood that we could end the exfoliation. The final test consisted in observing the sample under a microscope. Before doing this, it is necessary to transfer the material onto a SiO_2 substrate using the same technique. This allows to obtain a strong contrast under the microscope, without which it would be impossible to observe the exfoliated sample since it would be transparent. The monolayers obtained are then be encapsulated in the hBN which was therefore subjected to the same preparation and then equally transferred to the SiO_2. Once the transfer was completed, the samples were examined under microscope.

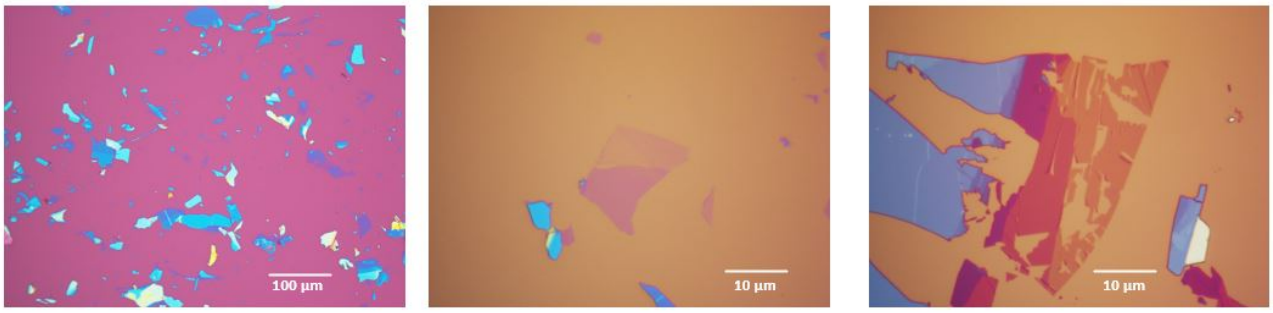

Figure 5.2: Microscope image that highlights how the fragments TMD are evident thanks to the strong contrast with the substrate. The different colors indicate the different thickness of the layers. The light violet color indicates a monolayer, as we see in the image in the center, that represents a monolayer of hBN while the one on the right a monolayer of WSe_2.

In Figure 5.2 we observe the results of exfoliation, seen under the microscope. The left figure shows a wide-field image that highlights how the fragments of WSe_2 are evident to the eye thanks to the strong contrast with the substrate. This applies also to the hBN. The image in the center represents, instead, a monolayer of hBN while the one on the right a monolayer of WSe_2. We can distinguish the thickness of the layers thanks to the variation of the color under the microscope. We observe an almost transparent purple for the monolayers while the color gradually darkens for thicker layers (bi-layer or multi-layer). It is important to observe how the production of hBN monolayers and bilayers is facilitated by its crystalline structure while for WSe_2 the structures were extremely fragile as can be seen from the image on the right in which the monolayer can be seen fragmented but still useful. To assemble a good sample, we sought the largest and most homogeneous monolayers possible in order to have an homogeneous optical signal and facilitate the deterministic transfer for encapsulation in the hBN.

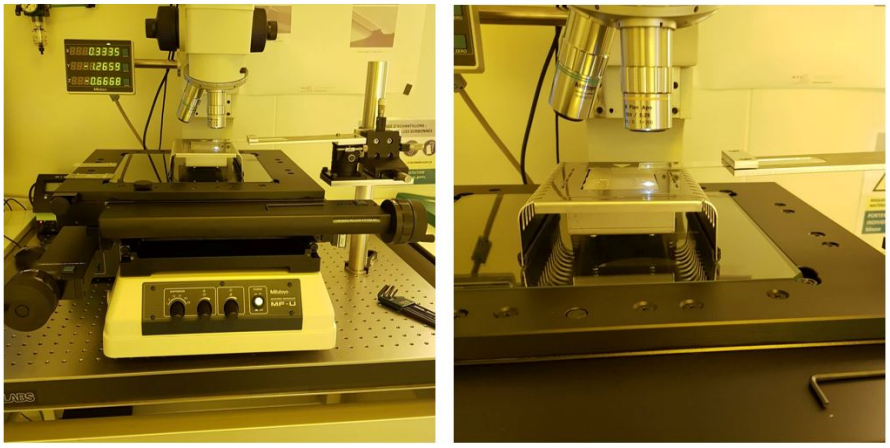

Figure 5.3: Apparatus used for the deterministic transfer process for the transfer of an atomically thin flake onto desired location. The right picture represents a zoom of the PDMS glass stage mounted on a micrometric moving stage, used to pick-up and depose the desired layers in the desired position.

At this point, the substrates on which WSe_2 and hBN had been deposited were transported to the instrument shown in Fig. 5.3 for the deterministic tranfer and encapsulation process. The figure on the right represents a zoom of the stamping stage in which we see the glass slide with the PMDS. The instrument, equipped with a microscope, allowed us to carefully select the monolayers we wanted and position them at the desired position on the final SiO_2 substrate and form, by repeating the process, a $hBN/WSe_2(ML)/hBN$ structure.

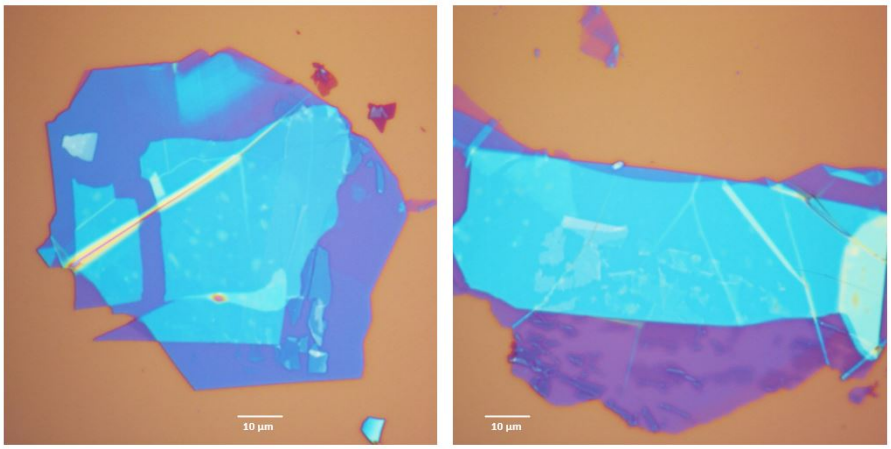

Figure 5.4: An example of two completed samples of $hBN/WSe_2(ML)/hBN$ as they appear under the microscope. The light blue part, therefore thicker, is actually the portion of the sample encapsulated in the hBN.

As reported in Fig. 5.4, we can observe how two samples of $hBN/WSe_2(ML)/hBN$ appear under the microscope when the process is completed. The light blue part, therefore thicker, is actually the portion of the sample encapsulated in the hBN. At this point the sample is carefully transported to the laboratory for optical signal analysis. I had the opportunity to go to the clean room several times and produce more samples, to which we will refer as sample 1 and sample 2. This will allow us to compare the signal of different samples as well as measuring the $g^{(2)}(\tau)$ that in sample 1 was not possible due to the low counts of the emitters.

5.2 Optical characterization of sample 1

In this section we will present the micro-PL experiments data. All the measurements were taken at 4K using liquid helium.

5.2.1 Micro-PL and power dependence measurement

The first analysis we made was the PL scanning of the sample. We tried to map the sample to understand if is there any difference in the PL signal from the monolayer and from the bilayer and then to check the difference within different emitters all over the sample. The results are presented in the following figures.

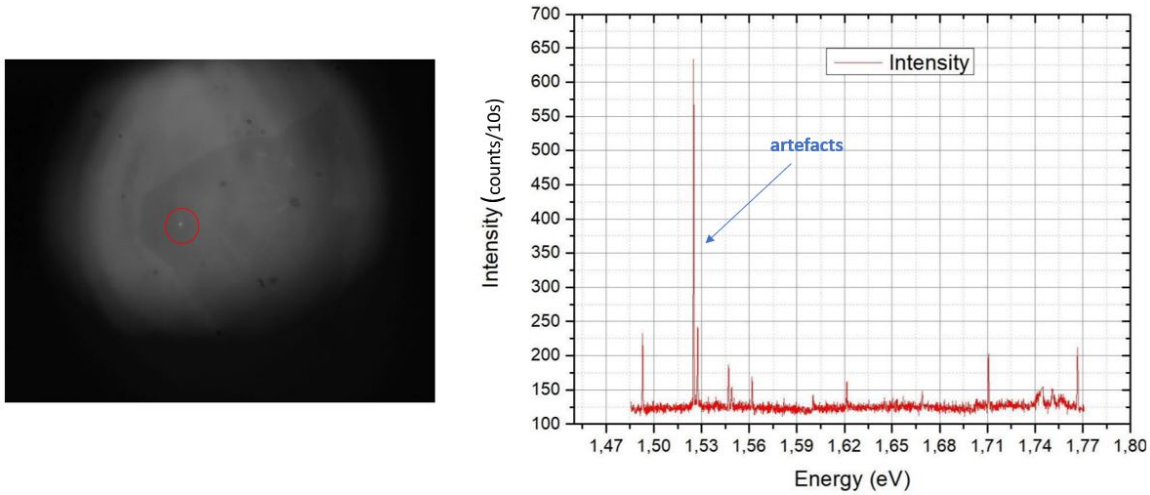

Figure 5.5: (Left) View of the flake from the imaging camera. The white spot is the laser. (Right) PL measurement of the WSe_2 flake in a position outside the monolayer and the bilayer. Indeed there is no significant peaks, since the super sharps ones we see are coming from the laptop screen. The measurement was taken at 4K, with a green laser (HeNe 532.2 nm) excitation at 66nW. The integration time is 10s.

The first measurement was taken from a position outside the bilayer and the monolayer zone and its PL signal is shown in 5.5. We can see some sharp spectral lines that we understood were artifacts. Since the aim of this section is just to qualitatively see the difference between the mono and the bilayer PL signal and since the significant peaks are way more intense than the artefacts and thus easily distinguishable, we decided to not re-take the measurements.In 5.5 we are focusing the laser outside the mono or bilayer active region, thus we see no lines at all. Finally in Fig. 5.6 a first clean signal from the free-excitonic band around 1.65 eV is present. We can observe, also, the trion peak at 1.67 eV. There is also a small increase in signal due to defects bound excitons around 1.53 eV. We can so understand that we are dealing with an emitter laying in a monolayer portion since, as shown in Chapter 1, the excitonic transition lines become intense as the optical band gap becomes direct in the monolayer limit [68].

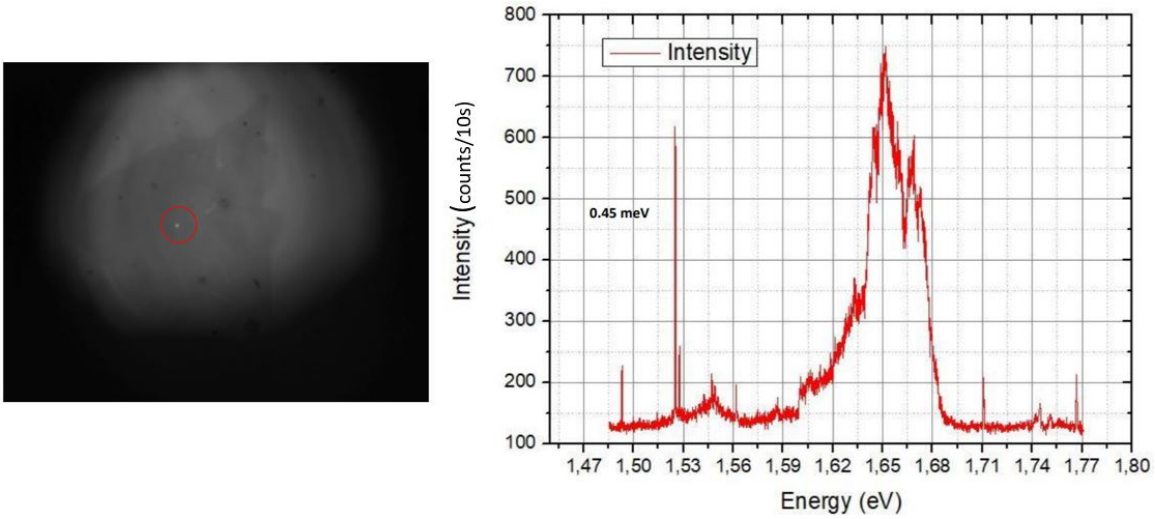

Figure 5.6: (Left) View of the flake from the imaging camera. The white spot is the laser. (Right) PL measurement of an emitter in the monolayer. A first clean signal around 1.65 eV is present. There is also a small increase in signal around 1.53 eV. They came from neutral exciton and defects-bound exciton. The measurement was taken at 4K, with a green laser (HeNe 532.2 nm) excitation at 66nW. The integration time is 10s.

Then in Fig. 5.7 a monolayer emitter spectrum is shown. In this case, the transition lines around 1.53 eV are more visible. These lines comes from defect-bound excitonic transitions and thus they are at lower energy with respect to the neutral excitonic transition lines[68].

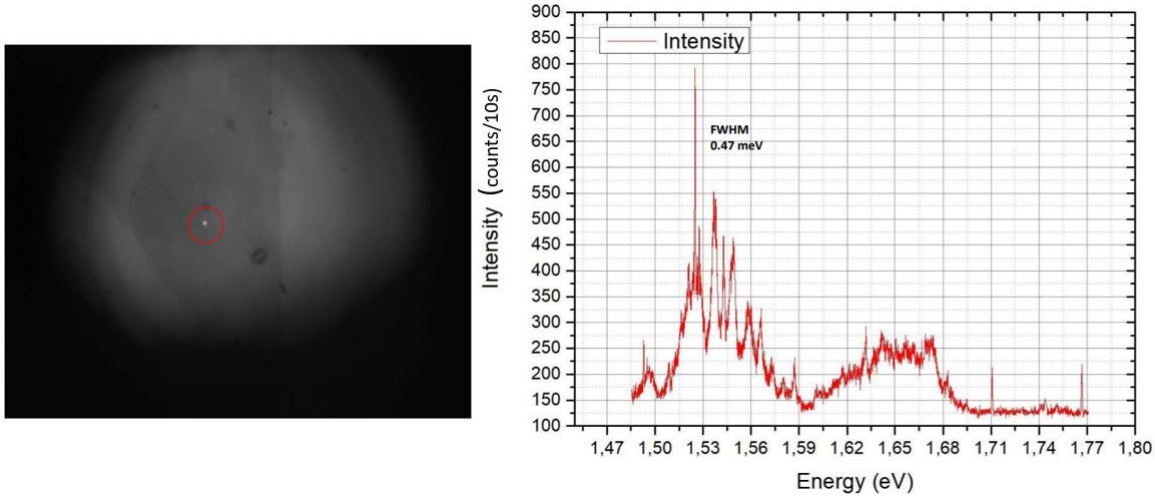

Figure 5.7: (Left) View of the flake from the imaging camera. The white spot is the laser. (Right) PL measurement of an emitter in the monolayer. A low signal around 1.65 eV is present. Sharp defects-bound excitonic lines are visible around 1.53 eV. The measurement was taken at 4K, with a green laser (HeNe 532.2 nm) excitation at 66nW. The integration time is 10s.

In Fig. 5.8 another monolayer spectrum is shown. As we see, the intensity and the sharpness of the lines highly depend on the chosen emitter and as we will see later, it depends also on the quality of the produced sample.

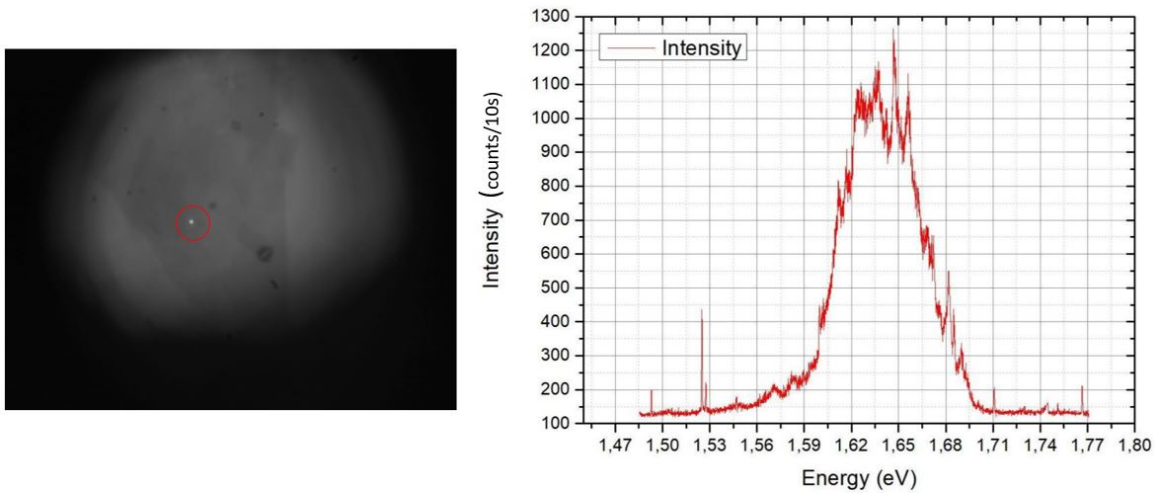

Figure 5.8: (Left) View of the flake from the imaging camera. The white spot is the laser. (Right) PL measurement of an emitter in the monolayer. For this emitter just the free excitons signal around 1.65 eV is present. No defects-bound excitonic lines are visible around 1.53 eV. The measurement was taken at 4K, with a green laser (HeNe 532.2 nm) excitation at 66nW. The integration time is 10s.

In Fig. 5.9, a bilayer PL signal is shown. We observed that defects-bound exciton transitions in bilayer are the most intense corresponding to the sharp lines in the spectra, reaching an intensity ten to twenty time higher than the monolayer signal. Such a high number of counts allowed us to perform radiative lifetime measurements but not $g^{(2)}(\tau)$ measurements for sample 1.

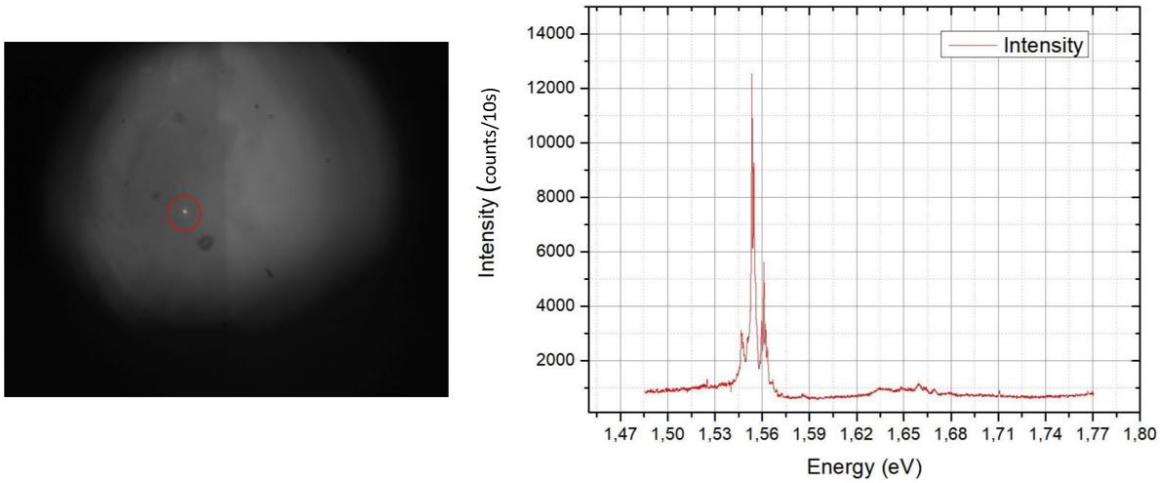

Figure 5.9: (Left) View of the flake from the imaging camera. The white spot is the laser. (Right) PL measurement of an emitter in the bilayer. For this position just a signal around 1.55 eV is present. Thus just defects-bound excitonic lines are visible. The intensity of the peaks is very high compared with the intensities of the monolayer peaks. The measurement was taken at 4K, with a green laser (HeNe 532.2 nm) excitation at 66nW. The integration time is 10s.

Power dependence measurements were performed for a chosen defect-like emitter. We performed this measurement for two reasons. First, to discriminate eventual parasitic signal. Second, to observe the characteristic behaviour of a two-level system versus excitation power [24] and to determine the saturation power. This value defines the maximum value we should

not exceed. Thus, in Fig. 5.10 the PL spectra for the same emitter for different values of excitation power is shown.

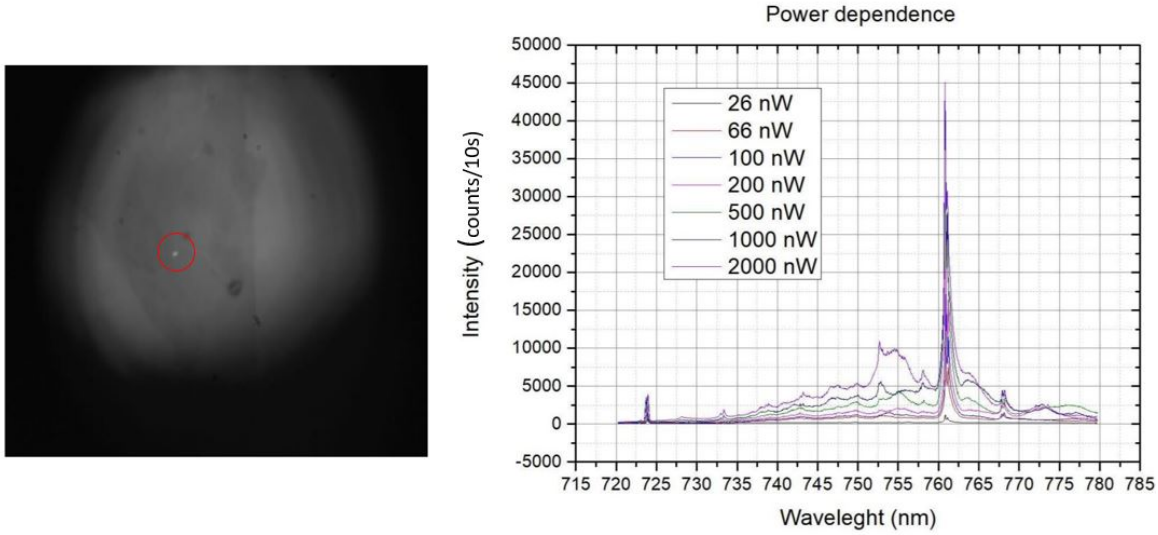

Figure 5.10: (Left) View of the flake from the imaging camera. The white spot is the laser. (Right) PL spectra for an emitter in the monolayer for different values of excitation power is shown.

It is useful to observe that the artefact peaks (around 723 nm) do not present any power dependence. Then we plotted in Fig. 5.11 the intensity values of the 760 nm peak as a function of the power. We extracted a saturation power of 3 μW for the CW green laser. Moreover we performed a fit with the 2-level system fitting function used in [24] to prove the 2-level nature of the system, see Appendix A. for a detailed explanation of the intensity saturation for a 2-level system.

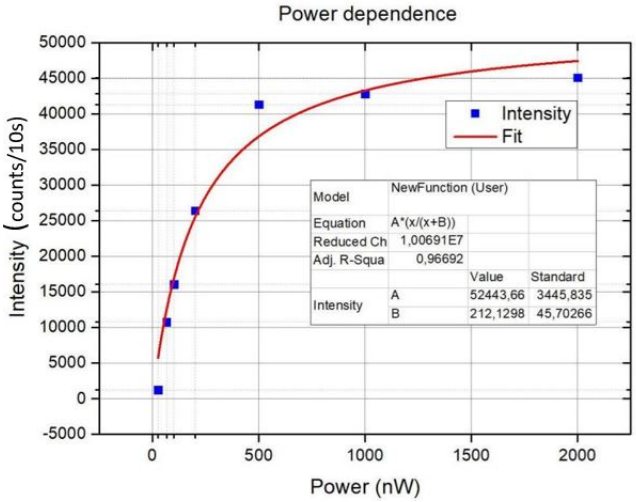

Figure 5.11: Plotted intensities of the peak at 760 nm as a function of power. The red line is the 2 level system fit. We extracted a saturation power of 3 μW for the CW green laser.

Moreover, we substituted the green laser with a Ti-Sa laser mode-locked at 710 nm. Thus we lowered the energy of the laser to reduce the charge injection through an higher energy laser. In Fig. 5.12 and Fig. 5.13 we can observe the PL signal for two different emitters collected

both with the green laser and the Ti-Sa red laser, using the same power and integration time, proving, as expected, to have a better PL signal using the red laser.

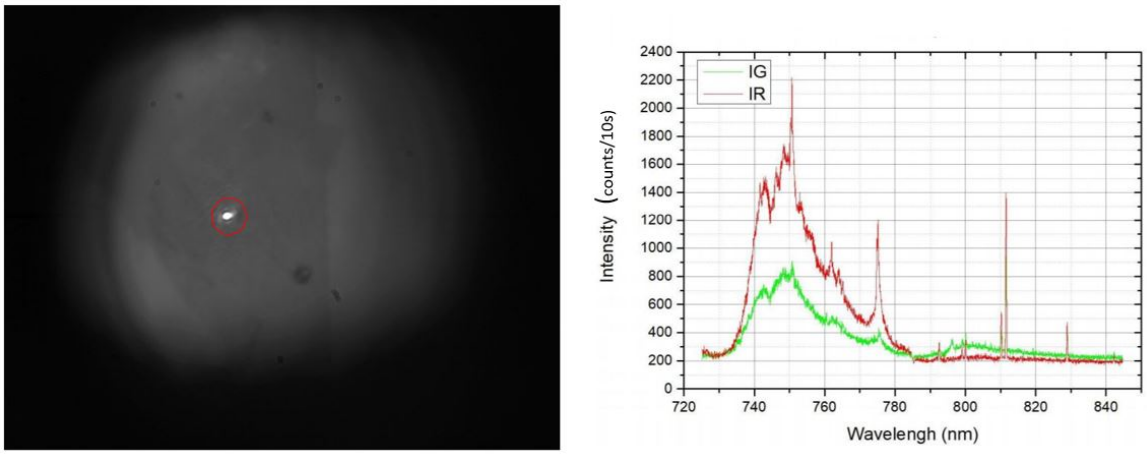

Figure 5.12: (Left) View of the flake from the imaging camera. The white spot is the laser. (Right) Green laser versus red laser PL signal for an emitter in the monolayer. The green line is for the green laser and the red for the red laser. We observe a three times increased intensity magnitude using the red laser and also a cleaner signal where the lines become more sharp and isolated.

We observe a three times increased intensity using the red laser and also a cleaner signal where the lines become more sharp and isolated.

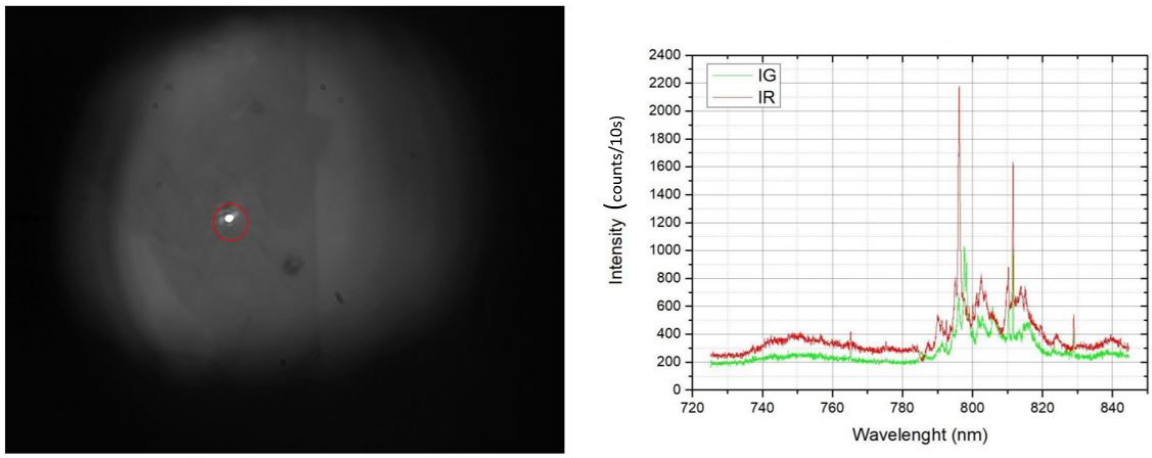

Figure 5.13: (Left) View of the flake from the imaging camera. The white spot is the laser. (Right) Green laser versus red laser PL signal for an emitter in the bilayer. The green line is for the green laser and the red for the red laser. We observe a two times increased intensity magnitude using the red laser and also a cleaner signal where the lines become more sharp and isolated.

5.3 Time correlated measurements sample 1

5.3.1 Radiative lifetime measurements

In this section, the radiative lifetime measurements of given emitters of sample 1 will be presented. We performed firstly a PL scanning of the sample in order to find the emitters that gave us more signal. A well spectrally isolated line is necessary for the T_1 measurements, as explained in Chapter 4.

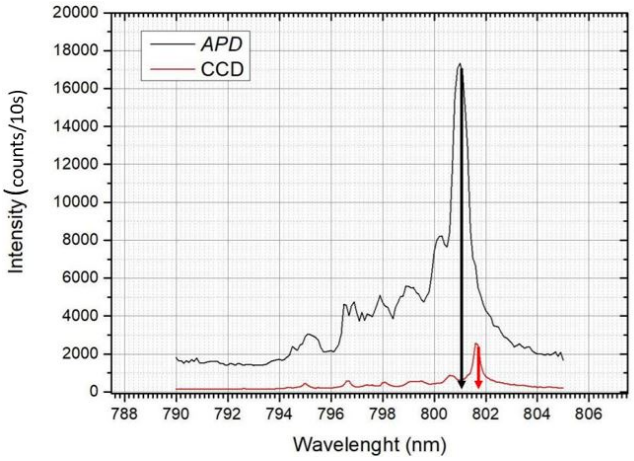

Figure 5.14: APD and CCD spectrum comparison. The background noise in the APD is higher than in CCD but the APD signal is more intense. Comparing the plots we observe a small shifting of about 0.3nm between the spectrum of the CCD and APD due probably to some internal slight misalignment in the spectrometer.

This technique allowed us to obtain the plot shown in Fig. 5.14. Even though the background noise in the APD was higher than in CCD, it is clear that the APD signal is more intense, granting the good counts conditions to obtain a good measurement of the lifetime in a rational waiting time. Observing the plots in Fig. 5.14, we noted a small shifting of around 0.3nm between the spectrum of the CCD and APD, the value of which, dependent on the alignment, needed to be taken in account for the choice of the peak.
In the next figures the lifetime results are shown. The probability distribution of the decaying time follows an exponentially decaying rule, thus to extract the lifetime, we plotted the graph in log scale and performed a linear fit. Calculating the inverse of the slope we obtained the lifetime. We measured the T_1 for three different peaks obtained from two defects-bound excitons emitters (one peak in position 1 and two peaks, left and right, in position 2) and for the right peak of the emitter in position 2 we measured the lifetime for two values of the laser power. All the emitters present long lifetime in the order of magnitude of dozens of nanoseconds, in agreement with literature values [68]. For the first peak (position 1) analyzed we obtained a lifetime of 27.7 ± 0.9 ns, as depicted in Fig. 5.15.

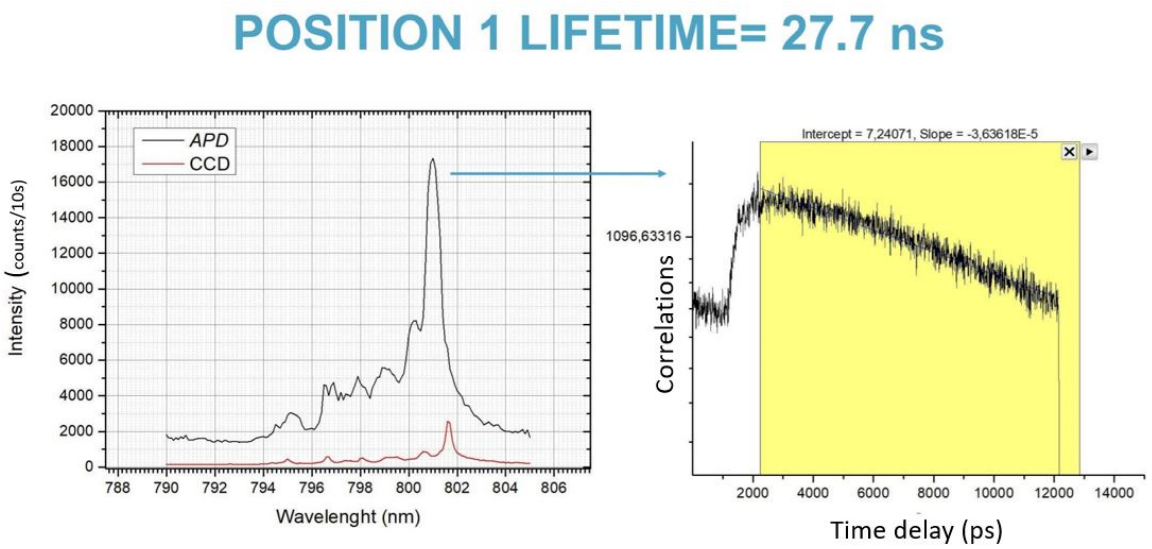

Figure 5.15: In the left part of the figure, the APD and CCD spectrum of the defect-bound excitonic emitter in position 1 is shown. In the right part the radiative lifetime measurement in log scale as well as the linear fit is plotted. The extracted lifetime is 27.7 ± 0.9 ns. We used pulsed Ti-Sa (80 MHz) laser at a power of 20 μW and a integration time of 1s.

For the emitter in position 2 two peaks are present and we measured the lifetime for both transitions. For the left peak the spectrum and the lifetime plot is shown in Fig. 5.16 from which we extracted a lifetime of 12.2 ± 0.8 ns.

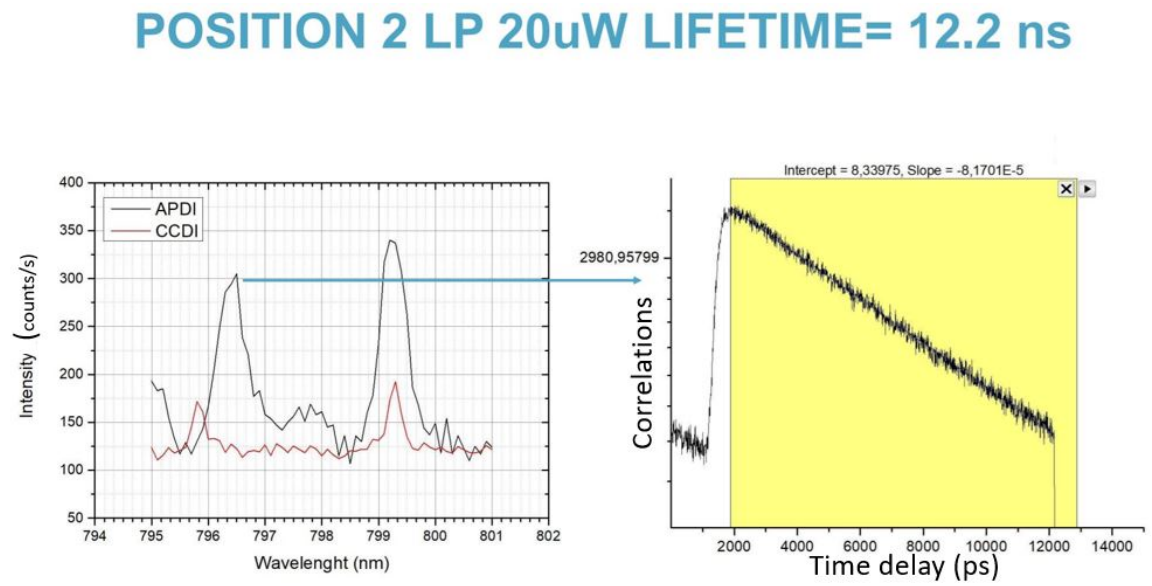

Figure 5.16: In the left part of the figure, the APD and CCD spectrum of the defect-bound excitonic emitter in position 2 is shown. Two peaks are present. In the right part the radiative lifetime measurement of the left peak in log scale as well as the linear fit is plotted. The extracted lifetime is 12.2 ± 0.8 ns. We used pulsed Ti-Sa (80 MHz) laser at a power of 20 μW and a integration time of 1s.

For the right peak the spectrum and the lifetime plot is shown in Fig. 5.17 from which we extracted a lifetime of 12.1 ± 0.3 ns. For the right peak the spectrum and the lifetime plot is shown in Fig. 5.17 from which we extracted a lifetime of 18.5 ± 0.2 ns.

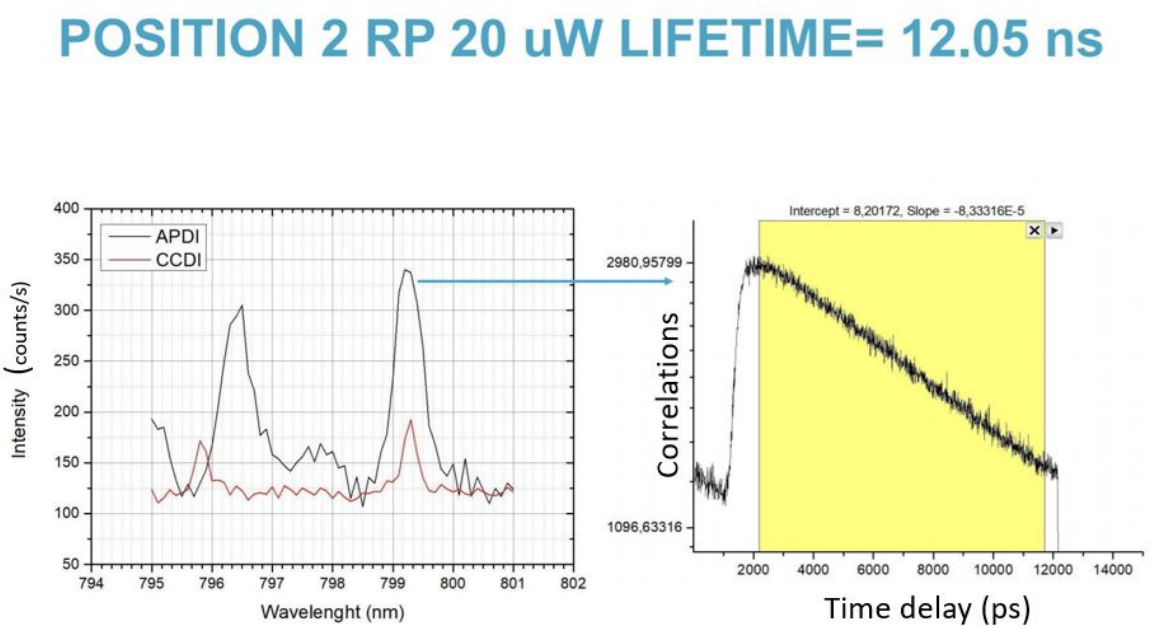

Figure 5.17: In the left part of the figure, the APD and CCD spectrum of the defect-bound excitonic emitter in position 2 is shown. Two peaks are present. In the right part the radiative lifetime measurement of the right peak in log scale as well as the linear fit is plotted. The extracted lifetime is 12.1 ± 0.3 ns. We used pulsed Ti-Sa (80 MHz) laser at a power of 20 μW a integration time of 1s.

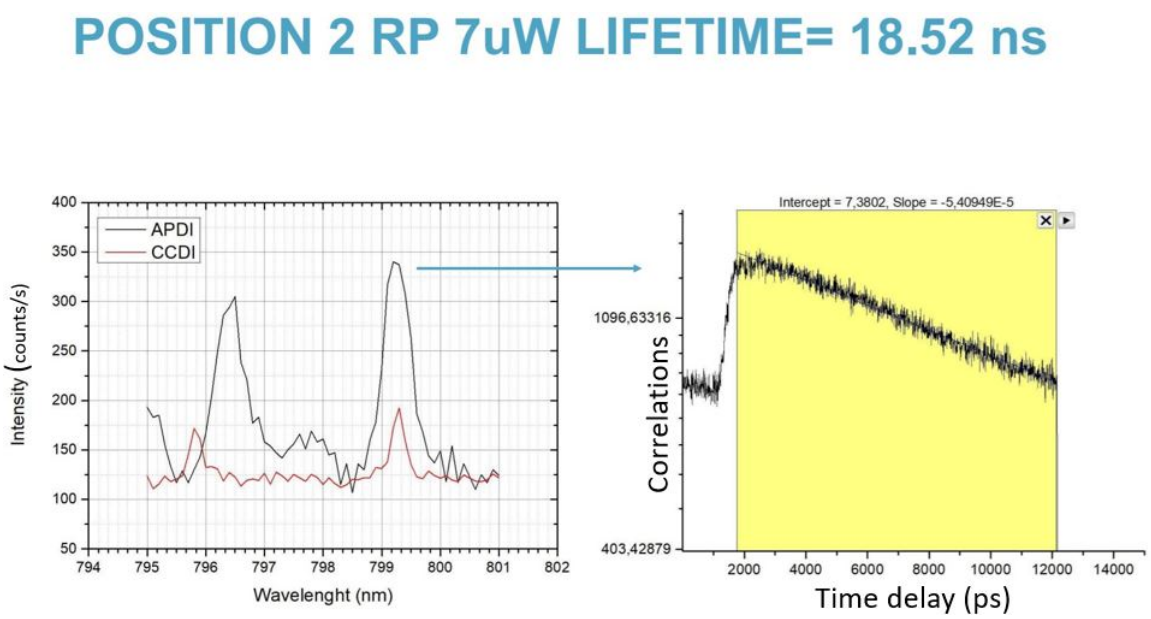

Figure 5.18: In the left part of the figure, the APD and CCd spectrum of the defect-bound excitonic emitter in position 2 is shown. Two peaks are present. In the right part the radiative lifetime measurement of the left peak in log scale as well as the linear fit is plotted. The extracted lifetime is 18.5 ± 0.2 ns. We used pulsed Ti-Sa (80 MHz) laser at a power of 20 μW and a integration time of 1s.

As we see from the comparison between Fig. 5.17 and Fig. 5.18, we measured 18.5 ± 0.2 ns for the right peak at a lower power. Thus, we have a longer lifetime for a lower power excitation. However, from the data we have we can not conclude some power dependence of the lifetime. In theory, is possible to find very different values of the lifetime of the emitters, depending on

their nature (interlayer excitons, defect bound excitons, dark or bright excitons...) [68]. An advantage of the TMD materials is the possibility to control the lifetime of the emitters by playing with different materials. In fact, one can play with the substrate material [2] or with the thickness of the hBN used as encapsulation [71]. The flexibility to generate emitters over a wide range of lifetimes in a single material system, has potential in many optical quantum computing applications like quantum memory devices [11].

5.4 Optical characterization of sample 2

The evaluation of the $g^{(2)}(\tau)$ for the emitters found in sample 1 was impossible since we just found emitters with low counts. It would be thus impossible measure the $g^{(2)}(\tau)$ since to do it we need to 50:50 split the signal into the two APDs reducing even more the low signal we had. We needed to produce a new sample (sample 2) to obtain a clean enough sample to provide good counts emitters. The results of the basic and detailed optical characterization of sample 2 is presented here. In Fig. 5.19 the microscope of the best sample we produced, in terms of optical response. In the right picture the expected active region is enlightened. The following optical characterization was performed on this sample.

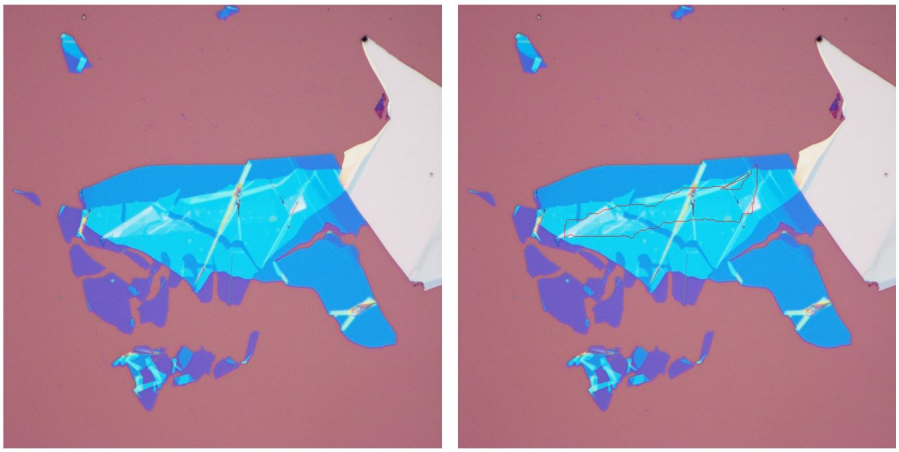

Figure 5.19: Optical microscope pictures of the $hBN/WSe_2(ML)/hBN$ produced in clean room. In the right picture the expected active region is enlightened.

5.4.1 PLE measurements

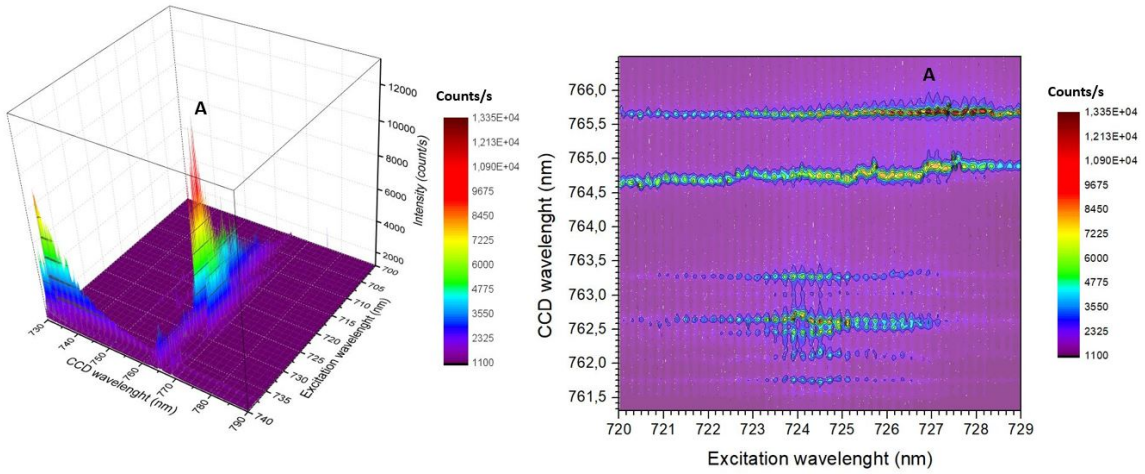

Figure 5.20: PLE measurements for a chosen emitter varying the excitation wavelength of the Ti-Sa laser from 700 to 740 nm. (Left) The entire spectrum. We note an absorption resonance at 740nm for the peak at 730nm while a resonance at about 727 nm for the lines at 765nm. (Right) Zoom on the CCD spectral range from 760 to 766nm. The presence of two lines can be observed. The line labeled A at 765.6 nm and a second line at 764.6 nm. Line A is the most intense and has a resonance at an excitation wavelength of 727.5 nm. We note how line A is subject to weak charge effects and therefore spectrally stable with respect to the excitation wavelength change.

For the optical characterization of sample 2 we started with a PLE measurement. PLE stays for photoluminescence excitation spectroscopy (PLE), and means that we detect the PL at a given energy while varying the energy of the excitation. Thus, one can determine what the resonance in the absorption spectrum. The PLE spectrum for a chosen emitter is shown in Fig. 5.20. We have changed the excitation wavelength of the Ti-Sa laser from 700 to 740 nm. The entire spectrum is shown in Fig. 5.20 (left). We note an absorption resonance at 740nm for the peak at 730nm while a resonance at about 727 nm for the lines at 765nm. In Fig. 5.20 (right) a zoom is shown on the CCD spectral range from 760 to 766nm, thus, close to the line labeled A in Fig. 5.20 (left). The presence of two lines can be observed. The line labeled A at 765.6 nm and a second line at 764.6 nm. Line A is the most intense and has a resonance at an excitation wavelength of 727.5 nm. This will be the excitation wavelength of the Ti-Sa that we will use for the optical characterization of sample 2. Furthermore, we note how line A is subject to weak charge effects and therefore spectrally stable with respect to the excitation wavelength change. We will therefore use the spectral line A for the measurement of T_1 and $g^{(2)}(\tau)$ in the following sections. These PLE data gives us the possibility to carry out a detailed analysis of the electronic structure of the emitter in the future.

5.4.2 Micro-PL and power dependence measurements performed on sample 2

As shown in Fig. 5.21, we found very good defect-bound excitonic emissions with an intensity almost hundred times higher than the ones in the previous sample. We used the Ti-Sa laser at $1\mu W$ tuned at the best excitation wavelength found in the PLE analysis, thus 727.5 nm. All the plots are obtained for 1s of integration time.

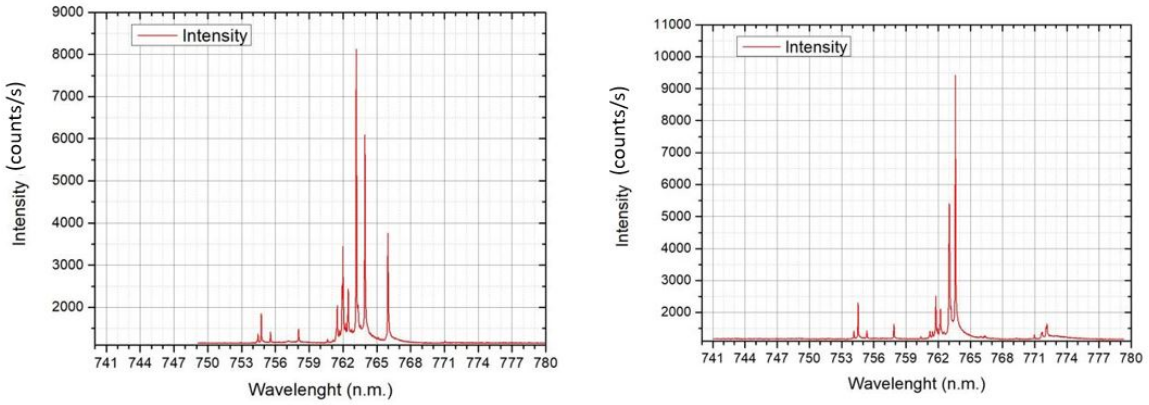

Figure 5.21: Different PL signal from two emitters found in the new sample. We used the TiS laser with a power of $1\mu W$ tuned at the resonant excitation wavelength found in the PLE analysis, thus 727.5 nm. All the plots are obtained for 1s of integration time.

The excitation power dependence measurements will be presented for A and B lines of the spectrum in Fig. 5.22. We performed the same fit with a 2-level system fitting function to prove the 2-level nature of the system. This time we extracted a saturation power of 4 μW. However, we didn't risk to explore that power value, avoiding to expose the sample to too much high powers. We decided to use $1.5\mu W$ for the next measurements.

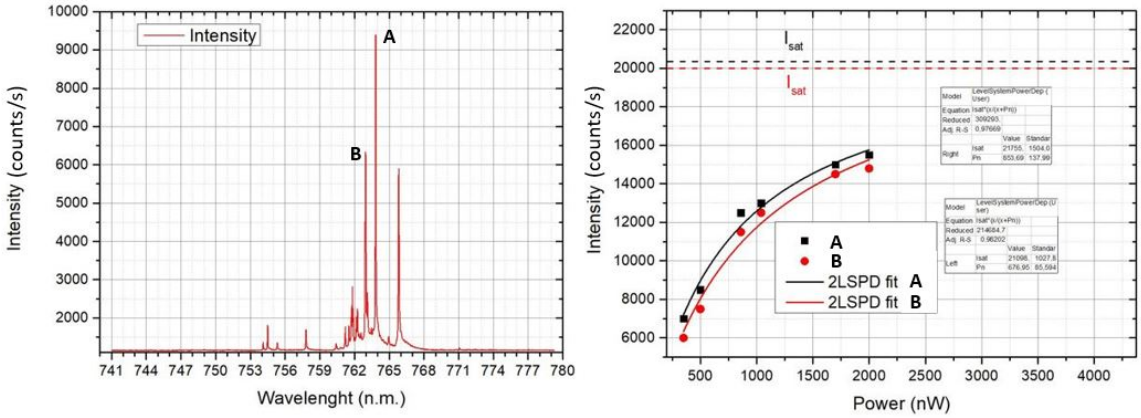

Figure 5.22: Power dependence measurements performed over the two highest peaks of the emitter shown in the left figure. The right picture shows the fit with a 2-level system fitting function to prove the 2-level nature of the system. The expected saturation intensity are depicted as well. The saturation power we obtained is 4 μW.

5.5 Time correlated measurements sample 2

5.5.1 Radiative lifetime measurements

Then we moved towards the measurements of the radiative lifetime for the A peak in Fig. 5.22. In Fig. 5.23 the spectra of the emitter collected using one and two APDs is shown. As expected, the signal is half splitted in the two APDs and no shift between them is registred.

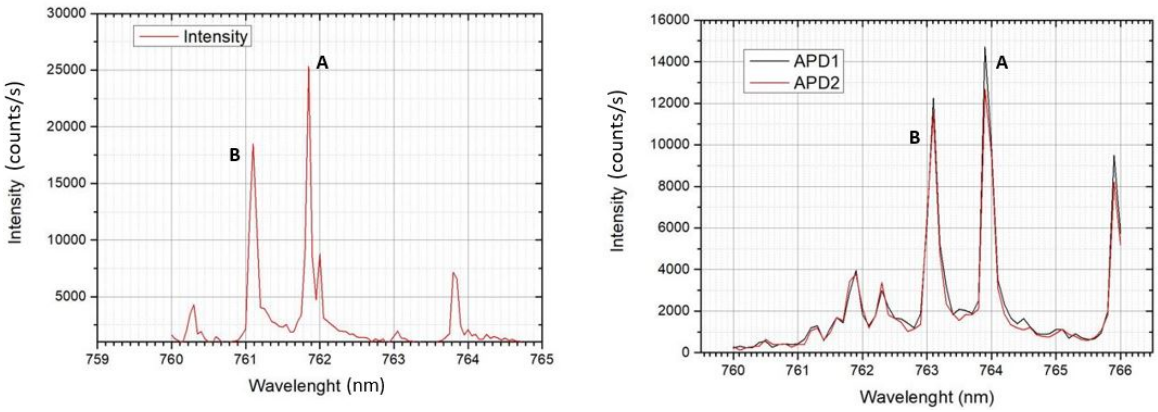

Figure 5.23: Recorded spectra through one APD (left) and two APDs(right) of the same emitter recorded through the CCD in Fig. 5.22. We used the TiS laser with a power of $1.5\mu W$ tuned at the resonant excitation wavelenght found in the PLE analysis, thus 727.5 nm.

The result of the lifetime measurement performed on A peak for two different laser power values (2 and $0.4\mu W$) are shown in Fig. 5.24. We extracted a lifetime of around 5ns (5.2 ± 0.9 ns and 5.0 ± 0.3 ns) for both power values, excluding a high dependence of the lifetime from the excitation power. The results are comparable with the ones in literature [68].

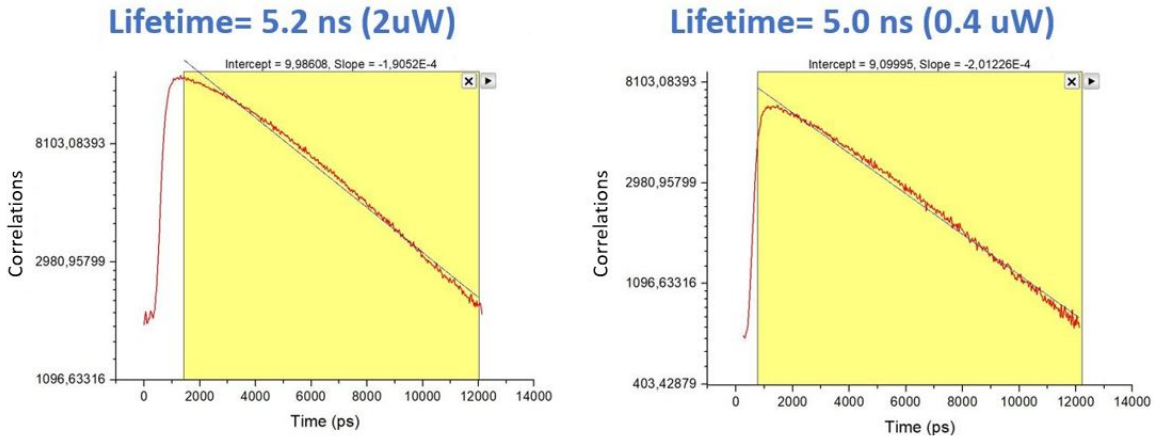

Figure 5.24: Lifetime measurement performed for two different laser power values (2 and $0.4\mu W$). We extracted a lifetime of around 5ns (5.2 ± 0.9 ns and 5.0 ± 0.3 ns) for both power values.

Comments on the T_1 measurements for sample 1 and sample 2

Disorder derived from defects or strain in monolayer TMDs can lead to a dramatic change in the physical behavior of the interband excitations, producing inhomogeneous spectral broadening and localization leading to radiative lifetime increase. We proved that localized excitons have a longer emission time than free excitons (picoseconds) [2]. Localized exciton in monolayer WSe_2 are described within Wannier- Mott exciton model, presented in Chapter 1. The difference between the lifetimes of sample 1 and sample 2 is compatible with the presence of very different strains in the two samples. We expect a shorter the lifetime for a stronger confinement. For a weak confinement, on the other hand, there is a small overlap of the wave function of the electron and that of the hole and therefore a longer lifetime. The strenght of the confinement can result from clean room manufacturing or local inhomogeneity of the samples.

5.5.2 $g^{(2)}(\tau)$ measurements

On the same peak (peak A) we measured the $g^{(2)}(\tau)$, using both the mode-locked TiS laser in pulsed mode and in CW. The results are shown in Fig. 5.25 and Fig. 5.26 respectively. It is easy to see how the single photon source property is evident since in both configurations we can observe a drop in counts for a delay value of 0.

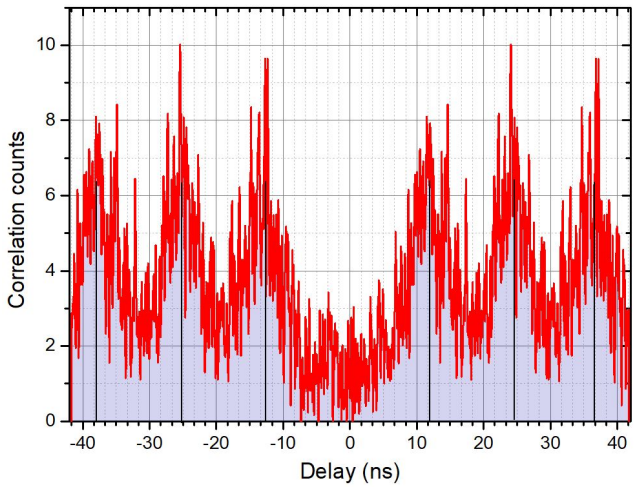

Figure 5.25: Recorded $g^{(2)}(\tau)$ in pulsed mode. The lateral peaks are centred at integer multiples of the laser pulses (almost 12ns). The single photon source nature is evident from the absence of peak for zero delay.

To extract the value of $g^{(2)}(0)$ in pulsed mode, one shoud perform a multi peaks Lorentz functions fit on the peaks and normalizing the value of the average area below the lateral peaks to 1 it is possible to extract the value of the area below the peak centered in 0, i.e. the value of $g^{(2)}(0)$. The analysis in CW is faster, thus we used the pulsed measurements just to prove the single photon source of the state [24].

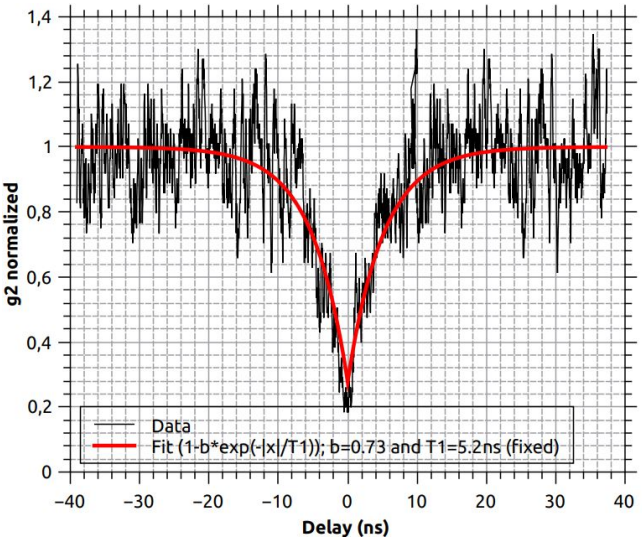

Figure 5.26: Recorded $g^{(2)}(\tau)$ in CW mode. The single photon source nature is evident from the absence of correlation counts for zero delay. We fitted fixing the T_1 measured for this line in the previous section. The extracted $g^{(2)}(0)$ value is 0.21 ± 0.02 plus 0.06 due to the correlation APD dark counts.

To extract the value of $g^{(2)}(0)$ in continuous mode, instead, we just normalized to one

the counts for long delay and using the fitting function presented in equation 2.60, where we inserted the measured T_1 of the line of 5.2ns. As expected, the function fit well the data and we could extract y-axis value of the peak to find $g^{(2)}(0) = 0.21 \pm 0.02$ plus 0.06 due to the correlation APD dark counts. The fitting function is shown in the inset in Fig. 5.26. The result is in agreement with the expected value for a single photon source [30], i.e. less than one half. The value found could be further lowered if the effect of the resolution of the APDs on the counts is taken into account. However, the discussion is not trivial and not necessary for the demonstration of single photon source nature of the emitter, therefore it is not reported here.

5.6 Simulations and fiber preparation

In this part the COMSOL and MATLAB simulations will be presented. Then, the tapered fiber preparation based on the simulation results will be shown.

5.6.1 Simulations

The main aim of the simulation analysis of the system was to understand which was the right diameter of the tapered fiber we needed to have to get a spatial broad enough evanescent field to enable the radiative mode coupling with the defect-bound excitons in the WSe_2 billayers by deposing the fiber directly above the emitter, through the use of a piezoelectric moving stage inside the cryostat. By changing the diameter of the fiber until we got the desired evanescent field, we found that the first right one was on the order of magnitude of 600nm. Thus we present the results for that diameter value.

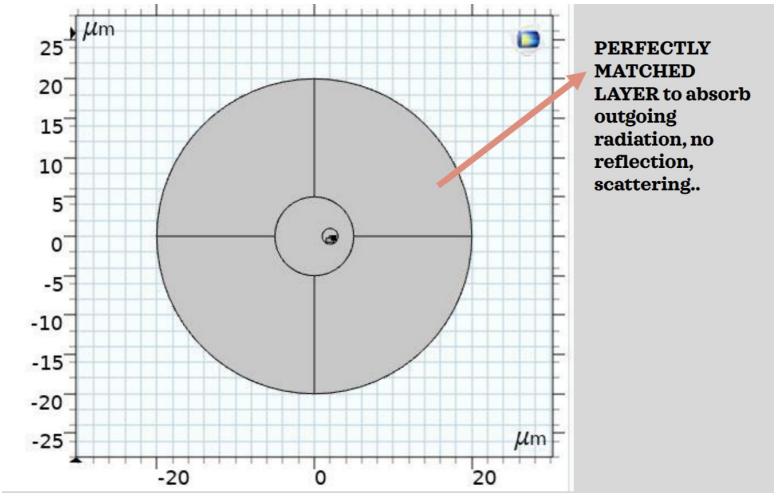

Figure 5.27: Input model for the simulation. We see the Perfectly Matched Layer (PML) domain, that can be used to reduce the computational area when one wants to simulate waves propagating in free-space.

Basically, here one needs to solve Maxwell equations imposing the right boundary conditions and inserting the right value of the parameters of the materials to extract the propagating modes and their amplitude. Fig. 5.27 and Fig. 5.28 present the input model we used to simulate our system. In Fig. 5.27 the attention is focused to the Perfectly Matched Layer (PML) domain, that can be used to reduce the computational area when one wants to simulate waves propagating in free-space. The PML is not a boundary condition, but rather a domain that can be added along the exterior of the model to absorb all outgoing waves. Mathematically

speaking, the PML is simply a domain that has an anisotropic and complex-valued permittivity and permeability [10]. Then, in Fig. 5.28 a zoom over the sample is shown as well as the mesh. The mesh represents the computational surface taken into account from the software.

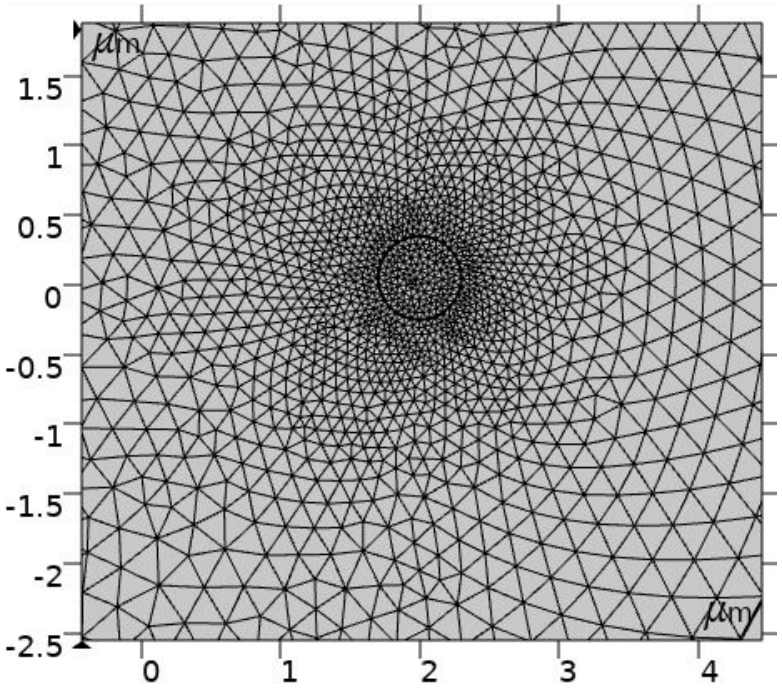

Figure 5.28: Zoom on the fiber with visible mesh. It is automatically finer close to the border of two different materials. The mesh represents the computational surface taken into account from the software.

The circular object is the optical fiber. It is just composed by the core. The reason is that since we are dealing with radiation at a wavelength around 800nm and the final optical fiber dimension will be of roughly 600 nm of diameter, we find our self in the sub-wavelength regime and thus there is no difference for the wave to propagates in the core or in the cladding. In Fig. 5.28 we note the mesh division, that is the computational areas, of the system and we see that it is automatically finer close to the system borders. Finally we computed the mode propagating in the system and we found the one proper of the fiber, indeed we found that for a 800nm wavelength and 600nm of dimension, the optical fiber is a single mode fiber.

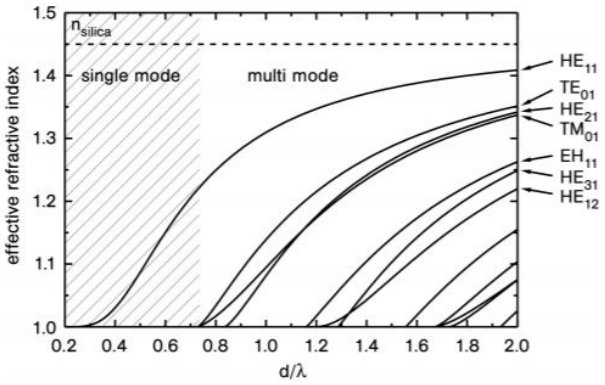

Figure 5.29: Effective refractive index for the fundamental mode and a higher order modes as a function of the fiber diameter normalized over the wavelength value. From this plot we expect a n_{eff} value of about 1.2, so a little bit higher than the one we obtained for a diameter of 600nm and a wavelenght of 800 nm. Figure extracted from [20].

We found that the effective refractive index of the only propagating mode was 1.0211. Indeed, light propagation in a nanofiber is usually described using the concept of an effective refractive index $n_{eff} = c/v_{phase} = \beta/k_0$, where c is the vacuum speed of light, v_{phase} is the phase velocity of the mode, β is the mode propagation constant, and $k_0 = 2\pi/\lambda$ is the vacuum wavenumber [20].The propagation constant is obtained by solving the transcendental equation arising from the Maxwell's equations imposing the right boundary conditions for the nanofiber geometry, thus different value of the refractive index coincide with different propagation modes, as depicted in Fig. 5.29. The 2D sketch of the intensity of the three components and the modulus of the electric field are shown in Fig. 5.30.

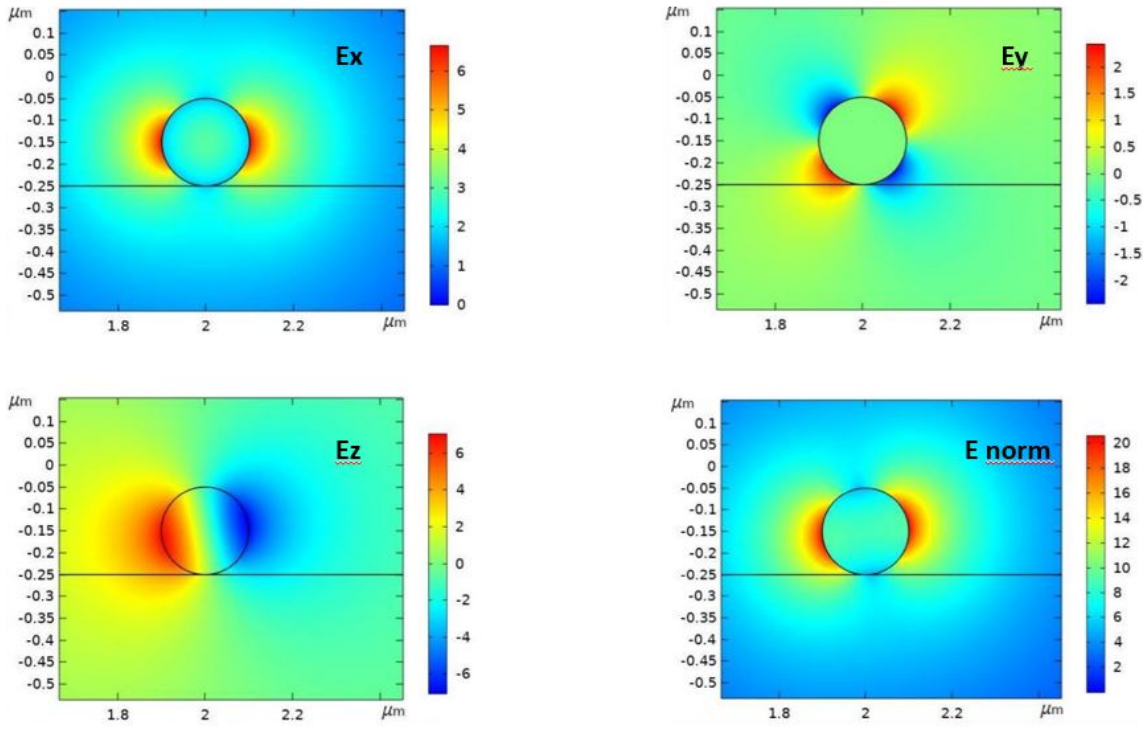

Figure 5.30: 2D representation of the electric field amplitude in the three directions and its modulus, the results are obtained through COMSOL.

Even though the results were in agreement with literature according to [63], in Fig. 5.31, and satisfying for what concerned the evanescent field value and geometry, well visible outside the fiber, we found some anomalies on the modulus of the electric field. In fact, we noted that the maximum of the intensity of the electric field modulus is not at the center of the fiber, but outside, this would be bad for the propagation losses. Thus we tried to repeat the calculations, these time using the MATLAB toolbox developed by Karapetyan et al. [28]. The results are shown in Fig. 5.32 and 5.33 with a 3D representation.

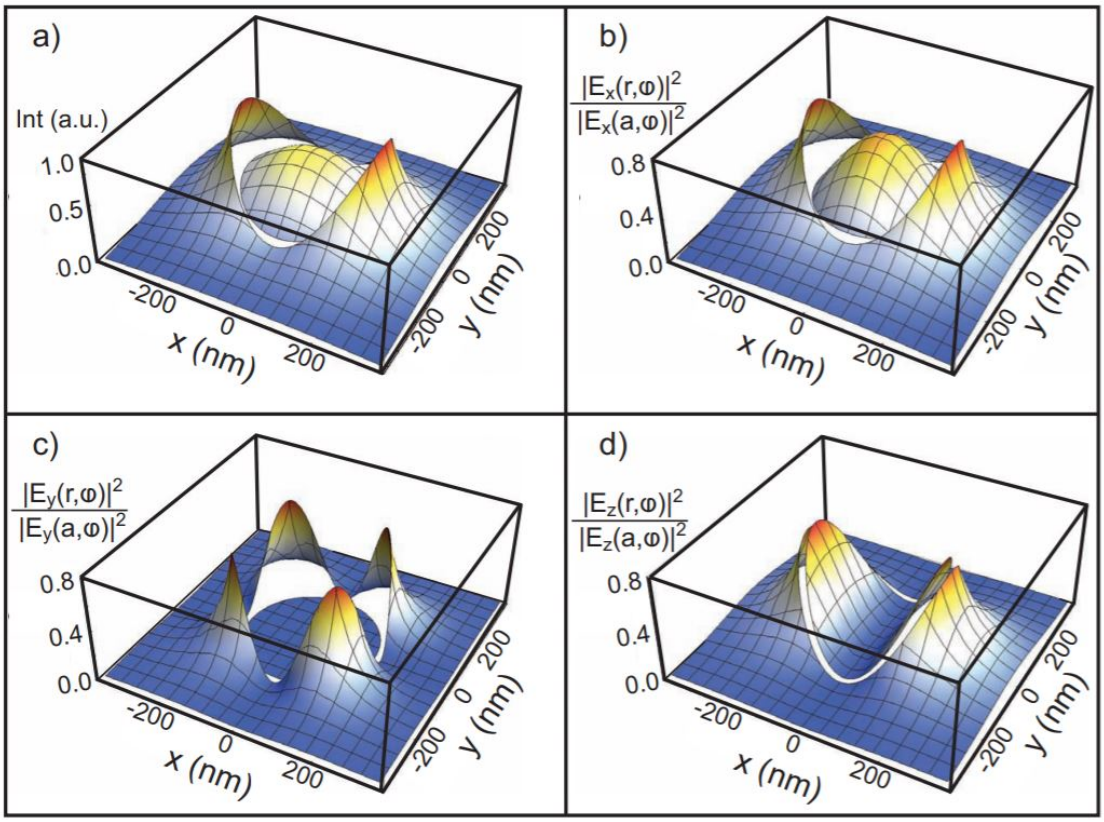

Figure 5.31: Fundamental (HE11) mode structure of 360-nm diameter nanofiber. A Total intensity normalized to its maximum value. B Intensity of the x component normalized to its maximum value at the nanofiber radius (a). C Intensity of the y component normalized to its maximum value at the nanofiber radius (a). D Intensity of the z component normalized to its maximum value at the nanofiber radius (a). Figure extracted from [63].

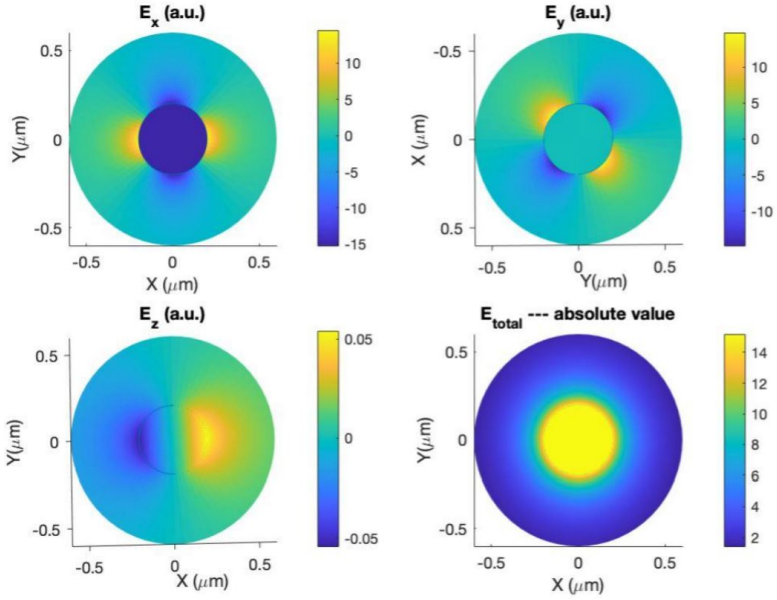

Figure 5.32: 2D representation of the electric field amplitude in the three directions and its modulus, the results are obtained through MATLAB.

It is clear that the difference is with the x-component of the electric field found in the COMSOL simulation, since with MATLAB we obtained the maximum intensity in the centre of the fiber.

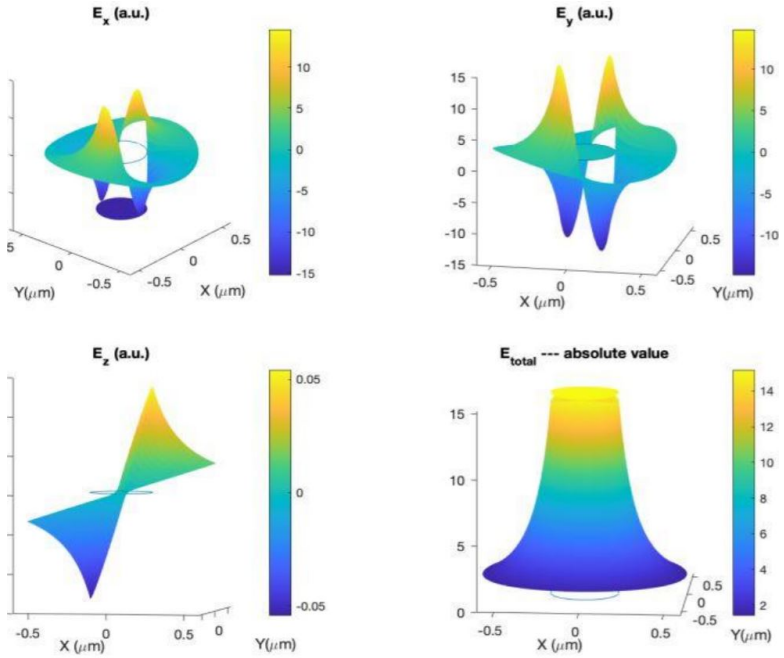

Figure 5.33: 3D representation of the electric field amplitude in the three directions and its modulus, the results are obtained through MATLAB. As we expected, the maximum amplitude of the mode is in the fiber centre.

We saw that COMSOL gave two equal results with the same effective refractive index value of 1.0211, indicating so the same mode of propagation. However the two solutions have different angles but the same shape. We understood that they correspond to two possible solutions of the problem but with different spatial distributions, the results are shown in Fig. 5.34.

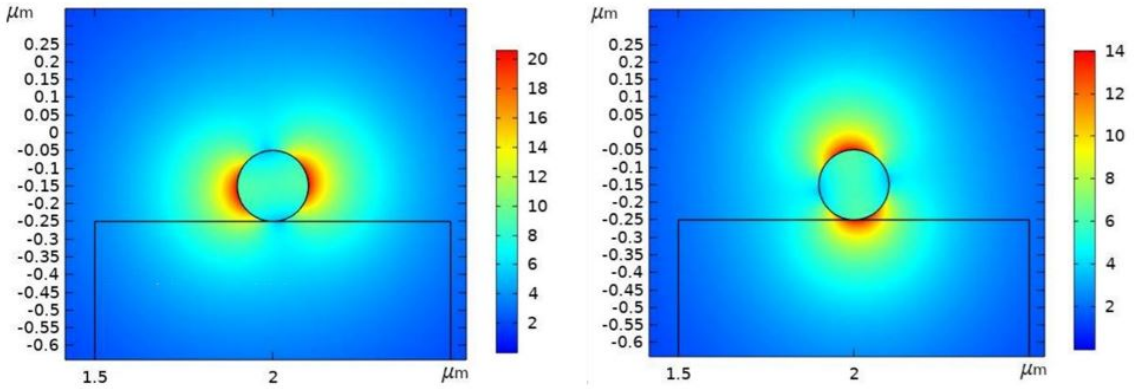

Figure 5.34: Representation of the two solutions found by COMSOL. They manifest qualitatively the same result, since they are defined by the same effective refractive index value of 1.0211 but with different geometry.

Indeed they represents two equiprobable solutions and we calculated the weighted average of the two and plotted it in 3D in Fig. 5.35, using ABC as axes. Now the solution is quantitatively better, as we observe an acceptable value of intensity in the centre of the fiber and a 3D shape similar to the one obtained with MATLAB but still with the highest value outside the fiber.

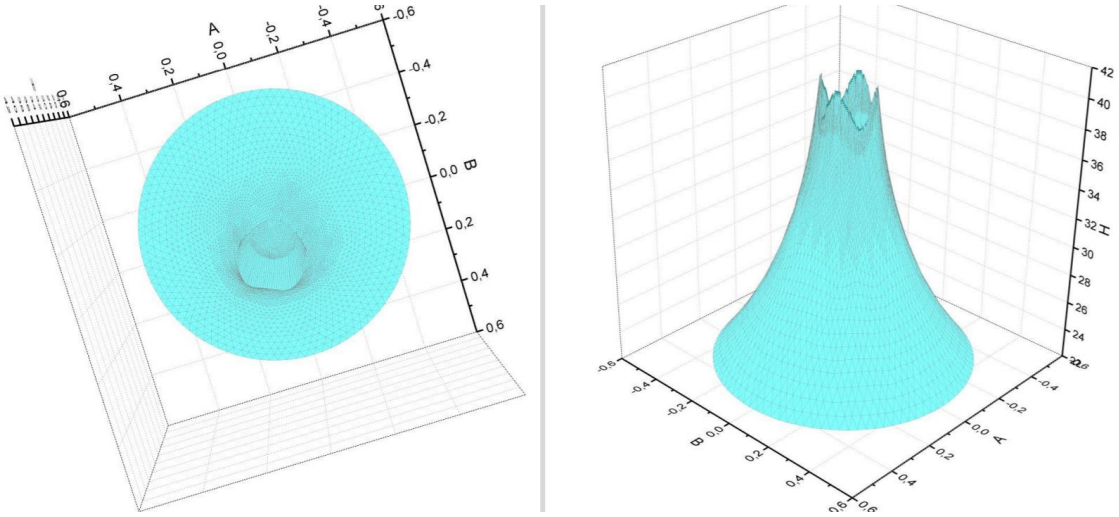

Figure 5.35: Weighted average of the two solutions plotted in 3D. The ABC axis correspond to XYZ and the scale is in micrometers.

Simulations comments

The difference between the results obtained from COMSOL and MATLAB simulations depends on the different analysis method used by the two programs. While COMSOL uses the finite elements method (FEM), MATLAB analytically solves Maxwell's equations taking in consideration the transformation within hybrid modes explained in Chapter 3, providing exact results. To question the validity of the COMSOL simulations we can compare the intensities at 50 nm outside of the fiber with respect to the maximum intensity. We found 60% for MATLAB and 67% with COMSOL. Therefore the two simulations indicate compatible results. However the COMSOL results are good enough to fulfill the fundamental condition to have an evanescent field well visible outside the fiber, laying the theoretical foundations for the success of the fiber coupling experiment.

5.6.2 Tapered optical fiber preparation

In this section is shown how we managed to manufacture a nanofiber with a tip diameter of no more than 600nm, i.e. the maximum value of the fiber tip diameter that guarantees a good evanescent field, which we found through COMSOL simulations. Starting from a pure silica optic fiber with a cladding diameter of 125 μm, when tapering we needed to take into account that, physically, the decrease of the diameter of the core leads to a compression of the guided mode until the mode diameter reaches a minimum. If we reduce more the core diameter then we would get an expansion of the mode into the cladding. The cladding then acts as the new guiding medium, increasing the transmission losses. It is proven that this mode conversion should be adiabatic, to have no coupling of the fundamental mode to higher transverse or radiative modes. This can be achieved by maintaining the tapering angles as small as possible, thus having the tip as long as possible [20].

Fabrication

For the fabrication of the fibers we used a laser-based micropipette puller, model P-2000 produced by SUTTER INSTRUMENTS, it is shown in Fig. 5.36. The puller integrates a CO_2 laser-based heat source to melt the fiber before pulling them and so cut them. The idea is to let the laser heat up the fiber and then controlling the pulling parameters to obtain the final fiber shape we desire. The CO_2 laser is used for several reasons: the nominal emission wavelength of the laser approximates the resonant frequency of the SiO_2 lattice in glass. Thus, quartz and other conventional glasses can be melted when the appropriate laser power is supplied; then, the laser heat is clean and leaves no metal residue on the fiber as do conventional heating filaments; moreover the laser heat can be turned off instantly, leaving no residual filament heat [27].

Figure 5.36: The laser-based micropipette puller, model P-2000 produced by SUTTER INSTRUMENTS that I used for the fiber preparation.

There where five parameters we could play with to modify the final shape of the fiber:

1. The **HEAT** specifies the output power of the laser, and consequently the amount of energy supplied to the glass.

2. The **FILAMENT** specifies the scanning pattern of the laser beam that is used to supply HEAT to the glass.

3. The **VELOCITY** parameter specifies the velocity at which the puller bar must be moving before the hard pull is executed.

4. The **DELAY** parameter controls the timing of the start of the hard pull relative to the deactivation of the laser.

5. The **PULL** parameter controls the force of the hard pull.

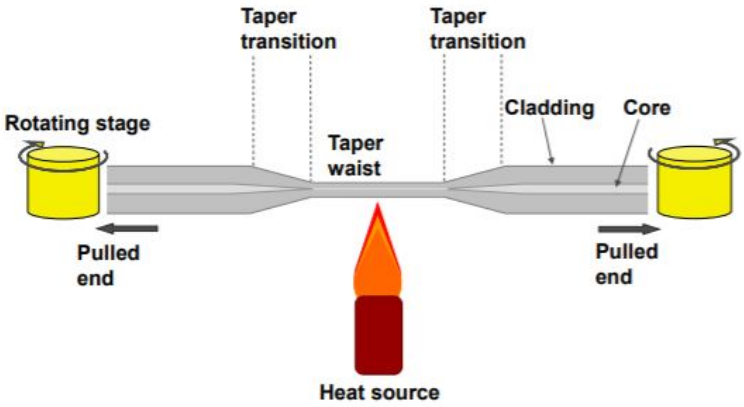

Figure 5.37: Schematic illustration of the flame (laser) approach used for the fabrication of tapered optical fibres. Figure extracted from [34].

In the next section we will present a set of pulled fiber I prepared to understand the process of optimization of the parameters to get to the desired fiber shape of 600nm and with a long tip [20].

Characterizaztion

With characterization of the pulled fiber shape we mean the final microscope check of the shape and the dimensions of the tip. By varying the heat parameter keeping fixed all the others we obtained the result shown in Fig. 5.38. The first white number is the heat parameter value, while the second one is the time in seconds necessary to complete the process. The lower the time the better the result [27]. In red the varied parameter and the scale. Since we obtained a narrow shape for a heat parameter value of 350, that was the one suggested by the user guide for the optical fibers we decided to use it for the next prepared fiber.

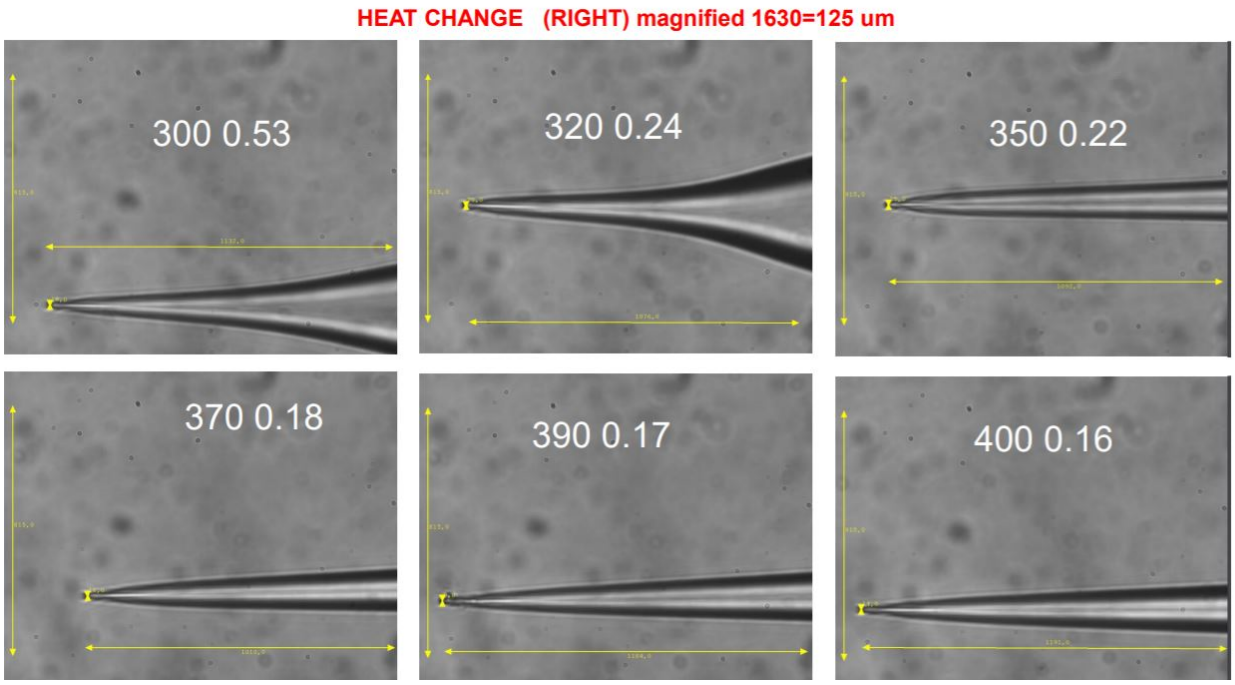

Figure 5.38: Shape of the fibers tip obtained by varying the heat parameter and keeping fixed the others. The best shape is obtained using a value of the parameter of 350.

Then we varied the pulling parameter value. The result are shown in Fig. 5.39. We observed that interesting results in terms of shape were obtained by the values 150 and 200 of the varied parameter.

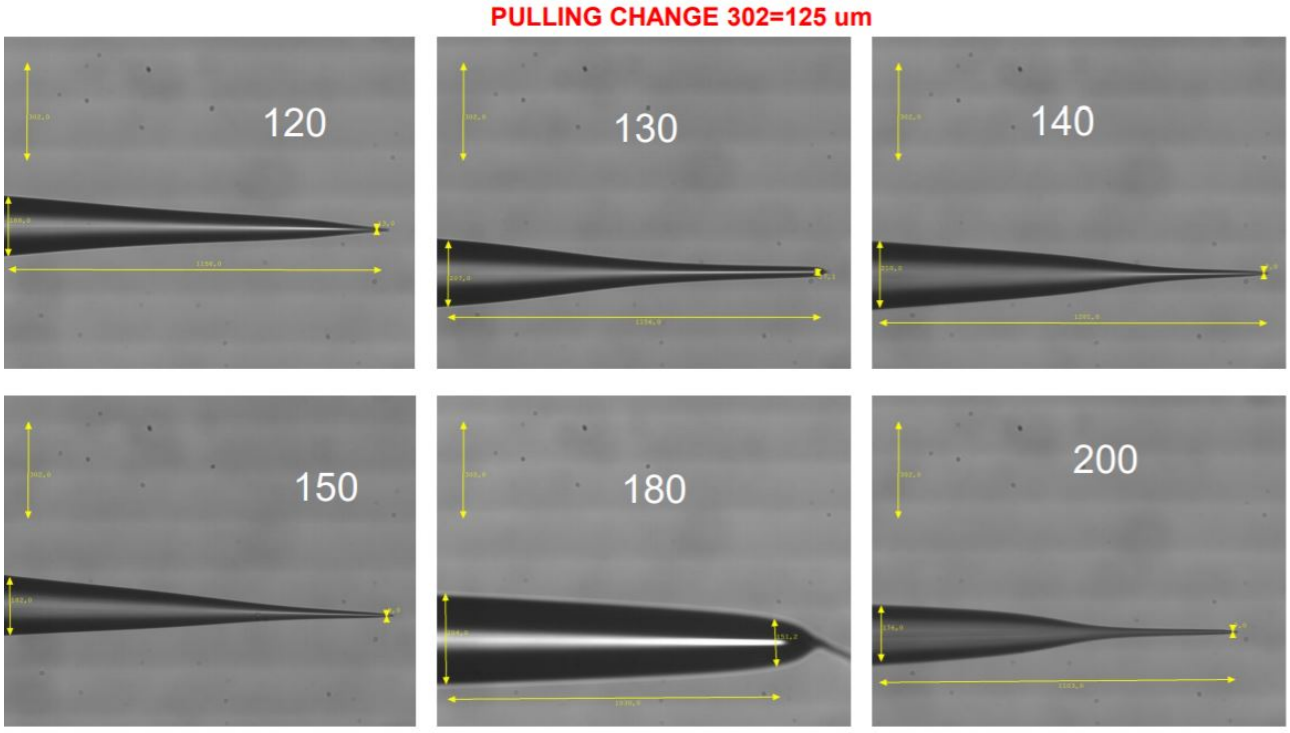

Figure 5.39: Shape of the fibers tip obtained by varying the pulling parameter and keeping fixed the others. The best shape is obtained using a value of the parameter of 150 or 200.

Now, increasing the magnification to a scale $1630 = 124\mu m$, we observed the 200 pulling

fiber and we measured a tip diameter of about $0.6\mu m$, , see Fig. 5.40.

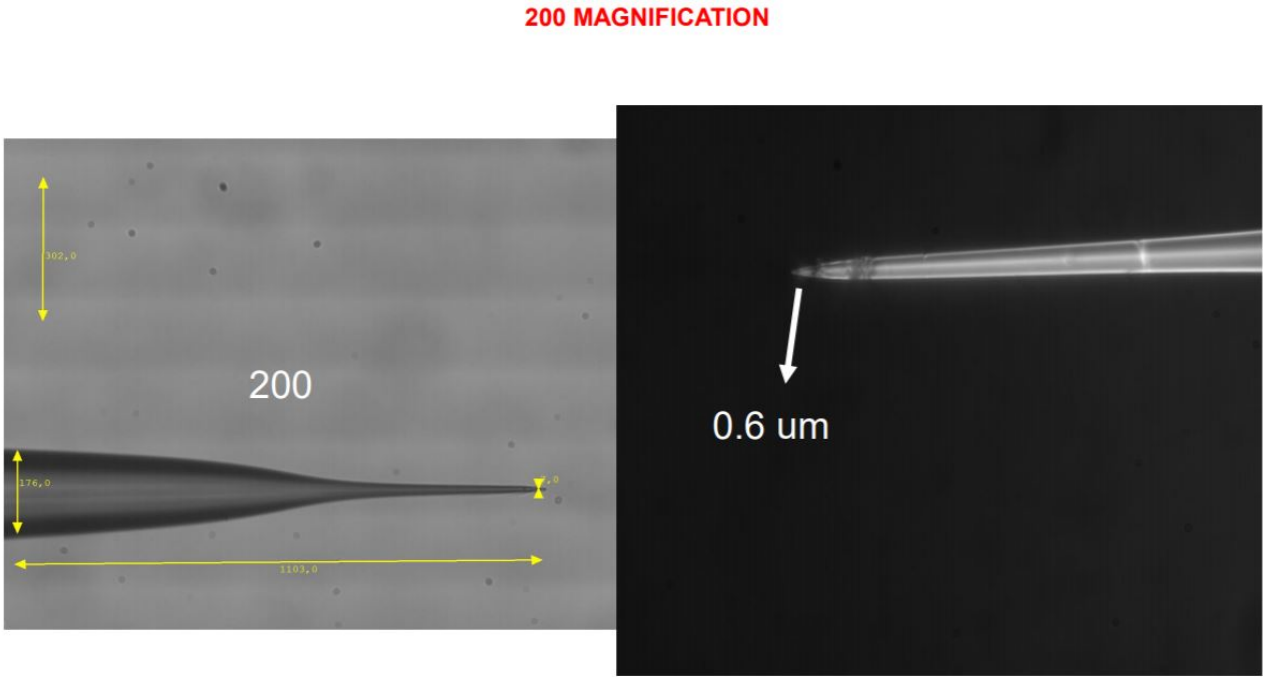

Figure 5.40: Magnification of the fiber shape obtained using 200 as the value of the pulling.

Then we varied the last parameter, the delay. We saw that for a lower value of the parameter we obtained a more narrow and small angles tapered fiber, as depicted in Fig. 5.41.

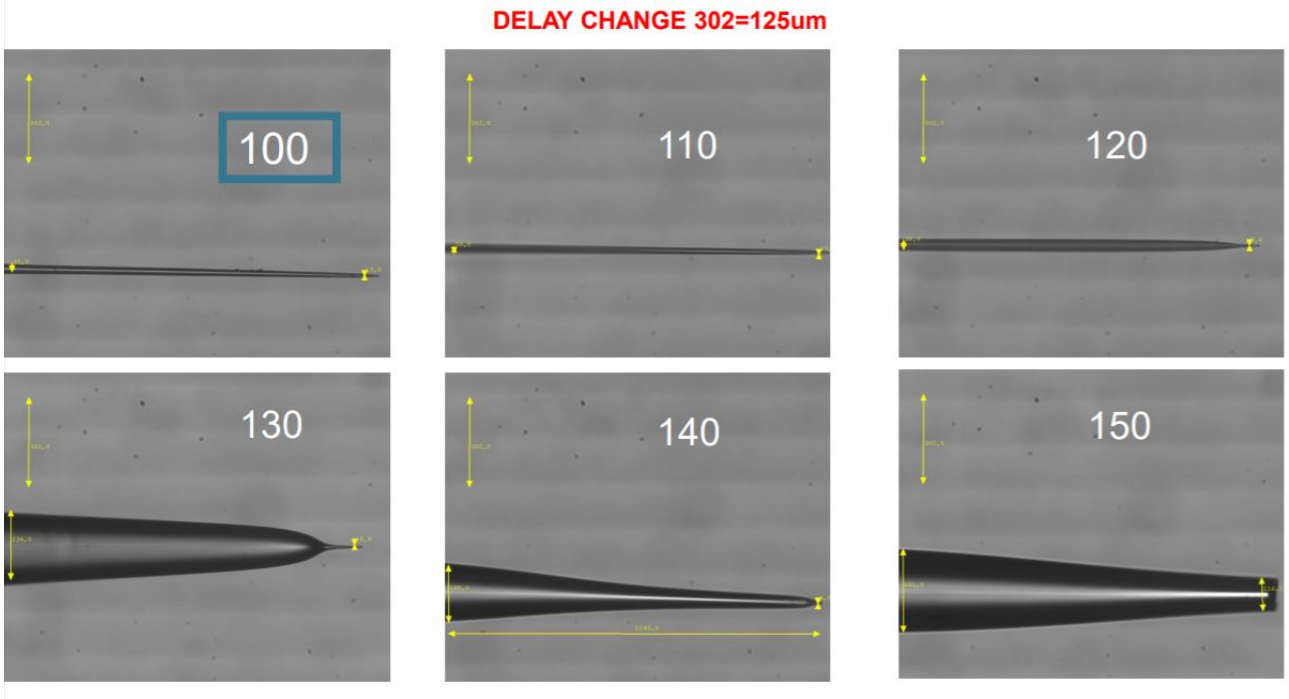

Figure 5.41: Shape of the fibers tip obtained by varying the delay parameter and keeping fixed the others. The best shape is obtained using a value of the parameter of 100.

We concluded with the analysis of the shape obtained by keeping fixed the heat(350), delay(100) and filament(0) parameters and varying the velocity and pulling one. The result is shown in Fig. 5.42.

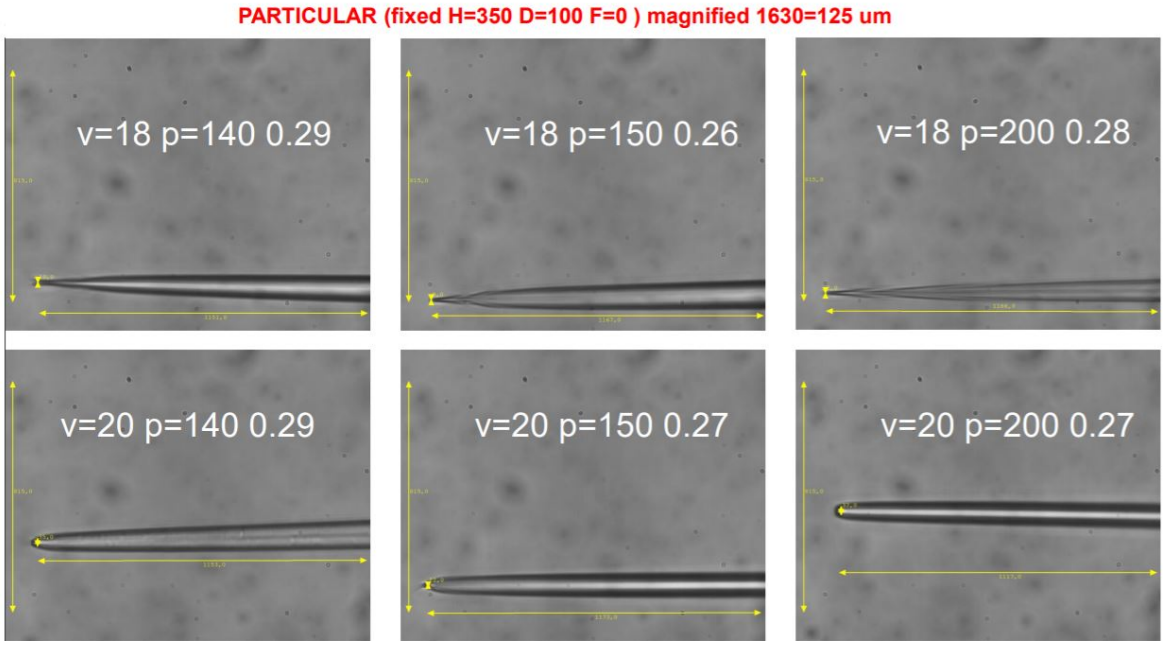

Figure 5.42: Shape of the fibers tip obtained by varying the velocity and pulling parameters while choosing the best parameters value we found for the others. The best shapes are obtained using a value of the pulling parameter of 150 and 18 for the velocity or 200 and 18.

In conclusion we could select two set of values of the parameters that enabled us to obtain the best fiber shape and a tapered diameter in the sub-wavelenght regime of about $0.6\mu m$. For the next prepared fiber we always used these values. The set of parameter values and the shape are presented in Fig. 5.43.

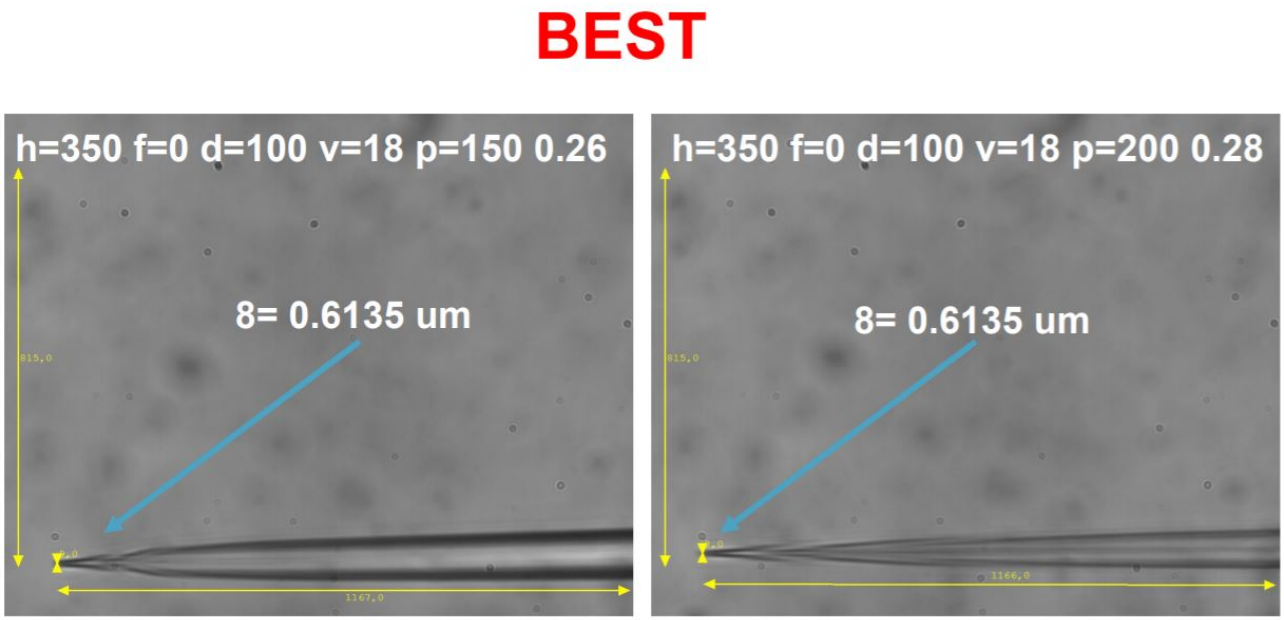

Figure 5.43: The picture of the best shapes we obtained. All the two set of parameters enabled us to obtain narrow tips with a final diameter of the desired value of $0.6\mu m$.

5.7 Fiber coupling and analysis

In this section it will be shown how we have implemented the setup for the collection of the signal through evanescent coupling to the nano optical fiber produced in the manner described above. Since the sample sizes are of the order of magnitude of a few tens of micrometers and the emitters in the nanometer scale, it was not possible to manually superimpose the fiber at the desired position on the sample. So, taking advantage of the large size of the cryostat, we inserted piezoelectrics to control respectively the movement of the sample and the fiber in all three directions with a sensitivity of less than a micrometer. This allowed us not only to center the fiber on the emitter but also to possibly move the fiber to the sample in search of higher optical quality emitters.

5.7.1 Fiber coupling dipole setup and results

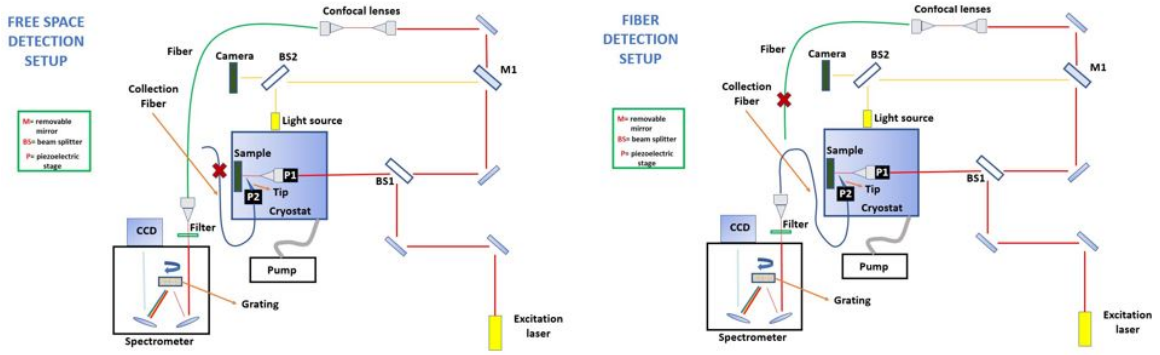

Figure 5.44: Schematic representation of the setup in free space collection (left) and fiber collection (right) configuration. The apparatus in fiber collection mode is the same as previously described for the micro-PL as regards the excitation part. The difference is in the collection. This time the signal is collected directly from the fiber and brought to the spectrometer after filtering it.

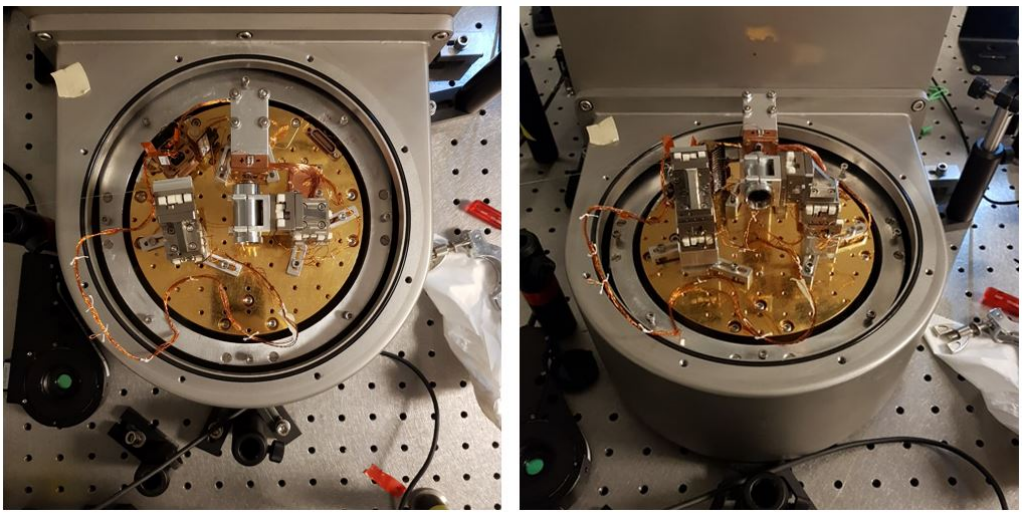

Figure 5.45: Here the internal arrangement of the components in the cryostat is shown. The piezoelectric on the left supports the tapered nanofiber. The piezoelectric closest to the reader supports the objective. The sample is the stage farthest from the reader.

The need to place technical elements such as piezoelectrics and nano fibers inside the cryostat required the use of a large cryostat that the laboratory was equipped with. The internal arrangement of the components is shown in Fig. 5.45. The photos represent the open cryostat in which the arrangement of the piezoelectrics is observed, used to control the position of the nano fiber and the laser spot over the sample with micrometric precision. The piezoelectric on the left supports the produced tapered nanofiber whose tip naturally faces the sample. The piezoelectric closest to the reader supports the objective that focuses the laser and collect the signal in free space mode. Finally, the stage farthest to the reader supports the sample. A schematic representation of the experimental setup for fiber collection is depicted in Fig. 5.44 as well as the comparison with the free space detection.The piezoelectric of the fiber could move independently in the three directions and therefore be easily arranged in the desired position. We tried to keep the back of the fiber raised with respect to the sample (therefore with the tip facing slightly towards the sample and not parallel) to avoid that the contact between the fiber and the sample could involuntarily generate an angle between the fiber and the sample such that the fiber is raised from the sample and this distance would prevent the evanescent field of the fiber from being in contact with the emitter. Fig. 5.46 shows, on the left, the nano optical fiber produced with the optimized parameters described in the previous chapter, on the right, instead, an image collected by the imaging system that shows the fiber just above the sample. It is possible to appreciate the thin tip of the fiber, with a diameter of about $0.4\mu m$ in this case, definitely smaller than the sample (about $60 \times 60\mu m$).

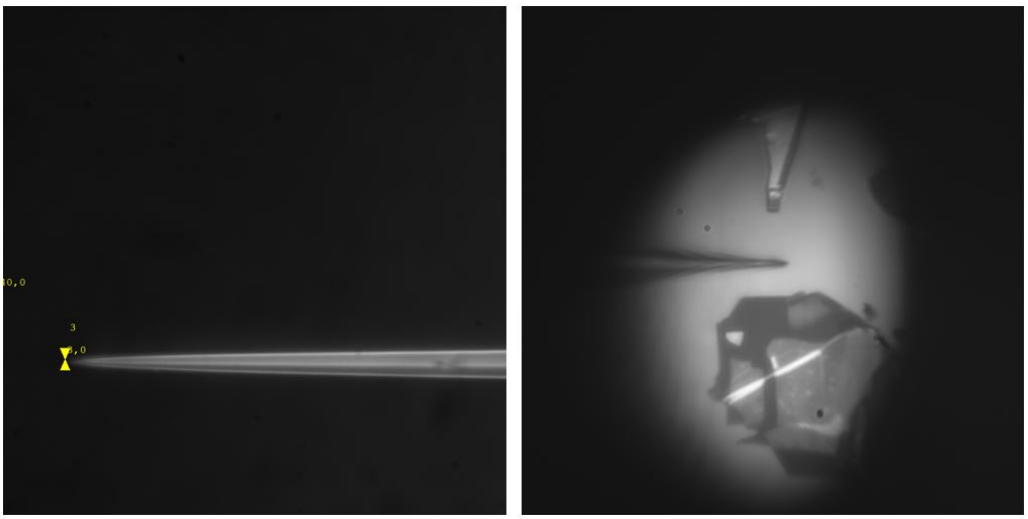

Figure 5.46: On the left, the nano optical fiber produced with the optimized parameters described in the previous chapter, on the right, instead, an image collected by the imaging system that shows the fiber just above the sample.

After having generated the vacuum and brought the system to 4K by liquid helium, everything is ready for optical measurements. Therefore we placed the fiber above the best signal found in the new sample.

5.7.2 Fiber collection

Now everything is ready to try the signal collection from the fiber. Showing the demonstration of the effective operation of such a collection setup would lay the foundations for the development of fiber photonic integrated circuits which are very advantageous in terms of product scalability and ease of use. Of course, the coupling efficiency is determined by the positioning of the fiber on the material. Therefore, after having selected the emitter, we tested the coupling for different positions of the fiber as shown in Fig. 5.47.

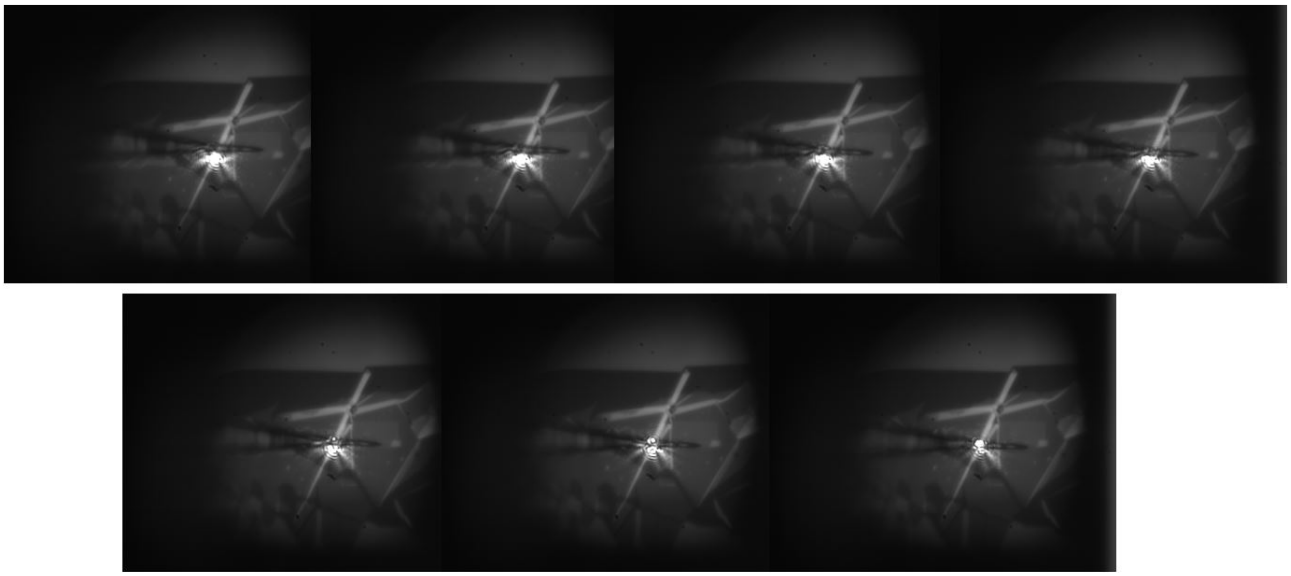

Figure 5.47: Images of the seven positions tested for coupling optimization. The best result was obtained for the positioning shown in the central image of the second line of images.

The respective collected spectra are represented in Fig. 5.48. First of all, the result of being able to collect from fiber is demonstrated. Furthermore, it can be noted that the coupling efficiency is highly dependent on the positioning of the fiber, this leaves open the possibility of not having perfectly centered the point of best coupling, we will try to address this problem in the next section.

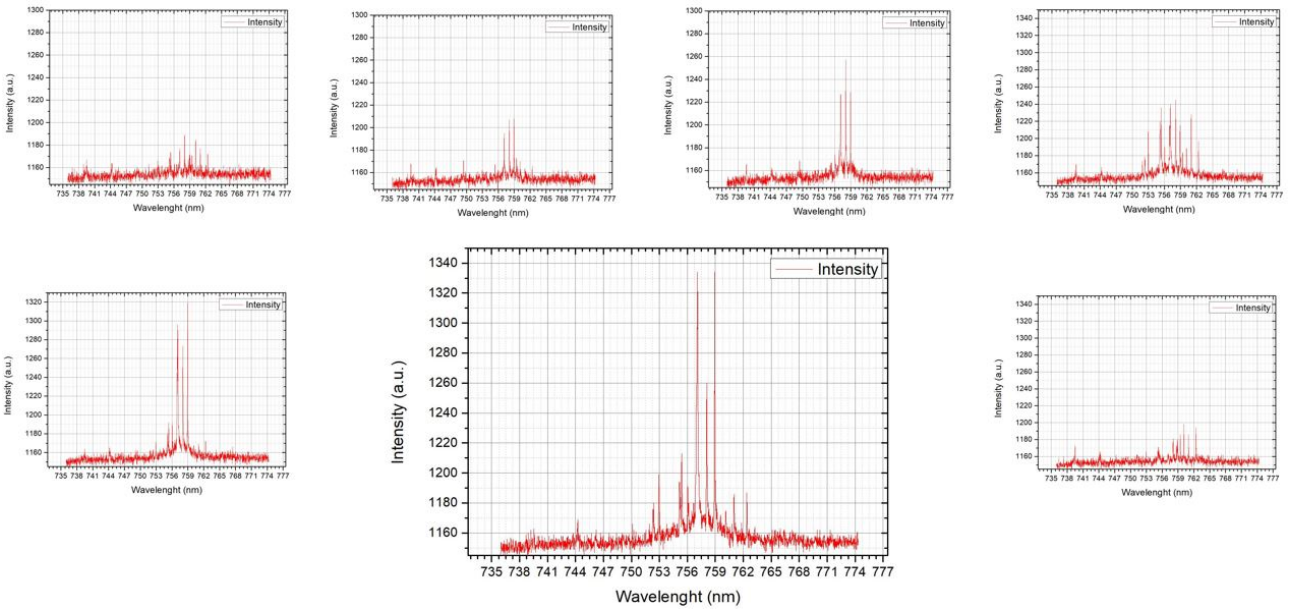

Figure 5.48: The relative seven spectra. The best one is the one magnified. The possibility to collect from fiber is then demonstrated.

Another important observation is that we note that the best coupling is not in the configuration in which the fiber is placed exactly above the laser spot but rather slightly to the side. This can be due to two main factors. First, the presence of the fiber along the optical path of the laser could slightly modify its trajectory and spread its intensity in a wider spot, thus reducing the optical signal that was previously optimized in the absence of the fiber. Also, one

cause of this could be a topological problem. The inhomogeneity of the sample could reduce the isotropy of the emitter radiation. We tested this last observation by choosing emitters in other positions on the sample observing the same behavior and therefore excluding this cause.

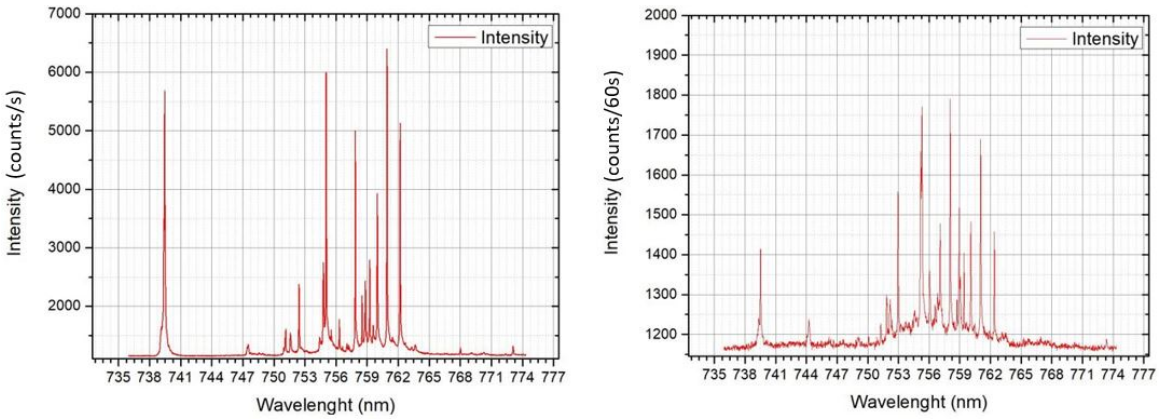

Figure 5.49: Comparison between the micro-PL signal measured for the same emitter in free space detection mode (left) and fiber collection mode (right) using the same laser power but respectively 1s and 60s of integration time. The possibility of collecting via fiber is demonstrated as well as the possibility of collecting the same spectrum.

In Fig. 5.49 we have compared the spectrum of the emitter obtained in free space configuration and the spectrum obtained through the fiber. Beyond the different detection efficiency, which can be improved with some tricks that we will show in the next section, we note how we were therefore able to collect exactly the same single emitter in free space configuration and in fiber coupling configuration. In fact, the slight differences in the spectra depend on the instability of the emitter itself, which we have seen to suffer from high charge effects that slightly modified the emission spectrum moment by moment.

5.7.3 Fiber excitation

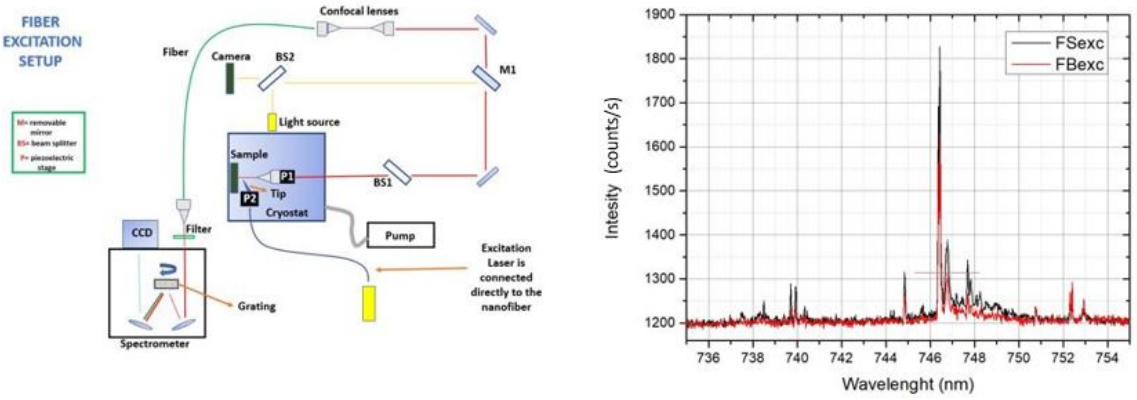

Figure 5.50: In the left picture the schematic representation of the setup for the fiber evanescent excitation free space collection configuration is shown. The apparatus in this mode is the same as previously described for the micro-PL as regards the collection part. The difference is in the excitation. This time the laser is evanescently brought to the sample directly from the fiber and the PL signal is then collected in the normal free space mode. In the right picture, the comparison between free space excitation (black line) and evanescent coupling through fiber (red) recorded for a quantum dot sample is shown. The fiber excitation reaches up to a 90% efficiency with respect to the free space excitation.

The optimal coupling for the collection with the fiber is verified in exactly the same maximum excitation configuration of an emitter through the evanescent wave of the fiber, thus in this way could be very easy to find the best coupling, in particular if exciting and collecting through the same fiber, that is possible exploiting a fiber beam splitter. The setup for the excitation via fiber is depicted in Fig. 5.50 (left). This time the laser is evanescently brought to the sample directly from the fiber and the PL signal is then collected in the normal free space mode. Indeed, the ability to excite with fiber has several advantages. As mentioned, since collection in free space is easier than that via fiber, it is much faster to optimize the coupling by trying to optimize the signal collected in free space. Furthermore, observing how the exciting laser propagates in the fiber and, in particular, observing where the evanescent field is visible, allowed us to verify that the tip of the fiber had no evanescent field and therefore highlighted some structural defects of the tip, perhaps slightly damaged by the continuous contact with the sample. Therefore we were forced to perform the coupling in a point of the fiber in which it had a larger diameter than expected and therefore a lower evanescent field, losing in efficiency. The next step will therefore certainly be the production of a new fiber. An example of fiber excitation is shown in Fig. 5.50 (right picture). In particular, it is the excitement of a quantum dot, which despite not being one of the samples on which my thesis is focused, I decided to include for two reasons. First of all, this spectrum demonstrates that we were able to couple the fiber to the quantum dots, showing their efficiency not only for 2D materials but also with quantum dots, thus expanding the field of application of such a setup. Furthermore, we note that the fiber excitation efficiency reaches 90% of the freespace excitation efficiency. In conclusion, we have thus shown that it is actually possible to stimulate and collect using the same fiber.

Part III

Conclusions

Conclusions

We will summarize here the experimental process followed and the most important results obtained as well as their outlooks in the integration with photonic circuits will be presented.

The experimental path followed was quite long and tortuous. No step was skipped as the thesis project started from the preparation of the materials in the clean room, passing from the simulation and preparation in the laboratory of the most suitable nanofiber up to the actual demonstration of the coupling with the nanofiber. In detail, the process followed was divided into these steps:

1. **Clean room preparation of WSe_2 samples encapsulated in hBN**: the preparation of the samples was one of the most crucial parts of the whole process. We have shown how the photoluminescence signal differs between the different samples. The second sample showed a hundred times higher signal than the first sample. For the fabrication of the samples, we used the mechanical exfoliation to arrive at the monolayer limit and an all-dry transfer method via PDMS to complete the hBN encapsulation.

2. **Optical characterization**: the micro photoluminescence experiments allowed us to demonstrate the transition from indirect band gap to direct band gap in monolayer regime as well as the comparison between the quality of the samples prepared in the clean room. Then we performed the measurement of the radiative lifetime and $g^{(2)}(\tau)$. All the results found were in agreement with the ones in literature.

3. **Nanofiber simulations and fabrication**: We performed the COMSOL and MATLAB simulation of the propagating modes in the tapered nanofiber to understand which shape and size were needed to obtain an evanescent wave large enough outside the tip of the fiber to enable the coupling. Then, we moved on to the production of tapered nanofibers. By varying different parameters and producing different sets of fibers we were able to find the optimized parameters to produce nanofibers of the desired size.

4. **Fiber coupling**: We finally proved that the fiber collected signal was clear and the procedure was well reproducible. Finally, we also demonstrated the possibility of excitation via fiber.

Through a more accurate preparation of the WSe_2 monolayers in the clean room we were able to pass from an average signal intensity PL for the different emitters analyzed of 150 counts/s to an average intensity of 10000 counts/s in sample 2, increasing the signal by 100 times. We measured the T_1 for some emitter chosen in sample 1 and sample 2. In sample 1, we measured the T_1 of three emitters, respectively, $27.7 \pm 0.9ns$, $12.2 \pm 0.8ns$ and $12.1 \pm 0.3ns$. We measured the T_1 for an emitter in sample 2, finding $5.2 \pm 0.9ns$. The difference between the lifetimes of sample 1 and sample 2 is compatible with the presence of very different strains in the two samples. We expect a shorter the lifetime for a stronger confinement. For a weak confinement, on the other hand, there is a small overlap of the wave function of the electron and that of the hole and therefore a longer lifetime. The strenght of the confinement can

result from clean room manufacturing or local inhomogeneity of the samples. For the emitter with $T_1 = 5.2 \pm 0.9ns$ in sample 2 we performed a PLE measurement and we highlighted a resonance of the PL signal for an excitation wavelength of 727.7nm. We therefore used this value for the subsequent measurements. On the same emitter we measured the $g^{(2)}(\tau)$, using both the mode-locked Ti-Sa laser in pulsed mode and in CW. Through the measurement of $g^{(2)}(\tau)$ in pulsed mode we could prove qualitatively the single photon source nature of the emitter by observing a drop in counts for a delay value of 0. From the measurement of $g^{(2)}(\tau)$ in CW mode, instead, we extract the exact value of the $g^{(2)}(0)$, i.e. $0.21 \pm 0.02ns$. We have therefore quantitatively demonstrated that localized defect-bound excitons in WSe_2 monolayers are single photon sources. Regarding the preparation of the nanofiber, through COMSOL and MATLAB simulations we found that a size of 0.6 um was right to have a sufficiently intense evanescent field to allow coupling to the emitter. We managed, through several repetitions, to produce autonomously the nanofiber of the desired size. Through the use of piezoelectric stages, we developed a setup that allowed us to have total and independent control of the positioning of the fiber on the sample and of the excitation laser, with a precision below the micrometer. Finally we were able to demonstrate the feasibility of the evanescent coupling of the emission to the fiber from a chosen localized defect-bound exciton. We were also able to demonstrate how the fiber collection setup can also be used for sample excitation. This also opens the way to use it simultaneously in excitation and collection through an additional fibered-beam splitter. Our next efforts will be focused on improving the coupling efficiency. New fibers will be produced whereby we expect the coupling to take place in the thinnest part of the fiber tip, that is where the evanescent field is most intense. Furthermore, we will try to deposit the flakes directly on the nanofiber so that the strain induced defects [35] are observed, by construction, in the vicinity of the tip and thus increasing the coupling efficiency. The results found during this project have interesting applications in the field of nano-photonics for the design of all integrated single-photon devices, we will see this, briefly, in the outlooks section.

Outlooks

The knowledge advances in atomically thin two-dimensional TMDs have led to a variety of promising technologies for nanoelectronics, photonics, sensing, energy storage, and optoelectronics [9] as well as the applications of in the field of biomedicine, including drug loading, photothermal therapy, biological imaging and biosensor [75]. In this thesis project we have dealt with the photoemission from excitons that are spatially localized by defects in two-dimensional WSe_2 monolayers. We have proven them to be source of single photons. Single quantum emitters (SQEs) are at the heart of modern quantum optics and photonic quantum information technologies. In addition to their fundamental importance, establishing new SQEs in 2D quantum materials could give rise to practical advantages in quantum information processing, such as efficient photon extraction and high integratability and scalability [24]. Traditional solid-state emitters are typically embedded in three-dimensional materials with high-refractive index, which usually limits the integratability and the photon extraction efficiency. Whereas, the 2D geometry of a SQE confined to an atomically thin material can in principle greatly enhance the photon extraction efficiency, potentially allowing for simplified integration with photonic circuits [24]. The localized defect-bound exciton emitters we found through the PL measurements have a narrow emission linewidth and they are very bright. However, in order to employ these emitters in applications, e.g., as single photon sources, it is necessary to efficiently extract the emitted photons. While usage of solid immersion lenses and dielectric antennas has been demonstrated, these approaches do not offer a path to scalability and suffer from complicated output modes [62]. A promising direction to overcome this problem could be using our setup. The evanescent coupling to tapered optical fibers, where the photons get directly

emitted into a guided mode inside the fiber, could provide, in theory, coupling efficiencies of over 20% and even higher efficiencies are possible by combining the tapered fibers with optical cavities, such as nanofiber Bragg cavities (NFBCs) [62]. The realization of integrated photonic circuits on a single chip requires controlled manipulation and integration of solid-state quantum emitters with nanophotonic components. The coupling to the tapered fiber allowed the excitation and detection in a fully fiber coupled way yielding a true integrated system [62]. Our results provide evidence of the feasibility to integrate quantum emitters in 2D materials with photonic structures. This shows that, increasing the coupling efficiency by producing new fibers, the new setup could play the same role as a high NA objective lens setup, while having the advantage of being directly fiber coupled and, thus, offering an alignment free collection. Furthermore, our setup does not require the deposit of the material directly on the tapered waist of the fiber, as proposed in [62] or [38], instead, it leaves us the freedom to move the fiber freely. This allows for a lighter setup since multiple samples can be analyzed at a time without having to deposit the sample on the nanofiber each time. Furthermore, by moving the fiber over the sample one can optimize the coupling quickly without having to move the whole sample, losing the signal. In conclusion, we realized a concept of an integrated photonic system where a localized defect-bound exciton in 2D layered WSe_2 monolayer is coupled to a tapered optical fiber. Our results could pave the way for promising applications in integrated quantum photonics using single quantum emitters in WSe_2.

Part IV

Appendix

5.8 Appendix A: saturation intensity for a 2-level system

In this section we will explain the model used for the saturation of the micro photoluminescence signal for the localized excitons bound to the defects. The intensity saturation emerges spontaneously from the 2-level nature of a system. This is the case for our excitons. To develop the accounts we will follow the discussion developed in [47]. In general, there are infinitely many energy eigenstates in an atomic, molecular or solid-state medium and the spectral lines are associated with allowed transitions between two of these energy eigenstates. For many physical considerations it is already sufficient to take only two of these possible energy eigenstates into account, for example those which are related to the transition from the ground state to an excited state. The resulting simple model is often called a two-level system i.e. it has two energy levels and energy eigenstates. The interaction of the two-level system with the electric field of an excitation electromagnetic wave is described by the Bloch equations. They will not be derived here but they will be used as a starting point to obtain the saturation intensity.

5.8.1 The two-level system model

A system with only two energy eigenvalues is described by a two-dimensional state space spanned by the two energy eigenstates $|e\rangle$ and $|g\rangle$ to constitute a complete orthonormal system. The corresponding energy eigenvalues are E_e and E_g, see Fig. 5.51

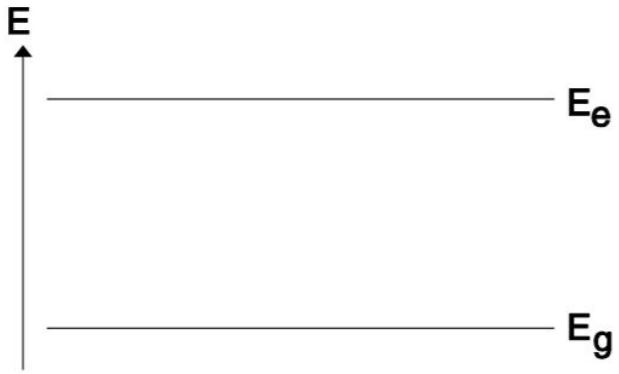

Figure 5.51: A schematic representation of a two-level system. E_e corresponds to the excited state while E_g to the ground state. Figure extracted from [47].

In the position-representation, these states correspond to the wave functions [47]

$$\psi_g(x) = \langle x \mid g\rangle, \quad \text{and} \quad \psi_e(x) = \langle x \mid e\rangle \tag{5.1}$$

The Hamiltonian operator of the two-level atom is in the energy representation [47]

$$\mathbf{H}_A = E_e|e\rangle \langle e| + E_g|e\rangle \langle g| \tag{5.2}$$

In this two-dimensional state space only four linearly independent linear operators are possible. A possible base choice is

$$\begin{aligned} \mathbf{1} &= |e\rangle\langle e| + |g\rangle\langle g| \\ \boldsymbol{\sigma}_z &= |e\rangle\langle e| - |g\rangle\langle g| \\ \boldsymbol{\sigma}^+ &= |e\rangle\langle g| \\ \boldsymbol{\sigma}^- &= |e\rangle\langle e| \end{aligned} \tag{5.3}$$

To understand the physical meaning of these operators we apply them to an arbitrary state

$$|\psi\rangle = c_g|g\rangle + c_e|e\rangle \tag{5.4}$$

to obtain [47]

$$\begin{aligned}\boldsymbol{\sigma}^+|\psi\rangle &= c_g|e\rangle \\ \boldsymbol{\sigma}^-|\psi\rangle &= c_e|g\rangle \\ \boldsymbol{\sigma}_z|\psi\rangle &= c_e|e\rangle - c_g|g\rangle\end{aligned} \tag{5.5}$$

The operator σ^+ generates a transition from the ground to the excited state, and σ^- does the opposite. In contrast to σ^+ and σ^-, σ_z is a Hermitian operator, and its expectation value is an observable physical quantity with expectation value [47]

$$\langle\psi\,|\boldsymbol{\sigma}_z|\,\psi\rangle = |c_e|^2 - |c_g|^2 = w \tag{5.6}$$

the inversion w of the system, since $|c_e|^2$ and $|c_g|^2$ are the probabilities for finding the atom in state $|e\rangle$ or $|g\rangle$ upon a corresponding measurement. If we separate from the Hamiltonian (6.3) the term $(E_e + E_g)/2 \cdot \mathbf{1}$, where $\mathbf{1}$ denotes the unity matrix, we rescale the energy values correspondingly and obtain for the Hamiltonian of the two-level system

$$\mathbf{H}_A = \frac{1}{2}\hbar\omega_{eg}\boldsymbol{\sigma}_z \tag{5.7}$$

where

$$\omega_{eg} = \frac{1}{\hbar}(E_e - E_g) \tag{5.8}$$

is the transition frequency.

5.8.2 Bloch equations

If there is a coherent time armonic additional field in addition,

$$\vec{E}(\vec{x}_A, t) = \frac{1}{2}\left(\underline{E}_0 e^{\mathrm{j}\omega t}\vec{e}_p + \underline{E}_0^* e^{-\mathrm{j}\omega t}\vec{e}_p^*\right) \tag{5.9}$$

where, $\vec{e}_p$ is the polarization vector of the excitation wave and $\underline{E}_0$ denotes the complex electric field amplitude at the position of the system (labelled A), the Hamiltonian has to be extended by the dipole interaction with that field,

$$\mathbf{H}_E = -\overrightarrow{\mathbf{d}}\cdot\vec{E}(\vec{x}_A, t) \tag{5.10}$$

Thus, the total dynamics of the two-level system including the pumping and dephasing processes, not derived here, is given by [47]

$$\begin{aligned}\dot{d} &= -\left(\frac{1}{T_2} - \mathrm{j}\omega_{eg}\right)d + \mathrm{j}\Omega_r^*\mathrm{j}^{\mathrm{j}\omega t}w \\ \dot{w} &= -\frac{w - w_0}{T_1} + 2\mathrm{j}\Omega_r e^{-\mathrm{j}\omega t}d - 2\mathrm{j}\Omega_r^* e^{\mathrm{j}\omega t}d^*\end{aligned} \tag{5.11}$$

where

- d is the dipole moment.
- w is the inversion.
- w_0 is the equilibrium inversion.
- Ω_r is the Rabi oscillations-frequency
- T_1 and T_2 denote, respectively, the energy relaxation (radiative lifetime) and the phase relaxation time constants.

These equations are called the Bloch Equations. They describe the whole dynamics of a statistical ensemble of two-level atoms interacting with a classical electric field.

5.8.3 Saturation

We have assumed that the external field is time harmonic. The Bloch Equations are nonlinear. However, for moderate field intensities, i.e. the magnitude of the Rabi-frequency is much smaller than the optical frequency, $|\Omega_r| << \omega$, the inversion does not change much within an optical cycle of the field. We assume that the inversion w of the system will only be slowly changing and it settles down to a steady state value w_s. If the inversion can be assumed time independent, $w = w_s$ the equation for the dipole moment is linear and the dipole moment will oscillate with the same frequency as the driving field

$$\underline{d} = \underline{d}_0 e^{\mathrm{j}\omega t} \tag{5.12}$$

Then, two solutions for the dipole amplitude and the steady state inversion are [47]:

$$\begin{aligned} \underline{d}_0 &= \frac{\mathrm{j}}{2\hbar} \frac{\left(\vec{M}^* \cdot \vec{e}_p\right) w_s}{1/T_2 + \mathrm{j}\left(\omega - \omega_{eg}\right)} \underline{E}_0 \\ w_s &= \frac{w_0}{1 + \frac{T_1}{\hbar^2} \frac{1/T_2 \left|\vec{M}^* \cdot \vec{e}_p\right|^2}{(1/T_2)^2 + (\omega_{eg} - \omega)^2} \left|\underline{E}_0\right|^2}. \end{aligned} \tag{5.13}$$

where $\vec{M}$ is the dipole matrix and $\vec{e}_p$ is the polarization vector of the excitation wave. Introducing the normalized lineshape function, which is in this case a Lorentzian,

$$L(\omega) = \frac{(1/T_2)^2}{(1/T_2)^2 + (\omega_{eg} - \omega)^2} \tag{5.14}$$

it is possible to show that [47]

$$w_s = \frac{w_0}{1 + \frac{I}{I_s} L(\omega)} \tag{5.15}$$

Thus the stationary inversion depends on the intensity of the incident light. Therefore, w_0 is called the unsaturated inversion, w_s the saturated inversion and I_s, with

$$I_s = \left[\frac{2T_1 T_2 Z_F}{\hbar^2} \left|\vec{M}^* \cdot \vec{e}_p\right|^2\right]^{-1} \tag{5.16}$$

is the saturation intensity. This is the expression of the saturation intensity of the photoluminescence signal measured during the experiments. To conclude, we can point out that in many cases the fastest process in the system-field interaction dynamics is the dephasing of the dipole moment, i. e. $T_2 \to 0$ [47]. In this limit the Bloch Equations became simple rate equations and we only take care of the counting of population differences due to spontaneous and stimulated emissions. Under this assumption, it can be shown that the saturation intensity can be linked to the interaction cross section through the relation [47]:

$$\sigma = \frac{\hbar \omega_{eg}}{T_1 I_s} \tag{5.17}$$

Bibliography

[1] Satish Addanki, I Sadegh Amiri, and P Yupapin. "Review of optical fibers-introduction and applications in fiber lasers". In: *Results in Physics* 10 (2018), pp. 743–750.

[2] Sabrine Ayari et al. "Radiative lifetime of localized excitons in transition-metal dichalcogenides". In: *Physical Review B* 98.20 (2018), p. 205430.

[3] Gordon Baym. "The physics of Hanbury Brown–Twiss intensity interferometry: from stars to nuclear collisions". In: *arXiv preprint nucl-th/9804026* (1998).

[4] R Hanbury Brown and Richard Q Twiss. "Correlation between photons in two coherent beams of light". In: *Nature* 177.4497 (1956), pp. 27–29.

[5] F Cadiz et al. "Excitonic linewidth approaching the homogeneous limit in MoS 2-based van der Waals heterostructures". In: *Physical Review X* 7.2 (2017), p. 021026.

[6] Fabian Cadiz et al. "Ultra-low power threshold for laser induced changes in optical properties of 2D molybdenum dichalcogenides". In: *2D Materials* 3.4 (2016), p. 045008.

[7] Andres Castellanos-Gomez et al. "Deterministic transfer of two-dimensional materials by all-dry viscoelastic stamping". In: *2D Materials* 1.1 (2014), p. 011002.

[8] Chin-Lin Chen. *Foundations for guided-wave optics*. John Wiley & Sons, 2006.

[9] Wonbong Choi et al. "Recent development of two-dimensional transition metal dichalcogenides and their applications". In: *Materials Today* 20.3 (2017), pp. 116–130.

[10] COMSOL. *Perfectly matched layer*. `https://www.comsol.com/blogs/using-perfectly-matched-layers-and-scattering-boundary-conditions-for-wave-electromagnetics-problems/`. 2016.

[11] Chandriker Kavir Dass et al. "Ultra-Long Lifetimes of Single Quantum Emitters in Monolayer WSe2/hBN Heterostructures". In: *Advanced Quantum Technologies* 2.5-6 (2019), p. 1900022.

[12] Cory R Dean et al. "Boron nitride substrates for high-quality graphene electronics". In: *Nature nanotechnology* 5.10 (2010), pp. 722–726.

[13] Paul Adrien Maurice Dirac. *The principles of quantum mechanics*. 27. Oxford university press, 1981.

[14] RP photonics encyclopedia. *Avalanche photodiodes*. `https://www.rp-photonics.com/avalanche_photodiodes.html?s=ak`. 2020.

[15] Hui Fang et al. "Strong interlayer coupling in van der Waals heterostructures built from single-layer chalcogenides". In: *Proceedings of the National Academy of Sciences* 111.17 (2014), pp. 6198–6202.

[16] Ugo Fano. "Quantum theory of interference effects in the mixing of light from phase-independent sources". In: *American Journal of Physics* 29.8 (1961), pp. 539–545.

[17] Richard P Feynman. "There's plenty of room at the bottom". In: *California Institute of Technology, Engineering and Science magazine* (1960).

[18] Alexander J Fielding and Christopher C Davis. "Tapered single-mode optical fiber evanescent coupling". In: *IEEE Photonics Technology Letters* 14.1 (2002), pp. 53–55.

[19] Mark Fox. *Quantum optics: an introduction*. Vol. 15. OUP Oxford, 2006.

[20] R Garcia-Fernandez et al. "Optical nanofibers and spectroscopy". In: *Applied Physics B* 105.1 (2011), p. 3.

[21] Nicolas Gisin et al. "Quantum cryptography". In: *Reviews of modern physics* 74.1 (2002), p. 145.

[22] JW Goodman. "Statistical Optics, 286–360 Wiley". In: *New York* (1985).

[23] Peter Grünwald. "Effective second-order correlation function and single-photon detection". In: *New Journal of Physics* 21.9 (2019), p. 093003.

[24] Yu-Ming He et al. "Single quantum emitters in monolayer semiconductors". In: *Nature nanotechnology* 10.6 (2015), pp. 497–502.

[25] Oliver Iff et al. "Deterministic coupling of quantum emitters in WSe 2 monolayers to plasmonic nanocavities". In: *Optics Express* 26.20 (2018), pp. 25944–25951.

[26] Koji Igarashi et al. "Performance evaluation of selective mode conversion based on phase plates for a 10-mode fiber". In: *Optics express* 22.17 (2014), pp. 20881–20893.

[27] SUTTER INSTRUMENTS. *Micropipette puller, P-2000*. `https://www.sutter.com/MICROPIPETTE/p-2000.html`. 2014.

[28] K Karapetyan et al. *Optical fibre toolbox for MATLAB*. 2010.

[29] G Kioseoglou et al. "Valley polarization and intervalley scattering in monolayer MoS2". In: *Applied Physics Letters* 101.22 (2012), p. 221907.

[30] Claus F Klingshirn. *Semiconductor optics*. Springer Science & Business Media, 2012.

[31] Pieter Kok et al. "Linear optical quantum computing with photonic qubits". In: *Reviews of Modern Physics* 79.1 (2007), p. 135.

[32] Andor Kormányos et al. "k· p theory for two-dimensional transition metal dichalcogenide semiconductors". In: *2D Materials* 2.2 (2015), p. 022001.

[33] Tobias Korn et al. "Low-temperature photocarrier dynamics in monolayer MoS2". In: *Applied Physics Letters* 99.10 (2011), p. 102109.

[34] Sergiy Korposh et al. "Tapered optical fibre sensors: Current trends and future perspectives". In: *Sensors* 19.10 (2019), p. 2294.

[35] Santosh Kumar, Artur Kaczmarczyk, and Brian D Gerardot. "Strain-induced spatial and spectral isolation of quantum emitters in mono-and bilayer WSe2". In: *Nano letters* 15.11 (2015), pp. 7567–7573.

[36] Angela Leung, P Mohana Shankar, and Raj Mutharasan. "A review of fiber-optic biosensors". In: *Sensors and Actuators B: Chemical* 125.2 (2007), pp. 688–703.

[37] Hai Li et al. "Preparation and applications of mechanically exfoliated single-layer and multilayer MoS2 and WSe2 nanosheets". In: *Accounts of chemical research* 47.4 (2014), pp. 1067–1075.

[38] Lars Liebermeister et al. "Tapered fiber coupling of single photons emitted by a deterministically positioned single nitrogen vacancy center". In: *Applied Physics Letters* 104.3 (2014), p. 031101.

[39] Lukas Linhart et al. "Localized intervalley defect excitons as single-photon emitters in WSe 2". In: *Physical Review Letters* 123.14 (2019), p. 146401.

[40] Rodney Loudon. *The quantum theory of light*. OUP Oxford, 2000.

[41] Yue Luo et al. "Single photon emission in WSe2 up 160 K by quantum yield control". In: *2D Materials* 6.3 (2019), p. 035017.

[42] Ruitao Lv et al. "Two-dimensional transition metal dichalcogenides: Clusters, ribbons, sheets and more". In: *Nano Today* 10.5 (2015), pp. 559–592.

[43] Kin Fai Mak et al. "Atomically thin MoS 2: a new direct-gap semiconductor". In: *Physical review letters* 105.13 (2010), p. 136805.

[44] Marco Manca. "Study of the optoelectronic properties of atomically thin WSe2". PhD thesis. INSA de Toulouse, 2019.

[45] Hanne-Torill Mevik. "Coherence in Classical Electromagnetism and Quantum Optics". MA thesis. 2009.

[46] GJ Milburn. "Photons as qubits". In: *Physica Scripta* 2009.T137 (2009), p. 014003.

[47] MIT. *Interaction of Light and Matter*. `https://ocw.mit.edu/courses/electrical-engineering-and-computer-science/6-974-fundamentals-of-photonics-quantum-electronics-spring-2006/lecture-notes/chapter6.pdf`. 2017.

[48] Galan Moody et al. "Intrinsic homogeneous linewidth and broadening mechanisms of excitons in monolayer transition metal dichalcogenides". In: *Nature communications* 6.1 (2015), pp. 1–6.

[49] Thomas Mueller and Ermin Malic. "Exciton physics and device application of two-dimensional transition metal dichalcogenide semiconductors". In: *npj 2D Materials and Applications* 2.1 (2018), pp. 1–12.

[50] Ruaa Khalil Musa, Salah Al deen Adnan, and Ali Mahdi Hammadi. "Design and fabrication of evanescent wavefiber optic sensor". In: *Advances in Natural and Applied Sciences* 11.4 (2017), pp. 130–140.

[51] Azo Nano. *Applications of Cathodoluminescence g(2) Imaging*. `https://www.azonano.com/article.aspx?ArticleID=5073`. 2018.

[52] KS Novoselov and AH Castro Neto. "Two-dimensional crystals-based heterostructures: materials with tailored properties". In: *Physica Scripta* 2012.T146 (2012), p. 014006.

[53] KS Novoselov et al. "2D materials and van der Waals heterostructures". In: *Science* 353.6298 (2016), aac9439.

[54] PicoQuant. *Antibunching*. `https://www.picoquant.com/applications/category/metrology/antibunching`. May 2018.

[55] Ashwin Ramasubramaniam. "Large excitonic effects in monolayers of molybdenum and tungsten dichalcogenides". In: *Physical Review B* 86.11 (2012), p. 115409.

[56] Michael E Reimer and Catherine Cher. "The quest for a perfect single-photon source". In: *Nature Photonics* 13.11 (2019), pp. 734–736.

[57] Daniel Rhodes et al. "Disorder in van der Waals heterostructures of 2D materials". In: *Nature materials* 18.6 (2019), p. 541.

[58] Sarah Saint-Jalm. *Sources optiques fibrées solitoniques pour la spectroscopie et la microscopie non linéaires*. `http://www.theses.fr/2014AIXM4353`. 2014.

[59] S Saint-Jaml. "Soliton-based fiber light sources for nonlinear spectroscopy and microscopy". PhD thesis. PhD dissertation, Aix Marseille University, 2014.

[60] K Santoro and C Ricciardi. "Biosensors". In: (2016).

[61] John R Schaibley et al. "Valleytronics in 2D materials". In: *Nature Reviews Materials* 1.11 (2016), pp. 1–15.

[62] Andreas W Schell et al. "Coupling quantum emitters in 2D materials with tapered fibers". In: *ACS Photonics* 4.4 (2017), pp. 761–767.

[63] Pablo Solano et al. "Optical nanofibers: a new platform for quantum optics". In: *Advances In Atomic, Molecular, and Optical Physics*. Vol. 66. Elsevier, 2017, pp. 439–505.

[64] Andrea Splendiani et al. "Emerging photoluminescence in monolayer MoS2". In: *Nano letters* 10.4 (2010), pp. 1271–1275.

[65] Malvin Carl Teich. *Fundamentals of photonics [electronic resource]*. Wiley, 1991.

[66] Sefaattin Tongay et al. "Defects activated photoluminescence in two-dimensional semiconductors: interplay between bound, charged and free excitons". In: *Scientific reports* 3.1 (2013), pp. 1–5.

[67] Milos Toth and Igor Aharonovich. "Single photon sources in atomically thin materials". In: *Annual review of physical chemistry* 70 (2019), pp. 123–142.

[68] Gang Wang et al. "Colloquium: Excitons in atomically thin transition metal dichalcogenides". In: *Reviews of Modern Physics* 90.2 (2018), p. 021001.

[69] Gang Wang et al. "Giant enhancement of the optical second-harmonic emission of WSe 2 monolayers by laser excitation at exciton resonances". In: *Physical review letters* 114.9 (2015), p. 097403.

[70] Qing Hua Wang et al. "Electronics and optoelectronics of two-dimensional transition metal dichalcogenides". In: *Nature nanotechnology* 7.11 (2012), p. 699.

[71] Jakob Wierzbowski et al. "Direct exciton emission from atomically thin transition metal dichalcogenide heterostructures near the lifetime limit". In: *Scientific reports* 7.1 (2017), pp. 1–6.

[72] Wikipedia. *Hanbury Brown and Twiss effect*. `https://en.wikipedia.org/wiki/Hanbury_Brown_and_Twiss_effect`. 2020.

[73] Wang Yao, Di Xiao, and Qian Niu. "Valley-dependent optoelectronics from inversion symmetry breaking". In: *Physical Review B* 77.23 (2008), p. 235406.

[74] Luigi Zeni et al. "A portable optical-fibre-based surface plasmon resonance biosensor for the detection of therapeutic antibodies in human serum". In: *Scientific reports* 10.1 (2020), pp. 1–9.

[75] Xiaofei Zhou, Hainan Sun, and Xue Bai. "Two-Dimensional Transition Metal Dichalcogenides: Synthesis, Biomedical Applications and Biosafety Evaluation". In: *Frontiers in Bioengineering and Biotechnology* 8 (2020).